Alfred-Wegener-Institut
Helmholtz-Zentrum für Polar- und Meeresforschung
Forschungsstelle Potsdam

Aerosols and boundary layer structure over Arctic sea ice based on airborne lidar and dropsonde measurements

Dissertation

zur Erlangung des akademischen Grades
'doctor rerum naturalium'
(Dr. rer. nat.)
in der Wissenschaftsdisziplin
Physik der Atmosphäre

eingereicht an der
Mathematisch-Naturwissenschaftlichen Fakultät
der Universität Potsdam

von
Lukas Schmidt

Potsdam, Oktober 2014

Published online at the
Institutional Repository of the University of Potsdam:
URN urn:nbn:de:kobv:517-opus4-75076
http://nbn-resolving.de/urn:nbn:de:kobv:517-opus4-75076

Abstract

The atmosphere over the Arctic Ocean is strongly influenced by the distribution of sea ice and open water. Leads in the sea ice produce strong convective fluxes of sensible and latent heat and release aerosol particles into the atmosphere. They increase the occurrence of clouds and modify the structure and characteristics of the atmospheric boundary layer (ABL) and thereby influence the Arctic climate.

In the course of this study aircraft measurements were performed over the western Arctic Ocean as part of the campaign PAMARCMIP 2012 of the Alfred Wegener Institute for Polar and Marine Research (AWI). Backscatter from aerosols and clouds within the lower troposphere and the ABL were measured with the nadir pointing Airborne Mobile Aerosol Lidar (AMALi) and dropsondes were launched to obtain profiles of meteorological variables. Furthermore, in situ measurements of aerosol properties, meteorological variables and turbulence were part of the campaign. The measurements covered a broad range of atmospheric and sea ice conditions.

In this thesis, properties of the ABL over Arctic sea ice with a focus on the influence of open leads are studied based on the data from the PAMARCMIP campaign. The height of the ABL is determined by different methods that are applied to dropsonde and AMALi backscatter profiles. ABL heights are compared for different flights representing different conditions of the atmosphere and of sea ice and open water influence. The different criteria for ABL height that are applied show large variation in terms of agreement among each other, depending on the characteristics of the ABL and its history. It is shown that ABL height determination from lidar backscatter by methods commonly used under mid-latitude conditions is applicable to the Arctic ABL only under certain conditions. Aerosol or clouds within the ABL are needed as a tracer for ABL height detection from backscatter. Hence an aerosol source close to the surface is necessary, that is typically found under the present influence of open water and therefore convective conditions. However it is not always possible to distinguish residual layers from the actual ABL. Stable boundary layers are generally difficult to detect.

To illustrate the complexity of the Arctic ABL and processes therein, four case studies are analyzed each of which represents a snapshot of the interplay between atmosphere and underlying sea ice or water surface. Influences of leads and open water on the aerosol and clouds within the ABL are identified and discussed. Leads are observed to cause the formation of fog and cloud layers within the ABL by humidity emission. Furthermore they decrease the stability and increase the height of the ABL and consequently facilitate entrainment of air and aerosol layers from the free troposphere.

Kurzfassung

Die Verteilung von Meereis und offenem Wasser hat einen starken Einfluss auf die Atmosphäre über dem arktischen Ozean. Eisrinnen (sog. Leads) verursachen konvektive Flüsse von latenter und sensibler Wärme und führen zum Eintrag von Aerosolpartikeln in die Atmosphäre. Dadurch führen sie zum vermehrten Auftreten von Wolken und modifizieren die Struktur und die Eigenschaften der atmosphärischen Grenzschicht (ABL), wodurch das arktische Klima beeinflusst wird. Im Rahmen der Messkampagne PAMARCMIP 2012 des Alfred-Wegener-Instituts für Polar- und Meeresforschung (AWI) wurden als Teil dieser Arbeit über dem westlichen arktischen Ozean Flugzeugmessungen durchgeführt. Mithilfe des nach unten gerichteten Airborne Mobile Aerosol Lidar (AMALi) wurde die Rückstreuung von Aerosolen und Wolken in der unteren Troposphäre und ABL gemessen. Dropsonden wurden verwendet, um Profile meteorologischer Größen zu erhalten. Zudem wurden in situ Messungen von Aerosoleigenschaften, meteorologischen Variablen und der Turbulenz durchgeführt.

In dieser Arbeit werden die Eigenschaften der ABL über arktischem Meereis basierend auf den Daten der PAMARCMIP Kampagne untersucht. Dabei liegt der Fokus auf dem Einfluss offener Leads auf die ABL. Aus den gewonnenen Dropsondendaten und AMALi Rückstreuprofilen wird die Höhe der ABL mithilfe verschiedener Methoden bestimmt. Die für verschiedene Messflüge und somit unterschiedliche atmosphärische Bedingungen sowie Meereisverteilungen berechneten ABL Höhen werden miteinander verglichen, und somit der Einfluss von offenem Wasser auf die ABL untersucht. Die verschiedenen Methoden zur Bestimmung der ABL Höhe führen zu unterschiedlichen Ergebnissen, je nach Eigenschaften der ABL und ihrer Geschichte. Es wird gezeigt, dass die Methoden für die ABL Höhen-Bestimmung aus der Lidar-Rückstreuung, die gewöhnlich für die mittleren Breiten verwendet werden, nur bedingt für arktische Bedingungen geeignet sind. Um die ABL Höhe aus der Rückstreuung ableiten zu können, müssen Aerosole oder Wolken in der Grenzschicht als Tracer vorhanden sein. Dazu ist eine Aerosolquelle nahe der Oberfläche notwendig, welche typischerweise unter dem Einfluss von offenem Wasser und konvektiven Bedingungen vorliegt. Dennoch ist es nicht immer möglich, die aktuelle Grenzschicht von residualen Schichten zu unterscheiden. Stabile Grenzschichten sind im Allgemeinen schwer zu detektieren.

Um die Komplexität der arktischen Grenzschicht und die beteiligten Prozesse zu veranschaulichen, werden vier Fallstudien detailliert analysiert, welche jeweils eine Momentaufnahme des Zusammenspiels von Atmosphäre und Meereis- bzw. Wasseroberfläche darstellen. Der Einfluss von Leads und offenem Wasser auf Aerosol und Wolken in der ABL wird diskutiert. Die Bildung von Wolken- und Nebelschichten, verursacht durch den Feuchteeintrag über offenen Leads, wird beobachtet. Zudem verringern leads die Stabilität der ABL, führen zu einer Zunahme ihrer Höhe und begünstigen dadurch Entrainment von Luft und Aerosolschichten aus der freien Troposphäre.

Contents

1 Motivation

The Arctic is affected by global warming more than other regions (IPCC, Intergovernmental Panel on Climate Change, 2013). Warming in the Arctic was found to be 2.5 times larger than the global average in an ensemble model study (Räisänen 2001). This so called Arctic amplification is associated with a rapid change of the Arctic environment. Sea ice extent as well as thickness decrease on a decadal scale and the fraction of younger, less stable sea ice increases. This causes an earlier onset of the melt season in spring via the so called ice-albedo feedback (e.g. Winton 2008), and an increasing occurrence of unprecedented minimum sea ice extent events in summer (IPCC 2013, chapter 2).

The fraction of leads, open water cracks in sea ice that form in consequence of ice motions, increases (Stroeve et al. 2012). During autumn, winter and spring, open water has a much higher surface temperature than the sea ice cover. One reason is a continuous heat supply from the ocean that is mostly maintained by currents from lower latitudes. Where a thick ice cover is present, it provides effective thermal insulation of the ocean against the atmosphere which can be colder than the ocean by more than 40 K during winter time. While heat fluxes over the ice are mostly directed downwards due to radiative cooling of the surface, over the ocean the large temperature difference between water surface and air causes strong upward fluxes of sensible and latent heat into the atmosphere. This increases the temperature within the atmosphere and therefore acts in favor of further reduction of the ice cover.

Besides the energy exchange, leads and other open water surfaces have considerable influence on the occurrence and distribution of aerosol particles and clouds. The most obvious effect of leads here is the emission of water vapor that increases the absolute and relative humidity in the atmosphere and promotes cloud formation. Unlike over ocean surfaces in mid-latitudes, clouds lead to surface warming over sea ice under most conditions and during most times of the year (Shupe and Intrieri 2004). The radiative effects of clouds are sensitive to the liquid water path as well as to microphysical cloud properties such as cloud particle size and cloud phase.

Aerosols are emitted from open water surfaces by different mechanisms that are mostly depending on wind speed and temperature. They have a direct radiative effect, that is however relatively small for non-absorbing particles at the low concentrations typical for the Arctic. Larger is the indirect effect of aerosols by influencing droplet size distribution and phase as well as cloud life time (Twomey 1977). At the same time clouds affect aerosol concentrations and properties within the atmosphere by wet deposition and cloud processing.

The interaction between ocean surface and atmosphere takes place within the atmospheric boundary layer (ABL). This lowest layer of the atmosphere can extend from the ground to altitudes of just few meters to several hundred meters above the surface in the Arctic. Due to the radiative cooling of the surface it is stably stratified about 75 % of the time (Persson et al. 2002) and dominated by strong, long lasting inversions. Processes in a stably stratified ABL are more difficult to understand than in a mid-latitude convective ABL (Mahrt 1999), e.g. turbulence in the stable ABL occurs sporadically and can be decoupled from the ground (Sodemann and Foken 2005).

Climate models have difficulties simulating the Arctic ABL. Tjernstroem et al. (2005)

compared six regional climate models, running over one year in the western Arctic, to measurement data from the Surface Heat Budget of the Arctic Ocean (SHEBA) experiment that took place from October 1997 to October 1998 in the same region. They found surface pressure, near surface air-temperature, specific humidity to be in good agreement with the measurement data. Long-wave radiative surface heat fluxes also agreed surprisingly well despite the large difficulties in adequately simulating cloud cover. However turbulent heat fluxes were represented poorly by all models. Observational data from SHEBA showed two regimes, one for convective and moderately stable conditions, with negative or slightly positive difference between 2 m temperature and surface temperature, and one for strongly stable conditions, where the surface was much colder than the air. While the agreement was acceptable within the first regime, where the heat flux depends to a first approximation directly on the temperature difference, all models failed in simulating the observed decrease of negative fluxes within the second, stable regime. Mielke et al. (2014) compared the regional climate model HIRHAM with observational data from the North-Pole-35 (NP-35) drift station between autumn 2007 and summer 2008. They found the model to overestimate vertical mixing of heat in the stable ABL which was related in difficulties of the model in reproducing strong surface based temperature inversions.

These examples illustrate some of the general difficulties and the relevance of understanding processes that govern the ABL over Arctic sea ice. The processes are important for understanding the Arctic climate, since they have a strong influence on the energy budget of the atmosphere.

To improve the understanding of the underlying physics and processes of climate models, measurement studies are necessary. Due to the harsh conditions in the Arctic environment, measurements are difficult to perform there and data coverage is therefore sparse. Long term measurements exist from several coastal sites in the high Arctic, but not over the Arctic ocean. The SHEBA campaign and the repeated Russian North-Pole drift stations are among the few exceptions. Satellites provide high temporal and spacial coverage, but many properties of atmosphere and ice cover are not accessible to them due to limitations in terms of resolution and indirect measurement principles. Sea ice represents a particular challenge for optical methods, for example in detecting clouds, due to the low contrast between cloud top and ice covered surface in infrared and visible.

Therefore field campaigns are crucial for closing gaps in process understanding. As a matter of principle they are not long-term observations, but can provide snapshots of atmospheric properties and processes under particular conditions. Since the applicability of statistical methods to these kinds of measurements is limited, they rely on obtaining data that characterize the examined conditions as comprehensively as possible.

For this study, measurements were performed as part of the PAMARCMIP campaign in 2012 with the research aircraft Polar 5 of the German *Alfred-Wegener-Institute for Polar and Marine Research (AWI)*. The *Airborne Mobile Aerosol Lidar* (AMALi) was installed on board of the aircraft to measure backscatter from aerosols and clouds within the atmosphere, in particular the ABL. Measurements were performed in zenith (upward) and nadir (downward) looking mode of the instrument, the nadir measurements being used for the characterization of the ABL in this study. Dropsondes were launched coincidently to measure vertical profiles of meteorological quantities between the aircraft and the surface. In situ measurements obtained during low-level flight provide a further characterization of the meteorological variables, aerosol concentrations and a measure for turbulence within the ABL.

The aim of this thesis is a characterization of processes observed in the ABL over sea ice during the campaign. Different criteria for the estimation of the ABL height are applied to data of dropsondes and lidar and their performance and the resulting ABL heights are

evaluated in the context of the underlying atmospheric and sea ice conditions. Four detailed case studies are conducted to illustrate the complexity and diversity of Arctic boundary layers and their interaction with sea ice, leads and the open ocean. Backward trajectories and sea ice concentration from satellite measurements are used to characterize the history of advected air masses within the ABL in terms of interaction with the ocean surface.

2 The Arctic atmospheric boundary layer

The earths atmosphere can be divided vertically into different layers. The troposphere is the layer in which most processes responsible for the weather take place, reaching from the ground to about 9-16 km (Hoinka 1999), depending on the geographic latitude. Above the troposphere, the stratosphere, mesosphere, thermosphere and exosphere follow. Towards the ground the troposphere can be further subdivided, yielding a layer called the atmospheric boundary layer (ABL). It can be defined as

> ...that part of the troposphere that is directly influenced by the presence of the earth's surface, and responds to surface forcings within a timescale of about an hour or less. (Stull 1988)

This definition accounts for the fact that the flow within the ABL is usually turbulent. This allows vertical mixing of influences originating from the surface much more efficiently and thus on much shorter timescales than in the mostly laminar flow of the so called free atmosphere above.

Linking the atmosphere to the ground, the ABL is of great relevance for the climate system. For example, most energy uptake from solar radiation happens through absorption by oceans and ground where it is converted into heat, which can then be transported within and through the ABL by advection and turbulence. Likewise all water vapor and the energy within it, referred to as latent heat, is transported into the free atmosphere from ground through the ABL. At the same time momentum from the free atmosphere is transmitted to the ground through turbulent and viscous friction processes within the ABL, limiting the kinetic energy of the atmosphere and thereby determining the shape of structures like synoptic systems.

2.1 Stability

The ability of the atmosphere to mix vertically is characterized by its stability. Since air pressure decreases with increasing altitude, an air parcel that rises adiabatically cools at a rate called the dry adiabatic lapse rate $\Gamma_d = -dT/dz = 9.8\,\mathrm{K/km}$, where T is the temperature of the parcel and z the vertical coordinate increasing with altitude above the surface. If the air is saturated with water vapor, condensation occurs and the released latent heat causes a lower temperature gradient, the so called moist adiabatic lapse rate, which depends on temperature and is about -6.5 K/km on global average within the troposphere (US standard atmosphere). If the actual temperature gradient within the atmosphere equals the (dry or moist) adiabatic lapse rate, its stratification is statically neutral with respect to dry or saturated air, respectively. This means that if an air parcel is displaced up- or downwards, it cools or warms at the same rate as the air surrounding it and therefore has the same density and remains in its new position. In the case of unstable stratification the atmospheric temperature gradient is lower than the adiabatic lapse rate. The cooling or warming and therefore the density change of the parcel is larger than for the surrounding air, leading to an accelerated vertical displacement of the parcel. The opposite is true under statically stable conditions. The displacement of an air parcel causes a vertical oscillation at

the frequency N, which is called Brunt-Väisälä frequency and depends on static stability.

$$N = \sqrt{\frac{g}{\theta}\frac{\partial\theta}{\partial z}}. \tag{2.1}$$

Here g is the gravitational acceleration, θ the potential temperature and $\frac{\partial\theta}{\partial z}$ the vertical gradient of potential temperature. The potential temperature is defined as

$$\theta = T\left(\frac{p_0}{p}\right)^{0.286}, \tag{2.2}$$

where p is the air pressure, T the air temperature and p_o the pressure at a reference level, usually 1000 hPa. The potential temperature is the temperature that an air parcel would have if brought to the reference level adiabatically. It is conserved for vertical motions within the atmosphere and can therefore be used to assess the static stability. A negative vertical gradient of θ means statically unstable, a positive gradient statically stable conditions. To account for the lower density of water vapor in humid, but unsaturated air, the virtual potential temperature

$$\theta_v = \theta \cdot (1 + 0.61r) \tag{2.3}$$

can be defined, where r is the water vapor mixing ratio in g/g (Stull 1988). For the low water vapor mixing ratios under typical Arctic conditions the difference to the potential temperature is relatively small.

Stability is particularly important for the understanding of the atmospheric boundary layer, since it inhibits or allows vertical turbulent mixing, the defining process of the ABL. The stability of the ABL is mainly controlled by the temperature difference between surface and air close to the surface, the so called surface layer that usually extends over the lowest 10 % of the ABL (Stull 1988). A warm surface causes a positive (i.e. upward) vertical heat flux into the surface layer which is heated, decreasing its density and producing convection. A cold surface cools the surface layer due to negative heat flux and causes a stable boundary layer.

A vertical oscillation of the air under statically stable conditions in a horizontal flow forms gravity waves. They can be caused by vertical displacement of the air, for example due a disturbance of the flow by an orographic obstacle or strong convection. Or as so called Kelvin-Helmholtz waves by dynamic instability that occurs due to vertical wind shear, i.e. a vertical gradient of the wind speed. If the Kelvin-Helmholtz waves reach a critical amplitude, they break and generate turbulence.

Thus, even in a statically stable atmosphere, turbulence can be generated mechanically. Wind shear is usually strongest close to the surface where the wind speed is reduced towards zero, resulting in the generation of turbulence there. But turbulence can also be generated at other altitudes where sufficient wind shear occurs, for example caused by a low-level jet (section 5.1.1.4).The degree of stability can be estimated by the Richardson number, a dimensionless quantity that contains the ratio of mechanical production and buoyant consumption of turbulence. It is described in section 5.1.1.2.

2.2 Height of the atmospheric boundary layer

The height of the ABL can vary considerably over space and time. Under high pressure conditions over mid latitude land surfaces, it has a well defined diurnal cycle that is mainly driven by the incoming solar radiation. Heating of the ground leads to thermal convection that causes turbulent mixing of the air up to an altitude where the buoyancy of air parcels

disappears due to the stability of the surrounding air. This altitude can be defined as ABL height. Successive warming of the ABL and entrainment of air from the free troposphere leads to an increase of the ABL height during the day. At night time, radiative cooling of the ground inhibits convection and forms a stable nocturnal boundary layer below the former convective ABL that is decoupled from the ground and remains as a neutrally stratified residual layer. After sunrise, a new convective boundary layer evolves from the ground and 'eats' its way through the former nocturnal ABL and then through the residual layer. Typical heights of the mid-latitude ABL are around 1000 m.

The Arctic ABL height behaves differently mostly due to the much weaker incoming solar radiation. Surface characteristics and the influence of wind shear become more important and the annual cycle is more distinctive than the diurnal cycle (Stull 1988). Especially over sea ice and during polar night, the dominating long wave radiative cooling of the ground leads to mostly stable conditions. ABL heights can be as low as a few meters with vertical mixing only caused by turbulence due to wind shear and surface roughness (Zilitinkevich and Baklanov 2002). Larger ABL heights can be caused by convection when cold air is advected over warm surfaces. Since air temperatures are typically far below 0 °C, open ocean water with its temperature of about −1.8 °C is comparatively warm and provides strong upward fluxes of sensible and latent heat that cause convection within the advected air and raise the ABL height.

3 Aerosol in the Arctic atmosphere

An Aerosol is defined as a suspension of solid or liquid particles in air. Such particles are omnipresent in the earths atmosphere. Their concentration as well as chemical and physical properties vary over large ranges depending on location and origin of the particles. Some basics on aerosols that are relevant for this thesis shall be briefly explained here.

Particle sizes of an aerosol usually show a broad distribution over several orders of magnitude, ranging from few nanometers to several 100 microns in diameter. However in the atmosphere particles larger than 10 μm and consist of water or ice are usually referred to as hydro meteors. While aerosols occur at concentrations up to 10^5 cm^{-3} in polluted urban air and $10^3 - 10^4$ cm^{-3} in continental air, concentrations of few hundred particles or less are common under maritime conditions and in the Arctic.

Aerosols can be characterized in different ways one of which is by their size distribution. Typical size distributions contain different modes that can in most cases be approximated by log-normal distributions. The modes originate from different formation mechanisms of the particles. Definitions of the different modes can vary (Seinfeld and Pandis 2006). Particles generated within the atmosphere from the gas phase form the nucleation mode that starts at sizes of a few nm. The next larger particles form the so called Aitken mode and above about 100 nm the accumulation mode begins that can extend up to 2.5 μm and consists of particles formed for example by condensation or by coagulation of smaller size particles that can also occur in the course of cloud processing. Particles above 2.5 μm are usually referred to as coarse mode and originate mostly mechanical formation processes as primary particles. Primary particles are emitted directly into the atmosphere. Examples of primary particles are for example sea salt that originating from sea spray, mineral dust and black carbon, that is mostly of anthropogenic origin, e.g. from biomass burning. Secondary particles form within the atmosphere for example from emissions originating from the biosphere, like dimethyl sulfide (DMS) that is emitted from oceans, or from volcanic eruptions, like sulfur dioxide that forms sulfate particles.

Aerosol in the Arctic during springtime consists to a large part of aged particles that are advected from mid-latitudes. This is often associated with a phenomenon known as Arctic haze, where advected aerosol layers lead to a significant turbidity of the Arctic atmosphere (e.g. Khattatov et al. 1997). Size distributions in the Arctic are typically dominated by two modes. For example Tunved et al. (2013) characterized aerosol size distributions that had been observed over ten years at the Zeppelin station on Svalbard, a site that is considered representative for remote Arctic conditions. On average they found number distributions dominated by an an accumulation mode, peaking mostly around 150 nm, and an Aitken mode with particle diameters <60 nm. The accumulation mode, mostly consisting of aged particles, dominates the number size distribution during springtime until late April. During the summer months, the Aitken mode becomes more important which was most likely linked to local emissions. The transition between the two modes has been observed to occur within a few days. This is considered to be caused by increasing wet removal of the accumulation mode as well as an increase of new particle formation over open water, for example due to DMS emissions that are linked to the influence of sunlight on the biological activity in the ocean. An indication for a third, larger mode was also observed by Tunved et al. (2013) that could not be fully resolved since the measurement range was limited to

a maximum of 1 μm. Seinfeld and Pandis (2006) suggest an aerosol mode with a median diameter of 750 nm in addition to an accumulation mode and a coarse mode for typical Arctic aerosol. The aerosol database OPAC (Hess et al. 1998) gives a sea salt component with a median diameter of 418 nm together with other soluble and insoluble components for typical Arctic aerosols.

In mid-latitudes, the aerosol concentration is usually highest in the ABL due to sources located at the surface and decreases towards the free troposphere. In the Arctic this can be different due to the absence of strong local sources and the frequent occurrence of advection of aerosol layers from lower latitudes.

There are a variety of processes removing aerosols from the atmosphere. Large particles of the coarse mode have relative short residence times in the atmosphere since they sink to the ground faster than small particles due to their large mass compared to their surface and therefore a comparatively low influence of friction while moving through the air. Depending on their material, particles can be hygroscopic and therefore serve as condensation nuclei to form cloud droplets in supersaturated conditions. Without these condensation nuclei, condensation would only occur at water vapor supersaturations of several hundred percent. If a cloud precipitates, the aerosol particles enclosed or solved in its droplets are deposited to the ground with the precipitation. This is referred to as wet scavenging and is the most effective process removing aerosols from the atmosphere.

Not all clouds are precipitating. In many cases they evaporate by diabatic or adiabatic heating or by entrainment of dry air. In total, these clouds do not or remove any mass to or from the air involved in the process. However, they have an influence on the components of the air, such as the aerosol. (Hoppel et al. 1986) described a bimodality within the lower size range of measured maritime aerosol size distributions that he could explain by processing of the aerosol within clouds. During cloud formation only a part of the available aerosol is activated as cloud condensation nuclei (CCN) each of which forms a cloud droplet. The minimum diameter of the activated CCN depends on the supersaturation within the cloud. The smaller particles remain in the air between the cloud droplets, but can collide with existing droplets and thus be included in them. Droplets also collide with each other when they have different sizes and therefore different settling velocities. Each collision increases the mass of aerosol, dissolved or just dispersed, within a droplet. The cloud thereby causes the redistribution of mass from smaller particles to larger ones in the size range above 0.2 μm that remain when the droplets evaporate. In addition to this, particle mass is added from the gas phase by condensation of precursor gases like SO_2 on cloud droplets. The minimum forming between the remaining smaller and the grown larger particles in the size distribution is today referred to as 'Hoppel minimum'.

Hygroscopic particles can grow without being activated to form cloud droplets, if the supersaturation is not high enough to make further growing energetically favourable. This so called hygroscopic growth leads to an increase of particle diameter and therefore to an increasing scattering coefficient as will be shown below. Hygroscopic growth is further explained in section 5.3.3.

Aerosols affect the climate by influencing the earths radiation budged, leading to a cooling on global average, which however depends on the surface albedo locally. This happens via direct and indirect effects. The direct effect acts by scattering or absorption of short- and longwave radiation, while the indirect effect occurs due to the modification of cloud properties by aerosols. Thereby higher aerosol concentrations lead to higher numbers of smaller cloud droplets for the same liquid water content by acting as condensation nuclei. This increases the cloud albedo by more effitient scattering of shortwave radiation and cloud lifetime by a reduction of precipitation.

3.1 Light scattering and absorption by aerosol particles

A light beam falling onto a small particle excites oscillations of electric charges within the particle. These oscillations can cause the emission of photons in different directions, referred to as scattering, or convert a part of their energy into thermal energy or absorption. If the scattered light has the same wavelength as the incident light, the process is called elastic scattering. Re-emitted photons can also have energies different from that of the incident photons, which is called inelastic scattering. Wavelength shifts can also occur due to quasi-elastic scattering processes, such as Doppler or diffusion broadening.

Due to the comparatively low energies involved in inelastic scattering in the earths atmosphere, elastic scattering is the process dominating radiative transfer here. Inelastic Raman scattering can for example be used by so called Raman lidars. However, the measurement principle used by the lidar instrument applied for this work (section 4.1) is based on elastic scattering, which will therefore be the focus of this section.

The intensity of the light scattered elastically by a particle I_{scat} is proportional to the intensity of the incident radiation I_0:

$$I_{scat} = C_{scat} I_0 \tag{3.1}$$

The constant C_{scat} is the scattering cross section of the particle in units of area, comparable to a shadow in geometric optics. The analogue relation as above can be defined for absorption by the particle, I_{abs}. The total energy removed from the incident beam is called extinction and is the sum of scattering in all directions and absorption. The extinction cross section is hence defined as

$$C_{ext} = C_{scat} + C_{abs}. \tag{3.2}$$

A beam of light traveling through a medium or an ensemble of particles is attenuated by scattering and absorption processes, which can be described by Bouguer-Lambert-Beer's law:

$$I_t = I_0 e^{-r\sigma_{ext}}, \tag{3.3}$$

where I_t is the transmitted light beam, σ_{ext} the extinction coefficient and r the distance traveled through the medium. The extinction coefficient is the sum of scattering and absorption coefficients, $\sigma_{ext} = \sigma_{scat} + \sigma_{abs}$, in units of $[m^{-1}]$.

Scattering and absorbing properties of particles depend on on the particle diameter D_p as well as on the wavelength of the incident light λ, which can be combined to the size parameter

$$x = \frac{\pi D_p}{\lambda}. \tag{3.4}$$

They also depend on the refractive index of the particle

$$m = n + ki \tag{3.5}$$

and therefore on the particle material. The real part n of the refractive index is responsible for scattering, the imaginary part k for absorption. The refractive index itself is dependent on the wavelength of the incident light.

Scattering by an aerosol particle is generally not isotropic. The dependency of the scattered intensity $I_{scat}(\theta,x,m)$ on the scattering angle, i.e. the angle between incident and

scattered beam, can be described by the scattering phase function

$$P(\theta) = \frac{I_{scat}(\theta,x,m)}{\int_0^\pi I_{scat}(\theta,x,m) sin(\theta) d\theta}, \tag{3.6}$$

that is normalized to the total scattering integrated between 0° and 180°. Here spherical particles are assumed, otherwise the scattering would also depend on the azimuth angle.

For spherical particles the interaction with electromagnetic radiation can be described by the Mie theory (Mie 1908). It describes an analytic solution of the Maxwell equations and is based on the idea of multipoles, that are induced in the particle by the incident electromagnetic waves, and the interference between their secondary waves. The Mie theory is described in detail in literature (e.g. Bohren and Huffman 1983) and shall therefore not be discussed here. It will be applied in this study to retrieve aerosol scattering cross sections and ohase functions based on particle size distributions (section 5.3).

Scattering for all particle sizes can in principle be calculated by Mie theory. However the characteristics of light scattering from spherical particles can be devided into regimes based on the order of the size parameter x. For size parameters $x \ll 1$, the so called Rayleigh regime, the scattered intensity is proportional to λ^{-4}. Scattering of visible light from air molecules and small particles falls into the Rayleigh regime. Scattering to forward and backward direction are approximately symmetric here, corresponding to the characteristics of a dipole. For size parameters on the order of one, scattering dependence on wavelength can not be described by a simple proportionality, but has an irregular shape due to the superposition of interfering waves scattered by the particle. The scattering is referred to as Mie scattering. The scattering phase function becomes increasingly irregular for increasing size parameters and forward scattering dominates. For size parameters $x \gg 1$ the scattering characteristics approach the geometric optics and scattering becomes independent of wavelength.

For an ensemble of particles, i.e. an aerosol, the scattering coefficient can be calculated the scattering cross section by

$$\sigma_{scat} = \int_{D_{p,min}}^{D_{p,max}} C_{scat} \frac{dN}{dD_p} dD_p, \tag{3.7}$$

where dN is the particle number concentration in units of $[cm^{-3}]$ for a particle diameter size bin dD_p. Absorption and extinction coefficients can be calculated analoguously.

4 Instruments and aircraft campaigns

4.1 The airborne aerosol lidar AMALi

The acronym LIDAR stands for *light detection and ranging*, indicating its similarity in basic operating principle with the better known RADAR. Being a remote sensing instrument, a lidar sends out visible or invisible laser pulses and detects the 'echoes' of these pulses, reflected or scattered by a target. In the case of an aerosol lidar, this target can be aerosol or cloud particles, gas molecules or, in nadir (downwards) pointing operation from an aircraft or satellite, the ground. The runtime between emission and detection of the light pulse yields the distance to the scattering target as $r = c\Delta t/2$.

AMALi, the *airborne mobile aerosol lidar*, was developed at the AWI Potsdam in 2003 for installation on board a research aircraft for use in Arctic atmospheric research (figure 4.1). It shall be described briefly here, a more detailed description of the system can be found in Stachlewska et al. (2010). AMALi uses a pulsed Nd:YAG laser operating at a wavelength of 1064 nm with a pulse repetition frequency set to 15 Hz. Most energy of the beam is converted to two additional wavelengths at 532 nm and 355 nm by a second harmonics generator (SHG) and a third harmonics generator (THG) crystal which are integrated in the commercial laser head design. The remaining share at 1064 nm is separated from the beam by a dichroic mirror that is highly reflective at 355 nm and 532 nm and transmissive at 1064 nm and dumped onto an absorbing ceramic surface (located behind the mirror, not shown in the schematic).

The light that is scattered back to the lidar from atmospheric targets is focused by an off-axis parabolic mirror to a field stop to yield a defined field of view of 3.1 mrad for the system. The light beam is split in the two wavelengths each of which is filtered by a narrow band dichroic optical filter centered at the respective laser wavelength to reduce background noise as much as possible while providing maximum transmittance at the laser wavelengths. Filter bandwidths are 0.15 nm for the filter centered at 532 nm and 1 nm for the filter centered at 355 nm. The 532 nm channel is further split into two linear polarization components, one parallel to the linear polarization of the emitted laser beam and one perpendicular to it. The perpendicular polarized channel is guided through a thin film polarizing filter to reduce cross talk from the parallel channel that receives much higher light intensities than the perpendicular channel. The signal intensity can be adjusted to the dynamic range of the detectors by inserting neutral density filters into the different channels.

The light beams of the three resulting channels are focused on three photo multiplier tube (PMT) detectors converting the light intensities to current signals. The signal of each channel is recorded by a transient recorder at a sampling frequency of 20 MHz which yields a height resolution of 7.5 m.

4.2 AMALi data processing

Data sent from the AMALi transient recorders to the data acquisition PC are saved by the acquisition software to binary files. Each file contains two minutes of data in intervals of 1 s. A 1 s data set contains two vectors per detection channel, one for the analogue signal

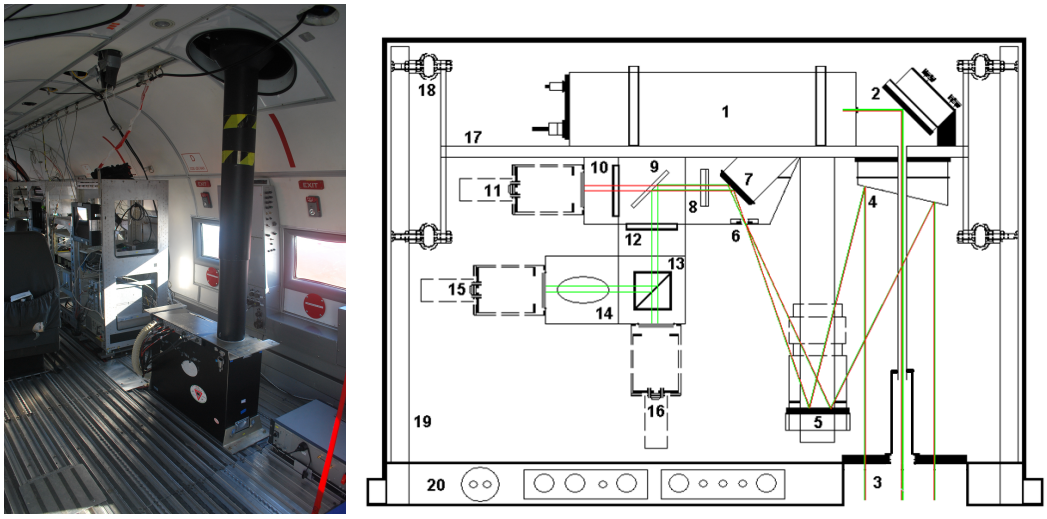

Figure 4.1: (left) The AMALi lidar on board of Polar 5. (right) The AMALi optical assembly with schematically drawn ray-tracking at 532 nm (green) and 355 nm (violet). 1. laser head 2. dichroic directing mirror with piezo motor 3. window with flexible tube 4. off-axis parabolic mirror 5. first folding mirror 6. field stop pinhole 7. second folding mirror 8. achromatic lens 9. beam splitter 10. interference filter for 355 nm channel 11. PMT for 355 nm detection 12. interference filter for 532 nm channel 13. polarizing cube 14. thin film polarizing filter 15. PMT for perpendicular 532nm detection 16. PMT for parallel 532nm detection 17. optical bench 18. springs 19. posts 20. base plate. (adapted from Stachlewska et al. 2010)

and one for the photon counting signal. The vectors have a length of 1700 elements, corresponding to the 20 MHz samples of the signal acquisition for one laser shot and therefore to the range bins of the lidar signal. Data acquisition for a shot is started synchronously with the flash lamp trigger. The Q switch, i.e. the actual emission of the laser beam into the atmosphere, is triggered with a delay. Therefore the first (pre-trigger) part of the recorded signal contains information about the pure signal background without the influence of scattered laser radiation.

4.2.1 Basic signal processing

Data processing for AMALi is performed in the proprietary numeric computing environment Matlab, partly with programs adapted from Lampert et al. (2009). In a first step, the binary data files of a flight are read into Matlab variables, combining all data for a continuous time interval. Variables are saved in Matlab format for further processing.

Further signal processing is performed by flight section in a separate program and consists of the following steps:

- Background subtraction
- Temporal averaging
- Deriving physical variables

The recorded lidar signal has a background, that consists of noise from scattering of sun light into the telescopes field of view and electronic noise from different elements in the

detection chain. The analogue channels contain an additional artificial offset that is added to the signal during recording to avoid negative values. The mean value of the signal background is as a first approximation independent of the signal range. Therefore it can be obtained from the pre-trigger range and subtracted from the whole profile to obtain the background corrected signal.

However, the baseline of the analogue signal shows a slight positive drift with increasing range. This drift can be approximated by a linear fit to the pre-trigger interval and, for better stability of the fit, to an additional part in the far range of the signal where scattering of the emitted laser light can be neglected. The fit is subtracted from the already background corrected signal. For the photon counting channels this step is obsolete, since the counts always refer to a baseline at zero.

In a next step signals are averaged over time to increase the signal to noise ratio. The averaging interval depends on the intended resolution with typical values from 1 s (no further averaging) to resolve fine structures to several minutes for robust profiles under horizontally homogeneous conditions.

4.2.2 Physical variables

The signal received by one channel of the lidar from elastic backscatter in the atmosphere is described by the lidar equation

$$P(r) = C_0 \frac{\beta(r)}{r^2} exp\left(-2\int_0^r \alpha(r')\,\mathrm{d}r'\right) \tag{4.1}$$

where $\beta(r)$ is the total backscatter coefficient, $\alpha(r)$ the total extinction coefficient, r the range from the lidar and C_0 the lidar system constant. C_0 includes all parameters of the instrument that act on the signal independent of range, as the intensity of the emitted laser pulse, the area of the receiving telescope and the gain of the detection chain. The backscatter coefficient β can be split into a component from molecular scattering and one from aerosol scattering

$$\beta = \beta_{aer} + \beta_{mol}. \tag{4.2}$$

For later use we also define the two-way transmission that accounts for extinction on the way from the laser to the target and back to the receiver,

$$T(r)^2 = exp\left(-2\int_0^r \alpha(r')\,\mathrm{d}r'\right) \tag{4.3}$$

and the range corrected signal

$$B(r) = P(r)r^2 = C_0\beta(r)T(r)^2 \tag{4.4}$$

that accounts for the decrease of signal intensity due to the distance to the target.

A variety of different methods are known to derive physical quantities of the atmosphere from aerosol lidar signals. They depend on the design of the instrumental system as well as on atmospheric conditions. In this study aerosol attenuated backscatter, attenuated color ratio and aerosol depolarization are used. These quantities are explained in the following.

4.2.2.1 Aerosol attenuated backscatter

Backscatter from aerosol particles is a fundamental quantity that can be derived from an elastic lidar signal. Since the instrument constant C_0 is generally not known and varies over time due to external influences such as the temperatures of different components of

the system, the lidar signal contains only relative information about atmospheric scattering properties depending on the range. To derive absolute values from it, a boundary condition for $\beta(r_{fit})$ is needed. For zenith pointing lidars it is common to set this boundary condition at a high altitude r_{fit}, where no aerosol is expected in the atmosphere and thus $\beta(r_{fit})$ can be set to $\beta_{mol}(r_{fit})$. Molecular scattering $\beta_{mol}(r)$ and extinction $\alpha_{mol}(r)$ can be calculated from a measured or assumed air density profile of the atmosphere.

The most common method to solve the lidar equation for zenith pointing elastic lidars is Kletts algorithm (Klett 1981). There a further assumption is made, the so called lidar ratio $S(r) = \alpha_{aer}(r)/\beta_{aer}(r)$ to account for the two-way extinction between lidar and measurement range r. The lidar equation is then solved by the algorithm starting from far to near range. By this approach any error in the assumption of the far range boundary condition decreases towards the lidar. However, for a simple elastic backscatter lidar the lidar ratio can only be guessed based on the expected aerosol types within the measurement range.

AMALi is mostly used in nadir pointing mode from about 3000 m altitude, which makes setting a boundary condition for β less straight forward due to the presence of aerosol below this altitude (e.g. Ancellet et al. 2014; Kupiszewski et al. 2013, and in situ aerosol measurements evaluated in this study). A possible way to circumvent the need of a boundary condition would be to determine the lidar constant C_0 once by comparison to a ground lidar, e.g. using the two-stream method (Stachlewska and Ritter 2010), and use it for all measurements. However, due to large temperature changes of the instrument during and between flights, C_0 is subject to changes in the order of ($\pm 50\%$), which would lead to large uncertainties in the retrieved β_{aer}. Stachlewska et al. (2010) used an approach estimating a boundary value at a range far from the lidar close above ground and applying Kletts algorithm. This process was repeated until a backscatter value assumed to be realistic for an altitude close to the aircraft was reached. However this does not solve the problem of the unknown aerosol contribution close to the aircraft.

Therefore a different approach was chosen here, calculating a C_0 for each profile by making a best estimate of the boundary condition close below the aircraft. Equation 4.4 yields

$$C_0 = \frac{B(r_{fit})}{T_0^2 \left(\beta_{aer}(r_{fit}) + \beta_{mol}(r_{fit})\right)} \tag{4.5}$$

with T_0^2 being the two-way atmospheric transmission by aerosol and molecular contribution between lidar and the fit range close below the aircraft. T_0^2 does not depend on r and can therefore be included in C_0.

To estimate a value for the signal $P(r_{fit})$, the median of the signal within a defined altitude range from 1800 to 2300 m was calculated. At this altitude the atmosphere was in most cases comparably clear, as was estimated from typical aerosol conditions found from the in situ particle measurements. At the same time the influence of signal oscillations that occur as artifacts in the near range signal is avoided. By using the median instead of a mean value the influence of spatially confined strongly scattering aerosol structures is reduced and the value is therefore considered to be closer to the signal that would be caused by molecular scattering. Since fluctuations of the lidar constant caused by temperature fluctuations take place at much longer timescales than the measurement interval, a moving average of $B(r_{fit})$ over 5 min is used to reduce short term fluctuations.

$\beta_{mol}(r_{fit})$ is calculated from a radiosonde air density profile. For the backscatter of the background aerosol $\beta_{aer}(r_{fit})$ an assumption has to be made. It is common to set this boundary condition as a backscatter ratio, which is defined as $BSR = (\beta_{aer} + \beta_{mol})/\beta_{mol}$ and is independent of altitude for a constant aerosol mixing ratio. Based on typical values

observed by the KARL lidar in Ny Alesund, Svalbard, and the fact that the flights took mostly place at higher latitudes with presumably lower aerosol concentrations, a value of $BSR(r_{fit}$,532 nm$) = 1.2$ is assumed for the 532 nm channel and $BSR(r_{fit}$,355 nm$) = 1.07$ for the 355 nm channel.

With the value of C_0, the aerosol attenuated backscatter

$$\beta_{aer,atten} = \frac{B(r)}{T_{mol}^2 C_0} - \beta_{mol} \tag{4.6}$$

can be calculated, with T_{mol}^2 being the two-way transmission due to molecular extinction. It accounts for molecular backscatter and extinction, however not for aerosol extinction. Neglecting aerosol extinction is arguable for a nadir pointing lidar under cloud free Arctic conditions. For typical aerosol conditions during the PAMARCMIP campaigns the difference between aerosol and attenuated backscatter due to extinction is in the order of 5 %, which is small compared to the uncertainty introduced by the assumption of the boundary condition that is estimated to be in the order of 20 %.

4.2.2.2 Depolarization

Volume depolarization is defined as

$$\delta(r) = \frac{\beta_\perp(r)}{\beta_\parallel(r)}, \tag{4.7}$$

the ratio of the fraction of light scattered in perpendicular and parallel direction relative to the linearly polarized laser beam, respectively (Pal and Carswell 1973). By combining the signals of the parallel and perpendicular polarization channels at 532 nm, the volume depolarization of the scattered light can be retrieved:

$$\delta(r) = \left(\frac{P_\perp(r)}{P_\parallel(r)} - c_2 \right) / c_1. \tag{4.8}$$

This is the depolarization that is caused by aerosol and molecular backscatter together. The constant c_1 is the gain ratio between the two channels, c_2 accounts for cross talk due to non ideal separation of the parallel and perpendicular components in the emitting as well as the receiving path. For AMALi the cross talk was experimentally determined by Stachlewska et al. (2010) and found to be negligible.

The disadvantage of the volume depolarization is that it depends on the backscatter ratio since it is a mixture of depolarization from air molecules and aerosol. Therefore the use of aerosol depolarization is common (Kovalev and Eichinger 2004) that is defined as

$$\delta_{aer}(r) = \frac{\beta_{aer,\perp}(r)}{\beta_{aer,\parallel}(r)} = \frac{\beta_{aer,atten,\perp}(r)}{\beta_{aer,atten,\parallel}(r)}. \tag{4.9}$$

Since the extinction on the way between lidar and target can be considered to be isotropic with respect to the horizontal plane under usual conditions, it acts in the same way on both, the perpendicular and the parallel component. Therefore the attenuated backscatter coefficient can be used equivalent to $\beta_{aer,\perp}(r)$ and $\beta_{aer,\parallel}(r)$. To calibrate $\beta_{aer,atten,\perp}(r)$ relative to $\beta_{aer,atten,\parallel}(r)$, a depolarization of 1.41 % is assumed at the fit range, which is the value of depolarization of air molecules.

4.2.2.3 Attenuated color ratio

The color ratio is a measure for the wavelength dependency of backscatter. Here, the attenuated total color ratio is defined as

$$CR(r) = \frac{\beta_{atten,532}(r)}{\beta_{atten,355}(r)} \tag{4.10}$$

for the attenuated backscatter coefficients of the two AMALi wavelengths. For small particles with $D_p \ll \lambda/\pi$ in the Rayleigh regime, scattering depends on the wavelength proportional to λ^{-4} (section 3.1). This yields a color ratio of $CR \approx 0.2$ for small particles and air molecules. Particles in the size range of the wavelength or larger scatter according to the Mie theory and appear gray for scattering adding up over the size range of a large particle mode. Color ratio values are then close to one, but can also vary around this value depending on the size distribution and also on particle shape (e.g. Bi et al. 2009; Xie et al. 2008). The color ratio is therefore a rough indicator for particle size.

4.2.3 Cloud identification

Aerosol and clouds can differ in their backscattering intensities by orders of magnitude. The differences between these two classes are usually larger than the variations that can be observed in either one of them. If one wants to address properties of clouds or aerosol, it is therefore necessary to first identify them in the data. Especially if looking at aerosols, cloud contamination has to be avoided, since even a few cloud pixels can cover variations one wants to find in aerosol backscatter.

A possible way to systematically distinguish between different atmospheric components is the use of a feature mask that assigns data to different types of scatterers. The space borne lidar CALIOP on board the satellite CALIPSO for example uses feature masks based on multidimensional probability density functions (PDF) to distinguish between clouds, aerosols and even different aerosol types (Liu et al. 2004). The separation into different aerosol types can be used for further evaluation steps by assigning typical lidar ratios to them. While this method has large uncertainties, the detection of clouds is comparatively straight forward. Especially at the low aerosol concentrations typical for arctic conditions, and in absence of a possibility to calibrate the signals in an absolute way, different aerosol types would be difficult to distinguish from AMALi measurements. Therefor the feature mask applied in this work was limited to cloud detection.

Here a simplified but still effective approach similar to the one by Liu et al. (2004) is used to detect clouds. It is mainly based on the difference in color ratio between cloud droplets and smaller particles. Figure 4.2 shows the distribution of color ratios based on aerosol attenuated backscatter for AMALi data measured during a typical flight leg, including an aerosol layer as well as low level water clouds of different optical thicknesses. Furthermore a thin, sub-visible ice fog layer within the ABL is marked by manual selection in green. A clear gap separates values originating from clouds from the ones originating from aerosol and remaining background. From visual examination of different flights a threshold value of $cr = 6.5$ was found to effectively separate the two regimes. The threshold value was chosen to rather erroneously attribute background pixels to the cloud class than miss parts of clouds to avoid contamination of aerosol measurements. Two additional low thresholds applied to the individual aerosol attenuated backscatter signals at 532 nm and 355 nm were used to avoid classification of single pixels as cloud due to noise in the color ratio in cloud free regions showing weak signal.

Visual examination of flights shows, that this cloud mask identifies practically all cloud pixels at resolutions up to $5\,\mathrm{s} * 7.5$ m. For higher temporal resolution, low SNR values lead

to considerable uncertainties. Nevertheless, these are in favor of false attribution of aerosol as cloud rather than vice versa, because SNR for the strongly scattering cloud pixels is still high enough to clearly identify them.

Additional masks were created to assure data quality. Threshold values were applied to signal to noise ratios of the different channels at a given resolution to identify regions of not trustworthy data. This is particularly relevant for depolarization ratio, that is sensitive to noise due to low signal intensities in the perpendicular polarization channel at low particle concentrations. Another mask identifies regions of strongly attenuated signal below clouds by applying a threshold to aerosol optical thickness between instrument and scatterer. An estimate of optical thickness is obtained by stepwise integration over the backscatter between the measurement altitude and the aircraft for each profile, assuming a lidar ratio $LR = 30$.

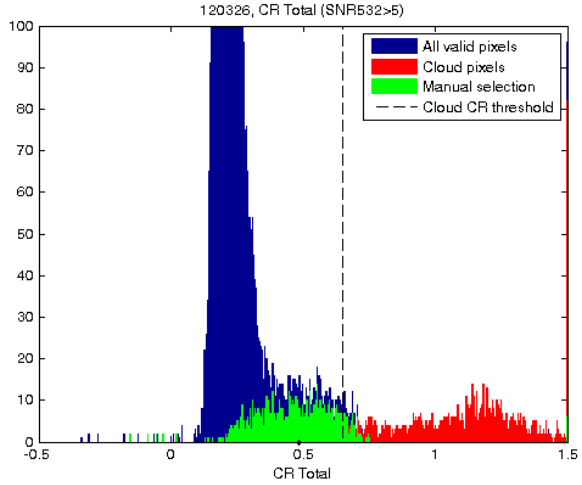

Figure 4.2: Distribution of AMALi attenuated color ratio during a typical high level flight leg in nadir mode. The measurement included a water cloud of moderate optical density, aerosol layers and an ice fog layer within the ABL that is marked in green in the plot by manual selection of the region. Blue and red denote the separation according to the cloud mask.

4.2.4 Cloud top altitude

The altitude of the highest detected cloud top between aircraft and ground is determined in a separate routine. It is based on the highest data resolution (1 s $*$ 7.5 m), to be able to follow the cloud top as closely as possible. Due to the typically high signal to noise ratio at cloud top, a short averaging time is not an issue here.

For the detection a simple threshold is applied to the attenuated backscatter variable at 532 nm. For each vertical profile, the first value meeting the threshold criterion is considered a cloud top, if it is followed by at least two more valid values. By this approach artifacts by signal noise are effectively avoided. The distance between the detected cloud top and the aircraft is subtracted from the flight altitude given by the on board GPS receiver. The measured distance is corrected for pitch and roll motions of the aircraft that increase the geometrical path of the laser beam to the cloud top. Cloud top altitudes higher than 100 m below the aircraft and lower than 30 m above the ground are not considered. If no cloud top is found for a profile, the value is set invalid.

The vertical resolution of this cloud top detection is limited by the AMALi vertical resolution and the GPS altitude resolution and is estimated to be about ±10 m.

4.2.5 Lead detection from background light scattering

The detectors of AMALi do not only detect backwards scattered laser radiation, which depends on the run time of the laser pulse, but also sunlight that is scattered into the telescopes field of view. This background can be considered constant over the time scale of the laser pulse run time. While it is generally unwanted noise when evaluating the usual lidar signal, the background light contains also useful information in itself. Part of it originates from sunlight scattered in the atmosphere by molecules, aerosols and clouds. Nevertheless, while pointing nadir and flying over arctic sea ice, the high albedo of the snow cover on the ice accounts for most of the background light when there are no clouds present between aircraft and surface. The background can thus be used as a qualitative measure of the surface albedo.

There is a strong contrast between the high albedo of the snow cover and the low albedo of leads that are either open water or thin, mostly transparent ice cover. The AMALi background signal can therefore be used as a simple measure to detect leads below the aircraft under cloud free conditions.

For the lead detection the background signals of the photon counting channels are used, since they do not contain significant electronic noise. The intensity of the sun light falling onto the surface is assumed to be unknown for simplicity reasons, since many different factors, such as clouds above and below the aircraft and sun elevation play a role here. Instead the surface albedo is determined relative to a snow background value. This value is determined for sections of the flight of 60 s, corresponding to flight distance of about 5 km. The 95th percentile of the signal of each section is used for a moving average to obtain a smooth background. The measured signal is then mapped between zero and the background value for each time step.

A threshold identifies leads with open water or covered by a thin ice layer. A clear differentiation between open water and fresh, thin ice is not reached due to the very similar albedo. The minimum lead width that is reliably and fully resolved by this method is $2*\Delta x$, where Δx is the distance covered by the lidar footprint in one sample at a given temporal resolution. However in principle, smaller leads are still detectable since they reduce the signal intensity when partly covered by the footprint.

The method has been used to validate locations of the leads shown by the MODIS image used in case study in section 7.2 with respect to the flight track. The agreement is found to be within the resolution of the MODIS image.

4.3 Aerosol in situ measurements

During the PAMARCMIP 2012 campaign, aerosols were measured in situ on board the aircraft by a suite of instruments that was provided and mainly operated by Environment Canada. Raw data were accessible and used for this work (courtesy Sangeeta Sharma and Richard Leaitch, Environment Canada). The systems are widely used in aerosol research, so here only a brief summary is given for understanding of the measurement principles.

The aerosol in the atmosphere was sampled with a diffuser-type inlet in combination with a venturi outlet to achieve sufficient flow rates for isokinetic sampling in the size range of interest. The particle loss for the inlet system was estimated to be smaller than 12 % between 20 nm and 2 μm (Roth 2014). The sampling lines of all instruments were connected to the bypass line of the inlet.

4.3.1 Optical particle spectrometer UHSAS

The *Ultra High Sensitivity Aerosol Spectrometer* (UHSAS, manufactured by DMT inc., Boulder, CO) is a so called optical particle counter (OPC), that measures the number size distribution of aerosol particles with diameters D_p between 60 and 1000 nm (Cai et al. 2008). It counts single particles passing through a laser beam by measuring the light scattered by them sidewards. Since scattering cross section C_{scat} is a function of D_p for a given wavelength, the particle diameter can be derived from the intensity of the scattered light. By integrating over a number of scattering processes, the size distribution of the aerosol is obtained.

The relation between C_{scat} and D_p also depends on the refractive index m, i.e. on the particle material. For a known refractive index it can be calculated using Mie theory and assuming spherical particles (section 3), which is a relatively good assumption for liquid particles and different salt crystals. The laser of the UHSAS has a wavelength of 1054 nm to yield an unambiguous relation between C_{scat} and D_p over the measurement range for the most common aerosol refractive indices.

Using the relationship that is obtained from the Mie calculation as calibration function, the instrument is calibrated to a material with a typical refractive index for a range of atmospheric aerosols and a known particle diameter under laboratory conditions. The instrument installed on board Polar 5 was calibrated to a polystyrene latex particle standard with a refractive index of $n = 1.59$. It was sampling with a flow of 1 l/min and a temporal resolution of $\Delta t = 1$ s.

4.3.2 Condensation particle counter (CPC)

To cover the smaller size ranges below 60 nm, a condensation particle counter (TSI model 7610) was used in parallel to the UHSAS. Its operation principle is similar in that it measures light scattering from particles. However it only counts the total integrated number of particles above a lower cutoff diameter.

Since C_{scat} varies proportional to λ^{-4} in the Rayleigh regime for particles much smaller than the wavelength of the scattered light, the smallest detectable particle size is limited by detector sensitivity and available laser wavelengths. To extend the size range towards smaller particles, they are therefore grown to measurable sizes by condensation growth within the instrument. This is achieved by guiding the aerosol flow through a chamber connected to a supply of n-butanol that is heated to cause evaporation of the n-butanol, and thereafter cooling it with a Peltier element. Thereby supersaturation of the n-butanol is reached, causing condensation on the particles which are then counted by guiding them through a laser beam and detecting the scattered light pulses.

The lower cutoff diameter is given as $D_{p50\%}$, specifying the diameter below which the counting efficiency drops below 50 %. It can be adjusted by varying the temperature difference between the n-butanol chamber and the saturation chamber. The instrument used here was calibrated to $D_{p50\%} = 14$ nm. Sampling was performed at a volumetric flow of 1 l/min with a temporal resolution of $\Delta t = 1$ s.

4.3.3 Nephelometer

An integrating Nephelometer (TSI model 3563) was installed in the aerosol rack to measure scattering coefficients in situ at three wavelengths, namely 450 nm, 550 nm and 700 nm. The instrument directs an aerosol sample flow through a chamber illuminated by a light source with a wide opening angle. The total light scattered by the ensemble of particles

under scattering angles ranging from 7° to 170° is detected. This yields a truncated scattering coefficient $\sigma_{s,tr}(\lambda)$ for each of the three wavelengths. This scattering coefficient does not include scattering in close to forward and backward directions due to the geometry of the instrument. To obtain the total scattering coefficient $\sigma_s(\lambda)$, a correction scheme is applied here as proposed by Anderson and Ogren (1998) that also allows for non lambertian properties of the instruments light source, based on a parametrization including the Ångstrom exponent of the sampled aerosol. Molecular Rayleigh scattering is subtracted during standard internal processing based on the measured sample pressure.

A rotating shutter allows additional measurement of a hemispheric backscatter coefficient for 90° to 170°. Note that this definition of backscatter is different from the one generally used in the context of lidar measurements which only refers to a scattering angle of 180°. The latter definition is the one used in this work if not stated otherwise.

Due to heating of the instrument, the temperature within the sampling chamber was usually higher than 20 °C, while outside temperatures were far below 0 °C. Relative humidity of the sampled aerosol was therefore considerably reduced by warming while entering the sampling chamber and can be assumed to be generally below 30 % and in most cases at much lower values. The measurement therefore refers to aerosol in a dry state regarding hygroscopic growth.

4.4 Dropsonde and aircraft meteorological measurements

To measure meteorological variables within the atmosphere, dropsondes and in situ aircraft sensors were applied, that are described in this section. The different sensors and the variables measured by them are listed in table 4.1.

Table 4.1: Different sensors used for temperature, humidity and wind measurements by dropsondes and onboard P5. Values are as given by the manufacturers. Accuracies marked with a * are repeatabilities only. ([1]Helten et al. 1998)

Instrument	Variable	Sensor	Accuracy
Dropsonde	RH	Humicap	2 % RH*
	T_{air}	Thermocap	0.2 °C*
	u, v	GPS	–
Rosemount Hum.	RH	Humicap (Vaisala HMT333)	5% RH[1]
Rosemount TAT	T_{tat}	PT 100 (102EJ2BS)	–
AIMMS-20	RH	capacitive (polymer)	±2 % RH
	T_{air}	thermistor (glass bead)	0.3 °C
Buck CR2	T_d	Dew point mirror (Rosemount inlet)	±0.1 °C

4.4.1 Dropsonde

Dropsondes are used to measure vertical profiles of temperature, humidity, pressure and wind speed and direction while descending on a small parachute from the aircraft to the surface. The measured data of the dropsonde are transmitted to a receiver on board the aircraft in real-time. Wind speed and direction are measured by a GPS receiver, temperature, humidity and pressure by fast reacting sensors that are exposed to the airflow of the descending sonde. The most recent dropsonde model that is deployed on campaigns

with the AWI Polar 5 aircraft is the NCAR GPS dropwindsonde (model RD94) that was developed at the *National Center for Atmospheric Research* (NCAR) and is manufactured by Vaisala, Inc. (Hock and Franklin 1999).

4.4.1.1 Laboratory test

A simple laboratory test was carried out on three dropsondes of a less than one year old batch to verify their ability to measure high relative humidities. Therefor the sensor rods of the dropsondes were introduced into a saturation chamber, a device routinely used for pre-launch quality control of radiosondes (Leiterer et al. 2005). On the ground of the cylindrical chamber, desalinated water is heated to a temperature slightly higher than that of the air above it. An impeller rotating horizontally above the surface at a defined speed establishes a laminar flow that ventilates the sensor horizontally at about 5 m/s. For fitting the sensor rod into the chamber, the plastic shield was removed after unpacking each sonde. After initializing the sonde, the sensor rod was placed into the pot for about two minutes to assure full saturation of the air. Data were transmitted to the AVAPS system and recorded as during usual in-flight operation.

An example of a test measurement of T and RH (of sensor 2) is shown in figure 4.3. The sensor rod was inside the saturated chamber between shortly before second 50 and shortly after second 200. Temperature within the chamber was 19.3 °C, about 2 °C warmer than the air outside. Moving the rod into and out of the chamber, respectively, took less than 1 s. Relative humidity adjusted to the conditions inside the chamber faster than resolved with this method and stabilized at a near constant value reaching a maximum of 94.5 % for sensor 1 and 93.6 % for sensor 2. Allowing for the accuracy of 2 % RH of the dropsonde, this yields a dry bias of 4.5 % against the expected 100 % within the chamber. The test was performed for three dropsondes. On average they reached a relative humidity of 95.5 %, with 94.5 % the lowest value and 96.8 % the highest one. This bias is still significant at high relative humidities, but is not corrected here due the small number of available test measurement and the lack of a possibility to test the dropsondes individually before starting them. However, as will be shown in section 4.4.3, the dropsondes perform well on average under cloud-free conditions.

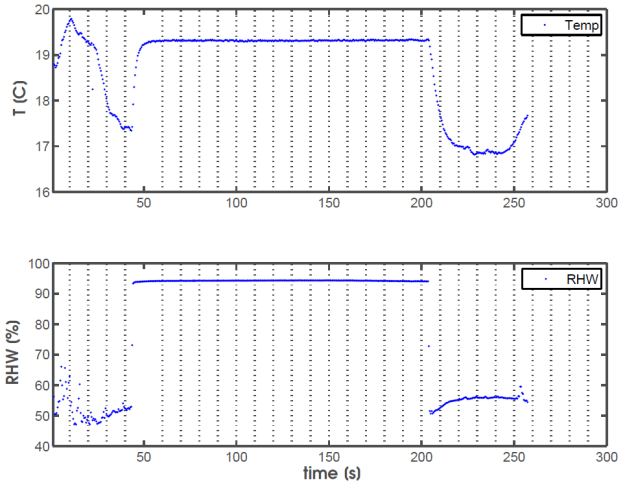

Figure 4.3: Temperature and relative humidity from test measurement with a dropsonde in the saturation chamber. As the sonde is introduced into the chamber, the relative humidity reaches 93.6 %.

4.4.2 Aircraft sensors

The Polar 5 aircraft of Alfred-Wegener Institute is equipped with a suite of instruments that measure standard meteorological variables. Since the data are provided in raw formats, they have to be corrected and converted to yield the final physical variables. The instruments and data processing are described here.

4.4.2.1 Rosemount temperature and humidity sensors

A Goodrich Rosemount total air temperature sensor, deiced model 102a is located in the nose region of the aircraft. The sensor type is widely established in aviation. It consists of a housing with forward pointing air inlet, designed to exclude particles and cloud or rain droplets from the air flow to prevent contamination of the sensor. The airflow is decelerated within the housing to a speed near zero, its kinetic energy thereby being converted to internal energy. Thus the temperature of the decelerated air, referred to as total air temperature (T_{tat}), is higher than the actual temperature of the surrounding air (outside air temperature, T_{oat}).

The sensor itself is a thin platinum wire sensor (PT100), reacting to temperature changes with a time constant of around 1 to 1.5 s for the typical speed and altitude range of Polar 5 during the campaigns (Stickney et al. 1994). To prevent icing, the sensor housing is heated, whereby the influence of the heating to the measurement is kept low by a laminar flow and boundary layer removal design inside the housing. A correction of the remaining influence can be applied, leaving an uncertainty of about ± 0.3 K.

To yield atmospheric temperature and humidity values from the aircraft sensors, some corrections and conversions have to be applied to the measurements (Stickney et al. 1994). On the measured temperature T_{meas} first a deicing correction is applied to account for warming of the probed air by the heated sensor inlet surface. This yields the recovery temperature T_{rec}, which is the actual temperature the air reaches inside the sensor housing by the dynamic heating effect. It is different from the (ideal) total air temperature T_{tat} by roughly -10 %, since the deceleration of the air is not complete. T_{rec} is corrected to T_{tat} using a third order polynomial fit based on empirical information provided by the manufacturer (Stickney et al. 1994). The static or outside air temperature is then given by

$$T_{oat} = T_{tat} - \frac{v_{tas}^2}{2\ c_p}, \tag{4.11}$$

where v_{tas} is the true air speed, i.e. the velocity of the aircraft with respect to the surrounding air, and c_p the isobaric heat capacity of dry air. T_{oat} is the actual air temperature of the atmosphere.

Relative humidity is measured with a capacitive Vaisala Humicap sensor included in a Rosemount housing similar to the one used for the temperature sensor. An additional temperature sensor located in the same housing close to the Humicap measures the temperature of the probed airflow $T_{meas,hum}$. This value is used for converting the relative humidity to outside air conditions.

The measured humidity RH_{meas} is subject to similar influences by its sensor housing as for the temperature sensor. The atmospheric humidity can be calculated as

$$RH_{atm} = RH_{meas} \cdot \frac{e_s(T_{meas,hum})}{e_s(T_{oat})}, \tag{4.12}$$

where $e_s(T)$ is the temperature dependent saturation vapor pressure over water.

4.4.2.2 Dewpoint mirror (CR-2)

The dewpoint or frostpoint temperature, respectively, was measured with a dewpoint mirror (Buck Research Instruments, L.L.C., Model CR-2 Hygrometer, 2009). It is installed inside the cockpit of the aircraft and provided with sample air through an inlet based on a Rosemount housing connected to a stainless steel tube inside the aircraft that leads to the instrument.

Within the instrument air is flowing above a mirror which is kept at a low temperature. Humidity from the air flow condenses on the mirror and produces a layer of condensate. The thickness of this layer influences the reflectivity of the mirror, which is measured by a photo diode. Its output signal is fed into a circuit regulating the mirror temperature to keep the layer of condensate at a constant thickness, meaning that the net flow of water molecules onto or from the surface is zero. This temperature is, by definition, the dewpoint temperature.

A value for water vapor mixing ratio w in units of parts per million is calculated by the instrument internally. Relative humidity for outside air temperature conditions is derived from this value by

$$RH = \frac{w \cdot R_v/R_d \cdot p}{(622 \cdot 10^{-3} + w \cdot R_v/R_d) e_s(T_{oat})}, \tag{4.13}$$

where R_v/R_d is the ratio of the gas constants for water vapor and dry air, p the air pressure and $e_s(T_{oat})$ the saturation vapor pressure over water at T_{oat}.

4.4.2.3 AIMMS-20 turbulence probe

A five hole turbulence probe (AIMMS-20, detailed description in Beswick et al. 2008) is installed below the right wing of Polar 5. It is a commercial instrument that measures a three-dimensional wind vector at a sampling frequency of 40 Hz and further temperature and humidity that are recorded at 40 Hz as well, but have time constants in the order of seconds and hence do not resolve turbulence. The measurement principle of the five hole probe is based on measuring dynamic pressures resulting from the air flow under different angles of incidence. The tip of the instrument has a hemispherical shape sitting at the end of a cylinder and pointing in flight direction. Dynamic pressure is measured through five holes that are arranged in a cruciform pattern at the tip, one in the middle and four arranged under a certain angle with respect to flight direction. Each hole is connected to a pressure sensor inside the instrument that measures the difference to a reference pressure, which is obtained from a ring of holes located at the side of the cylinder and hence perpendicular to the flight direction.

The five dynamic pressures resulting from different angles yield velocity and direction of the flow hitting the probe. This flow is relative to the coordinate system of the moving aircraft and can be seen as the sum of aircraft motion relative to the ground and air motion relative to the ground. To yield the wind vector, i.e. the air motion relative to the ground, a coordinate transformation is performed by the instruments data processing algorithm. The AIMMS-20 therefor has an integrated inertial measurement unit (IMU) that uses GPS, accelerometers and gyroscopes to measure aircraft motion and attitude in three linear and three rotational axes at a sampling frequency of 40 Hz.

The instrument is mounted with some distance to the wing and is supposed to be located outside of the boundary layer of the aircraft. Hence it does not see turbulence that is generated by the aircraft. However it is still considerably influenced by the aerodynamics of the wing that deforms streamlines as a matter of principle while generating lift and moving through the air. Therefore calibrations are necessary to retrieve the undisturbed flow from the measurements. The calibration procedure includes specific flight maneuvers

that have to be performed in as far as possible uniform flow to eliminate the aircraft influence that varies according to flight conditions. Unfortunately the calibration performed for the campaign data used here was not entirely successful and hence the retrieved wind vectors are not consistent in direction and magnitude. They depend considerably on the aircraft flight conditions and can not be used for analyzing the mean flow.

However they still contain information about relative fluctuations of the wind components and about the spectral characteristics of these fluctuations. Figure 4.4 shows power spectra of vertical and horizontal wind that are obtained by fast Fourier transform (FFT). A time interval of 240 s from a measurement at relatively constant flight altitude near the top of a maritime convective boundary layer is selected. Before conducting the FFT a linear trend is removed from the signal by least squares fit and a bell taper window is applied to reduce artifacts introduced by discontinuities at the boundaries of the signal (Stull 1988).

Both spectra show a slope very close to the ideal $f^{-5/3}$ that is expected for the inertial sub-range of a turbulent flow (Kolmogorov 1991). Only for low frequencies the curves deviate from the slope, which is consistent with the characteristics expected for large scales in a turbulent flow, but may also include some influence of aircraft motions. The small maxima in the vertical wind spectrum near 6 Hz and 12 Hz can be found in different spectra of the instrument and are likely to be the result of oscillations of the wing. They contain very little energy and can be neglected for the treatment of the turbulence data here.

It can be concluded that the spectral characteristics of a typical turbulent flow are well represented in the AIMMS-20 wind measurement up to the highest resolved frequency of $f_N = 40\ \text{Hz}/2 = 20\ \text{Hz}$, the Nyquist frequency of the system. Towards the lower end of the spectrum a high pass wavelet filter is applied in this study, suppressing frequencies below 0.1 Hz to minimize the possible influence of aircraft motions that is not properly removed by the calibration. A second alternative variable was created with a filter frequency of 0.5 Hz to obtain a measure for the scale of turbulent structures. The obtained filtered wind components are used as a qualitative measure for the occurrence of turbulence in the atmosphere, in analogy to the usual separation of a quantity, e.g. the vertical velocity w, into a mean part $\bar{w}$ and a disturbed part

$$w' = w - \bar{w}, \tag{4.14}$$

representing turbulent fluctuations.

Since the velocity of the aircraft is high compared to the velocity scales involved in the observed turbulence and stationarity may be assumed over the time scale of a measurement interval, the measurement can be considered to be a snapshot of the turbulent eddies present at this particular time. The time or frequency scale can therefore be converted to a spatial scale based on the mean true air speed (TAS), the speed of the aircraft with respect to the mean air flow. In the example shown in figure 4.4, the frequency range contributing to w' corresponds to an approximate spatial scale range from 3 m to 580 m considering the mean TAS of around 58 m/s. Spectra referring to atmospheric properties will be plotted with a wave number as abscissa, based on the actual average TAS of the measurement interval.

4.4.2.4 Surface temperature

The temperature of the snow, ice or water surface, respectively, below the aircraft is measured with a nadir pointing radiation thermometer (Heitronics, model KT19.85II). The temperature provided by the instrument is a brightness temperature, i.e. the temperature

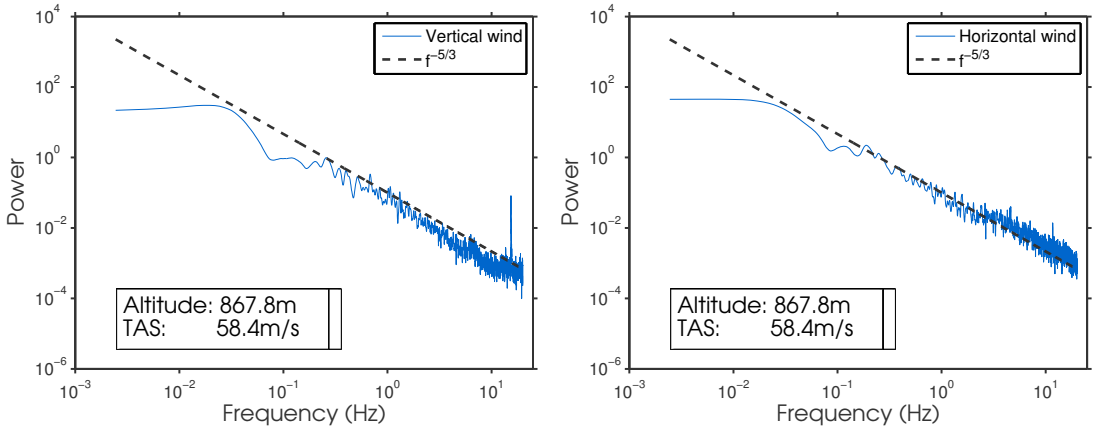

(a) (b)

Figure 4.4: Power spectra from wind measurements of the AIMMS-20 near the top of a maritime, turbulent boundary layer at ≈ 868 m altitude. The dashed line indicates the slope expected for the inertial sub-range of a turbulent flow. a) vertical velocity, b) horizontal velocity.

a black body would have to emit the same intensity as the actually measured gray body at a wavelength λ. Since the emissivities of snow, ice and water are around $\epsilon = 0.99$ for the wavelength band of the measurement between 9.6 and 11.5 μm (MODIS UCSB emissivity library of the MODIS LST group at University of California, Santa Barbara (UCSB)), the measured brightness temperature is close to the physical surface temperature.

The measurement band of the instrument is optimized for maximum atmospheric transmittance. However clouds and fog between aircraft and ground can influence the measurement by absorbing and emitting thermal radiation according to their own temperature. To keep atmospheric influence at a minimum, surface temperature is only used from low level flight legs that were carried out at altitudes around 100 m. Due to flight safety reasons, these flight legs were only possible at good visibility conditions close to the ground and thus the influence of fog on the surface temperature measurements is assumed to be as low as possible. An exception may be the occurrence of intense low level steam fog over open leads that may mask their temperature signature. However, such conditions seemed to be rare according to visual observations. Assuming a surface emissivity of $\epsilon = 1$, the error of the obtained surface temperature T_{surf} is estimated to be smaller than $\pm 1K$.

4.4.2.5 Photo camera for sea ice concentration

A nadir pointing photo camera (Canon EOS-1D Mark 3, 14 mm focal length) was installed on Polar 5 to take photographs of the sea ice surface at preset time intervals. The camera was operated with a shutter speed of 1/2000 s and automatic field stop setting. Photos were taken at intervals of 15 s, and 10 s, varying between flights.

The high contrast due to different albedos between snow covered ice surface and dark open water surface can be used for an automated detection of open or recently refrozen leads. A simple qualitative method was developed that is similar to the one used for lead detection from lidar background signals (section 4.2.5).

A threshold value is applied to the brightness value of each pixel of the blue channel of a photo. The threshold value is set at a fixed ratio between the brightest and the darkest pixel to allow for the dynamic range of the photo. The towed sea-ice probe EM-Bird (section 4.5)

that was in the field of view of the camera during operation is used as a reference target. It has markers in a dark blue tone similar to typical brightness values of open water and in white, similar to the snow surface. This assures an appropriate setting of the threshold in case of full snow cover or ocean surface. Further criteria were applied on dynamic range to enable the application of the lead detection in absence of the EM-Bird during high level legs, but in this there is a significant probability of an erroneous detection of shades behind ridges as leads. Therefore the detection is only used on low level legs here.

The fraction of pixels with values lower than the threshold is defined 'open water' fraction. A second threshold was adjusted by visual comparison of a number of photographs to detect refrozen leads below a certain brightness value, yielding a 'lead' faction. However the false detection rate can be high for this threshold, depending on light conditions and therefore it is only used as a qualitative measure.

The advantage of the method is that it resolves very small scales of leads down to less than 50 cm and at the same time covers a two-dimensional footprint below the aircraft of about 100 m $\times$ 150 m during low-level flight. Due to the time interval the coverage of the photos is not seamless at low flight altitude and the derived quantities therefore have to be seen as random samples.

4.4.3 Comparing dropsonde and aircraft temperature and relative humidity

The humidity sensor of Vaisala dropsondes was subject to discussion in the past due to a reported dry bias. Wang (2005) compared dropsonde and radiosonde profiles within and below maritime stratocumulus clouds to assess this bias. They did not find a significant dry bias beyond the accuracy of the dropsonde (2% relative humidity). A similar investigation is performed here for cold Arctic conditions. Dropsonde profiles of temperature and humidity are compared to aircraft in situ measurements to determine a potential bias of the dropsonde sensor and to validate the agreement between temperature and humidity profiles measured by dropsondes and aircraft sensors. Of the aircraft sensors the Rosemount PT100 temperature and the Rosemount Humicap humidity sensor are used for the comparison.

For the comparison, near coincident vertical aircraft and dropsonde profiles of two different Arctic campaigns are selected, the PAMARCMIP 2012 campaign and the VERDI 2012 campaign. Low level stratus clouds were present in a number of cases. Temperatures measured by the dropsondes range from -33 °C to $+5$ °C and altitudes from about 70 to 3000 m. Four cases showing obvious influence of horizontally inhomogeneous clouds and strong horizontal temperature gradients are removed from the analysis based on visual examination. The measured values from both, dropsonde and aircraft profiles, are averaged over equidistant altitude intervals of 50 m. The influence of atmospheric inhomogeneities is further reduced by excluding all bins for which the standard deviation of the temperature values from the aircraft measurement exceeds a threshold of 0.2 K or the standard deviation of the relative humidity measured by the aircraft exceeds a threshold value of 5 % RH. This excludes in particular bins around strong inversions that might have varied slightly in altitude between the profiles and therefore would introduce large deviations.

Altitude bins are classified as cloud for the comparison if 90 % of the dropsonde humidity values within the respective bin are higher than 85 % and 90 % of the aircraft humidity values are higher than 97 %. Bins that contain no humidity values surpassing the thresholds from both, aircraft and dropsonde profile, are classified as cloud-free. All remaining bins are excluded from the analysis.

Figure 4.5 shows the difference, dropsonde minus aircraft measurements, of all valid bins. A total of 20 combined profiles are included in the comparison. Red bars are based

on cloud free atmosphere, blue bars show the cases in which both dropsonde and aircraft were sampling clouds. Nine profiles contain measurements from clouds, yielding a relatively small number of comparable bins, since the vertical extent of the cloud layers was limited. The aircraft humidity sensor measured unrealistically high values of relative humidity within clouds, which is expected due to the design of the sensor housing that leads to the evaporation of droplets in the warming air flow within the housing. For the cloud bins, dropsonde humidity measurements are therefore not compared against the aircraft humidity sensor, but against a constant value of 100 % as it can be approximately expected within clouds.

It has to be noted that the comparison of dropsonde and aircraft measurements does not solely refer to deviations between the sensors themselves as it would be obtained from laboratory measurements. It rather allows a statement about the consistency of the profiles measured by dropsondes and aircraft sensors under real atmospheric conditions. This includes a possible systematic bias of the sensors as well as errors that are introduced due to time lags of the sensors having different time constants. To some extent it also includes differences of the sampled atmosphere due to the horizontal distance between aircraft vertical profile and dropsonde launch. This accounts for a large part of the scatter of the deviations between dropsonde and aircraft, but is expected to approximately cancel out for the mean values, since the 20 different profiles were measured at different locations, orientations and atmospheric conditions.

In cloud free atmosphere, the comparison shows a good overall agreement of the temperatures as well as the humidities. The values of mean and standard deviation (in brackets) are $\Delta T = -0.3$ K (0.87 K) for the temperature difference and $\Delta RH = -0.9$ % (7.8 %) for the relative humidity difference, hence no significant bias is found. Within clouds the dropsondes agree with the aircraft measurements in temperature, while the humidity sensor of the dropsonde only reaches approximately 90 % on average. One reason for this bias is the time lag of the humidity sensor that causes a slow adaption to the strong humidity increase at cloud tops.

The dropsonde temperature and humidity measurements are subject to a time lag, depending on temperature and absolute humidity of the environment. The time constant of the sensor is defined as the relaxation time needed for the sensor to adjust to e^{-1} of a step change ΔT_0 or ΔRH_0 in the profile (Stickney et al. 1994). To estimate the time constants, dropsonde profiles from the two campaigns are selected that include sharp vertical gradients occurring at temperature inversions at the top of stratocumulus clouds. These provide fast transitions from warmer to colder, and from dryer to more humid air. Nearby profiles from the faster reacting aircraft sensors are used to assure that the respective inversion has a much smaller vertical extent than the relaxation of the dropsonde measurement and hence can be used as approximation for a step change. Cloud top altitudes from AMALi are used to verify the beginning of the step for the humidity profile. The temperature inversion usually occurs slightly above the cloud top and is therefore identified visually in the profile. A function of the shape $\Delta y(t) = \Delta y_0 e^{-t/\tau}$, where y is temperature or relative humidity and t the time since the dropsonde reached the top of the inversion, is fitted manually to the temperature or relative humidity profile, respectively. This yields the time constant τ for the profile. Five profiles are analyzed that show well defined step-like transitions occurring at cloud tops.

Temperatures below the inversions were in a range between -15.4 and -4.2 °C with ΔT_0 between -3 and -5 °C and ΔRH_0 between 20 and 30 % RH for the analyzed profiles. For the temperature sensor the retrieved time constant is found to be (4.5 ± 2) s on average, for the humidity sensor (8.2 ± 2) s, based on the examined profiles. No significant dependency of the humidity time constant on temperature could be identified due to the small number

of profiles and the limited temperature range. Time constants for the humidity sensor are given by the manufacturer as < 0.5 s at 20 °C and < 20 s at -40 °C. Wang (2005) had found a value of 5 s at 15 °C in marine stratocumulus clouds, suggesting an underestimation of the time constant by the manufacturer. In contrast to this, the value of (8.2 ± 2) s down to temperatures of -15.4 °C found here is in better agreement with the range given by the manufacturer. For the temperature sensor the time constant given by the manufacturer is < 2 s. The value of 4.5 s found here suggests a slightly slower reaction time after taking into account the uncertainty that is estimated to be 2 s due to the non-ideal step change at inversion tops.

Due to the large time constants of the humidity sensor expected for low temperatures, dropsonde humidity obtained below $-25°$ or coincident with sharp temperature gradients will be excluded from following analysis.

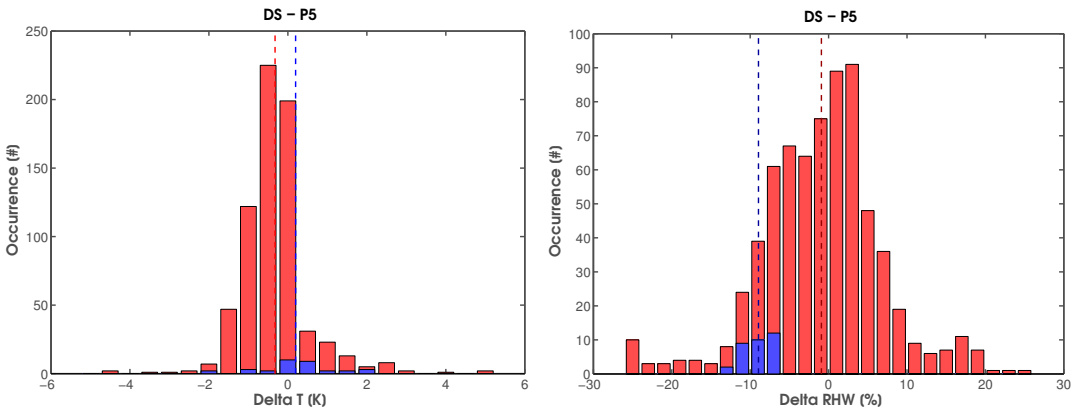

(a) (b)

Figure 4.5: Differences between dropsonde and near coincident aircraft vertical profiles of (left) temperature and (right) humidity measurements. The comparison includes 20 profiles from the campaigns PAMARCMIP 2012 and VERDI 2012. Measurements in cloud free atmosphere are shown in red, measurements within clouds in blue. Dashed vertical lines indicate the mean values of the differences.

4.5 PAMARCMIP campaign

Data for this study were obtained during the Polar Airborne Measurements and Arctic Regional Climate Model Simulation Project (PAMARCMIP) campaigns (Herber et al. 2012). Measurements were made from the aircraft Polar 5, a modified Basler BT-67, of the Alfred-Wegener-Institute. The aim of the campaigns is to obtain snapshots of atmospheric and sea ice conditions during spring time, covering a large part of the western Arctic ocean. So far the campaign was performed in 2009, 2011, 2012 and 2013.

The focus of this study is on data measured in 2012, with flights taking place between 20 March and 23 April. During the campaign the Polar 5 was based at different stations near the coasts of Svalbard, Greenland and Canada that had the logistical capabilities to accommodate aircraft and crew. Figure 4.6 shows an overview of the flight tracks performed during the campaign in 2012 that are used for this study. The measurements covered a latitude range from about 70°N to 86°N and different sea ice conditions.

The measurement pattern of most flights consisted of three parts (figure 4.7):

A low-level transect close to the surface at around altitude to measure aerosol concentrations and meteorological parameters with the in situ instruments on board the aircraft as well as sea ice thickness using an electromagnetic probe (EM-Bird, Haas et al. (2010)) towed below the aircraft. The low level leg was generally performed at an altitude of approximately 70 m which was the operation altitude for the EM-Bird. Lower flight altitudes were not possible during this flight phase, but short climbs up to 150 m altitude were performed about every ten minutes for calibration of the EM-Bird. These profiles are used in section 7 to characterize conditions below and above the top of the ABL. Flight operation was critically dependent on good visibility of the horizon and therefore clouds or fog had to be avoided on some flights.

A high-level leg at 3000 m altitude that was preferably conducted along the same track over ground as the low-level leg in the opposite direction. During this leg the AMALi lidar was operated in nadir mode and dropsondes were launched as frequently as possible. This was mostly at a time interval of approximately 10 minutes, due to the circumstances that only one dropsonde can be handled by the receiver at a time, a drop takes about 6 minutes and the next dropsonde had to be prepared for the next launch while communicating with the receiver. By using the same track as for the low-level leg, measurements of both tracks can be compared if assuming stationary atmospheric conditions. The time difference between the legs is smallest at the far end of the track with 10 to 30 min, depending on the time needed for the ascent, and largest at the near end with mostly about 5 hours separating the measurements.

An ascent or descent profile, respectively, was usually conducted at each end of the flight track, connecting the low- and the high-level leg. On some flights an additional pair of ascent and descent profiles was conducted in the middle of the flight track. Profiles were either performed as spirals or as steps of about 2 minutes length in altitude intervals of usually 500 m. The stepwise profiles allow longer averaging periods for in situ measurements.

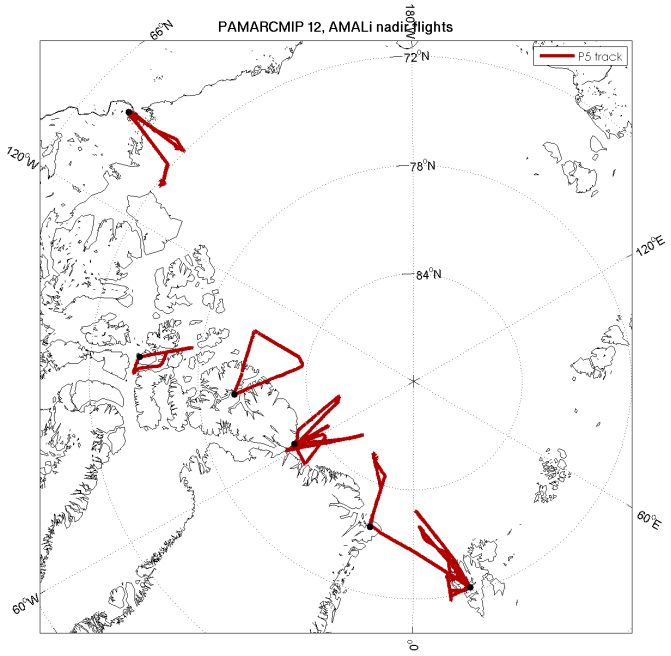

Figure 4.6: Map showing the flight tracks (red) of flights performed during the PAMARCMIP campaign in 2012. Black dots indicate the different stations from which the flights were conducted. These are from bottom right to top left: Longyearbyen, Station Nord, Alert, Eureka, Resolute Bay and Inuvik.

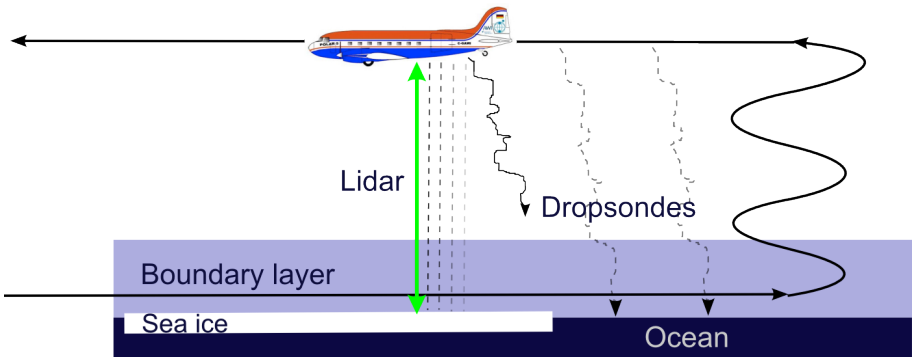

Figure 4.7: Schematic of the typical flight pattern during the PAMARCMIP campaign, consisting of three main parts: A low-level leg at approximately 70 m close to the surface and partly within the ABL (depending on ABL height), ascending and descending profiles in most cases at the end of each leg and a heigh level leg that was preferrably following the track of the low level leg. During the high level leg dropsondes were launched and nadir lidar measurements were performed.

5 Methods and data processing

This chapter explains methods that were used to derive further quantities from the data beyond the basic processing of the measurements. The main section deals with methods to determine ABL height. Two further sections explain the use of satellite and reanalysis data to characterize the influence of sea ice concentration on air masses, as well as the retrieval of aerosol optical properties from in-situ measured size distributions using Mie calculations.

5.1 Methods to measure boundary layer height

Determining the height of the ABL is generally not as straight forward as it may seem. The definition by Stull (1988) (section 2) is usually not directly accessible to measurement methods. Instead, a variety of quantities can be measured in vertical profiles that are related to different definitions of ABL height. The obtained height can differ significantly between the different methods. The adequacy of different methods and definitions for a situation depends on the conditions as well as on the application. While the top of a mid-latitude convective ABL is typically relatively well defined, large differences between different criteria can arise in stable ABLs as they are common in the Arctic (e.g. Zilitinkevich and Baklanov 2002, Vickers and Mahrt 2004).

In the following, several methods will be described which can be applied to the measurements that are available for the cases studied in this thesis.

5.1.1 From dropsonde data

The vertical profiles of the meteorological variables temperature, humidity as well as wind speed and direction that are measured by dropsondes, are all related in more or less direct ways to the present state or the history of the ABL. Humidity profiles are excluded from the analysis here, since their slow response in cold air leads to large errors in the ABL over sea ice that is characterized by low temperatures and sharp gradients. Temperature and wind profiles can be used to estimate ABL heights based on a number of different criteria that are described here.

5.1.1.1 Temperature gradient

A relatively simple definition of ABL height is based on the vertical temperature gradient. Generally, a positive vertical gradient of virtual potential temperature $\partial\theta_v/\partial z$ indicates static stability, i.e. the absence of thermally induced convection (section 2.1). Besides convection, turbulence within the ABL is also driven by wind shear, which means that despite a positive gradient of θ_v there can be turbulent mixing. A reasonable threshold value for the gradient that can be used to detect the top of the ABL is therefore expected to be greater than zero. For convective situations, Dai et al. (2011) found a value of $\partial\theta_v/\partial z = 0.01$ K/m to best represent ABL heights over sea ice. They were using the altitude where turbulence significantly decreased as a reference, obtained from measurements with an aircraft turbulence probe. For stable conditions, the gradient method can have problems detecting ABL height, since it does not take explicitly into account dynamic instability that is induced

from wind shear. Another difficulty of the method is that the derived altitude, z_{Tgrad}, is sensitive to the time lag error of the dropsonde temperature at low temperatures below sharp inversions. A higher threshold $\partial\theta_v/\partial z = 0.04$ K/m is therefore used here. It is set to still trigger the detection at the base of capping inversions, while compensating the temperature error as far as possible. This was achieved by a comparison of dropsonde and coincident aircraft temperature profiles. The remaining error of z_{Tgrad} is estimated to be in the order of ±20 m, where the largest relative errors occur at small values of z_{Tgrad} since temperature gradients and therefore the dropsonde error are highest in cases of shallow, stable ABLs and surface based inversions.

5.1.1.2 Richardson number

The role of wind shear in generating turbulence can be explicitly taken into account by using profiles of the Richardson number to estimate ABL height. The Richardson number is a dimensionless measure for the laminar or turbulent nature of a flow under the influence of gravity. It is based on the ratio of a term for buoyant production and a term for mechanical production of turbulent kinetic energy (Stull 1988). Under statically stable conditions the buoyancy term acts against turbulence, while the mechanical term produces turbulence. A higher Richardson number therefore indicates a higher stability of the flow. A variety of definitions for Richardson numbers exist that vary depending on application and available quantities. They are usually derived from the gradient Richardson number, that is defined as

$$Ri_g = \frac{\frac{g}{\theta_v}\frac{\partial\theta_v}{\partial z}}{\left(\frac{\partial u}{\partial z}\right)^2 + \left(\frac{\partial v}{\partial z}\right)^2}, \tag{5.1}$$

where g is the gravity acceleration, θ_v the virtual potential temperature and u and v the mean horizontal components of the wind speed. Since gradients are in most cases not explicitly known from meteorological measurements, as from radiosondes or dropsondes that measure at discrete height intervals, they are usually approximated as difference quotients. This yields the so called bulk Richardson number

$$Ri_b = \frac{g\Delta\theta_v\Delta z}{\overline{\theta_v}\left((\Delta u)^2 + (\Delta v)^2\right)} \tag{5.2}$$

with the finite differences being calculated between two discrete measurement altitudes and $\overline{\theta_v}$ the mean of the virtual potential temperatures measured at these altitudes. A positive sign of the finite differences is defined as an increase with altitude. Ri_b is tested and mentioned in section 6 as Ri_2, but not used further in this study.

Critical values of Ri_b, indicating that a laminar flow becomes turbulent, have been derived from theoretical and laboratory research and are commonly assumed to be between $R_c \approx 0.21$ and 0.25 (Stull 1988), but can also take higher or lower values in stably stratified ABLs depending on surface roughness (Vickers and Mahrt 2004). As turbulence needs a trigger in order to start from a laminar flow, it exhibits a hysteresis effect. The critical value for the transition from turbulent to laminar flow is therefore higher than R_c, with a typical value of $R_T \approx 1.0$ (Stull 1988).

As equation 5.2 is derived from the gradient form of the Richardson number, it refers to discrete thin layers within the atmosphere and is sensitive to variations in gradients within the respective height intervals of these layers. Moreover it depends on the vertical resolution of the measurement. For an estimate on the height of the ABL the characteristic of the whole boundary layer regarding turbulence is of interest. Therefore a form of the

bulk Richardson number referring to a layer extending from the surface to the altitude z_i is widely used:

$$Ri_1(z_i) = \frac{g(\theta_v(z_i) - \theta_v(z_0))z_i}{\overline{\theta_v}(u_i^2 + v_i^2)}. \tag{5.3}$$

Here $\overline{\theta_v}$ is the mean virtual potential temperature of the layer extending from z_0, the altitude of the lowest dropsonde measurement close to the surface, to z_i. This definition of the bulk Richardson number is discussed for example by Vickers and Mahrt (2004). Although it does not include a surface temperature, it is referred to as surface bulk Richardson number here, since it extends down to the lowest altitude above the surface that is accessible to the dropsonde measurements. It is used here with a threshold $Ri_c = 0.22$ that was validated based on several profiles using the turbulence measurements as described in section 5.1.2. Ri_1 is not sensitive to local vertical gradients, but to the overall stratification from the surface up to the altitude z_i and therefore less sensitive to possible small scale perturbations in the wind and temperature profiles than Ri_b.

5.1.1.3 Temperature inflection point

Temperature profiles often show a discontinuity that can be associated with the top of the ABL. It is caused by the formation of a mixed layer within a stably stratified atmosphere below the altitude where the discontinuity forms (Stull 1988). The downward heat flux caused by entrainment at the top of the mixed layer leaves a well defined edge in the temperature profile above. This edge can be detected from the second derivative of the temperature profile. The profile is smoothed using a moving average with a window size of five altitude steps of the dropsonde (≈ 25 m) three times iteratively on the temperature profile. The second derivative is then approximated by the difference quotient

$$\left.\frac{\partial^2 T}{\partial z^2}\right|_i \approx \frac{T_{i+1} + T_{i-1} - 2\ T_i}{(0.5\ (z_{i+1} - z_{i-1}))^2}. \tag{5.4}$$

The first local maximum of the second derivative that surpasses a threshold is defined as temperature inflection height, z_{Tinfl}. The threshold is set empirically to detect any clearly visible discontinuities while not being triggered by small scale fluctuations or gradual changes of the profile. The location of the maximum that defines z_{Tinfl} is not sensitive to the threshold value.

5.1.1.4 Low-level jet altitude

A low-level jet (LLJ) is a local maximum in the vertical wind profile within the lower troposphere. While under the assumption of a stationary geostrophic flow, wind speed generally decreases towards the ground owing to the loss of momentum caused by friction, this is often not the case in a real atmosphere. Wind speeds can increase to values significantly higher than the geostrophic equilibrium under stably stratified conditions. Such low level jets typically occur at the altitude of a strong inversion, like the capping inversion of the ABL or within the Arctic stable boundary layer. They can be caused by different mechanisms (Stensrud 1996).

A typical formation mechanism in mid-latitudes is an inertial oscillation following a diurnal cycle (Blackadar 1957). Convective vertical transport of horizontal momentum during the day reduces the wind speed within the ABL to subgeostrophic values and causes a horizontal wind component towards low pressure. The formation of the nocturnal stable boundary layer after sunset decouples the former ABL from the ground and inhibits the

vertical turbulent exchange of momentum. The air consequently accelerates in response to the horizontal pressure gradient during the night and gains momentum, while the Coriolis force acts on the wind direction to restore the geostrophic balance. The resulting inertial oscillation causes supergeostrophic wind speeds reaching their maximum about 8 hours after the breakdown of convection (Stensrud 1996). Inertial oscillations can also be found in the absence of a diurnal cycle as a result of large scale changes of surface temperature. Another mechanism producing low level jets is shallow baroclinicity caused by strong gradients in surface temperature as they occur at coasts or the marginal sea ice zone which is particularly relevant over the arctic ocean (Jakobson et al. 2013).

A low-level jet is commonly defined as the lowest wind maximum above which the wind speed decreases by at least 2 m/s below an altitude of 1500 m (Stull 1988). This definition is used here as well for the detection of LLJs.

5.1.2 Vertical velocity fluctuations

With their relatively coarse temporal resolution, dropsondes are not able to resolve small scale turbulent fluctuations of wind, temperature or humidity. To estimate ABL heights from their profiles one has therefore to rely on features that are related to the vertical extend of turbulent or thermal influence of the surface (Wetzel 1982). To validate the methods applied to dropsonde data, it is therefore useful to compare them to explicit measurements of a turbulent quantity.

Dai et al. (2011) compared profiles of equivalent potential temperature θ_v and a formulation of the Richardson number to vertical velocity fluctuations w' as an indicator for turbulence from aircraft measurements over sea ice during the SHEBA campaign. The altitude up to which turbulence occurred starting from the measurement level closest to the ground was considered to represent the 'true' ABL height for both convective and stable cases.

Measurements of turbulent wind vectors at 40 Hz are available for several flights of PAMARCMIP 2012 from the AIMMS-20 five-hole probe (section 4.4.2.3). They are only for few cases coincident with dropsonde profiles, but were used to qualitatively validate the threshold for the critical Richardson number Ri_c (section 5.1.1.2).

5.1.3 Mixing height from lidar data

Under certain conditions, ABL height can be derived from lidar data. Several methods have been evaluated and used in past studies. In the case of aerosol lidars, which shall be discussed here, they all have in common that they rely on a tracer that is visible to the lidar, usually aerosols or clouds. The underlying idea of most methods is to distinguish between the air masses of the ABL and the free troposphere by differences in the concentrations of the tracer. Most aerosols are directly or indirectly (via a gas phase) emitted from sources located at or near the surface. At the same time wet deposition by clouds, that is the most efficient sink for aerosols (section 3), takes place at any altitude within the troposphere. Therefore aerosol number and mass concentrations are usually higher within the ABL than above. By detecting the transition between higher and lower aerosol concentrations from lidar backscatter signals, the height of the ABL can be estimated.

An overview of different methods to derive ABL height from surface based remote sensing is given in Emeis et al. (2008) with a particular focus on lidar measurements. Early methods relied on simple thresholds applied to backscatter signals (Melfi et al. 1985; Boers et al. 1988). Since different threshold values have to be used depending on absolute aerosol concentrations, these methods require some manual evaluation of the data and are therefore not very efficient. More robust methods use the gradient between high backscatter within

the ABL and lower backscatter above it. This can be achieved by using simple difference quotients for the first or second derivative or by applying a wavelet transform to the backscatter signal. A method that was successfully applied on convective ABLs in mid-latitudes is based on the horizontal variance of backscatter profiles (Crum et al. 1987). This method relies on high aerosol concentrations and intense entrainment into the ABL and was therefore found here to be not applicable under typical arctic conditions. Gradient and wavelet methods as well as an inflection point method using the second derivative of the signal are applied in this study and described in detail below.

5.1.3.1 Gradient method

Distinct gradients between vertical layers of atmospheric constituents can indicate boundaries between air masses that exist due to the absence of mixing between them. The opposite is not necessarily true, since mixing may have taken place in the past and is not ongoing anymore, so that the absence of distinct gradients does not allow a statement about present vertical mixing.

To be a valid proxy for vertical mixing, the horizontal and temporal scale of the gradient need to be large compared to the turbulent eddies that would cause the mixing. However, it is also possible that mixing of air takes place irrespective of a gradient, if the tracer is not conserved for vertical motions. This is the case for the formation liquid water at the bottom of convective clouds. In rising air parcels condensation takes place at the altitude where water vapor saturation is reached due to adiabatic cooling. Droplets evolve and form a cloud above this so called lifting condensation level (LCL). Droplets of air parcels descending from the cloud through the LCL evaporate on a short time scale at about the same altitude. Therefore the LCL causes a relatively sharp transition between cloud free air and cloud that does obviously not indicate an absence of mixing. Since adiabatic cooling and warming are related to the direction of up- and downward motions, respectively, this type of condensation and evaporation can only occur at the bottom of a cloud. The cloud top is therefore a more reliable indicator for the vertical separation of air masses, at least if diabatic processes can be neglected. This is usually the case on the time scale of turbulent mixing.

Here the gradient of the averaged and smoothed range corrected lidar signal is used (section 4.2). To improve the signal-to-noise ratio while limiting temporal and spacial averaging to the necessary minimum, range corrected signals from the channels at 532 nm and 355 nm are summed up to B_{sum}. The gradient of a profile is then calculated as the central difference quotient

$$\left.\frac{\partial B_{sum}}{\partial z}\right|_i \approx \left(\frac{B_{sum,\ i+1} - B_{sum,\ i-1}}{z_{i+1} - z_{i-1}} + \frac{B_{sum,\ i+2} - B_{sum,\ i-2}}{z_{i+2} - z_{i-2}}\right)/2, \tag{5.5}$$

where i is the index of the altitude bin and z the altitude vector, starting from the ground. The difference quotient is calculated over ± 2 altitude bins, corresponding to ± 15 m here, which provides an additional smoothing effect to reduce the influence of signal noise.

The gradient profile is then searched for local minima, where a minimum is only accepted if the value of the next maximum is higher by a preset threshold. This threshold ΔB_{sum} is defined as the median of B_{sum}, divided by a factor f that was adjusted manually to a value as low as possible to still exclude peaks resulting from signal noise. The same value of f is used for all measurements.

The first local minimum starting from the ground that has an absolute value higher than ΔB_{sum} is then defined as the gradient based ABL height h_{AMgrad}.

If clouds are present that attenuate the signal close to the ground below a threshold,

ABL heights from AMALi are rejected since no statement is possible about whether there is an ABL signature below the cloud. If the signal is not attenuated past the threshold below an optically thick cloud, the cloud is assumed to extend down to the surface and indicate a coupling between surface and cloud top. Here the cloud top is accepted as ABL height.

5.1.3.2 Backscatter inflection point method

The second derivative of B_{sum} can be used as well in the detection of the ABL height. For example Emeis et al. (2008) refer to it as inflection point method, detecting the first minimum of the second derivative above ground as ABL height. This height is generally lower than the one found with the gradient method, since it marks the base of the transition zone caused by mixing between ABL and free troposphere.

Here the second derivative is used to estimate the vertical extent of the transition zone. The smoothing applied to the signal before calculating the second derivative is stronger than the one used for the gradient method, to avoid false detection of small scale features as inflection points. A moving average with a constant window width of 5 steps, corresponding to 37.5 m, is applied three times iteratively to yield an appropriate smoothing, based on visual examination of different signals. The second derivative is calculated from the smoothed signal as

$$\left.\frac{\partial^2 B_{sum}}{\partial z^2}\right|_i \approx \frac{B_{sum,\ i+1} + B_{sum,\ i-1} - 2B_{sum,\ i}}{(z_{i+1} - z_i)^2}, \tag{5.6}$$

and then searched for extrema, marking inflection points of B_{sum}, in analogy to the gradient method. Of these detected extrema, the first minimum located below the ABL height defined by the gradient method and the first maximum located above it are selected. They are used as a measure for the bottom and the top of the transition zone, respectively.

The transition zone is not always well defined if profiles show a smooth gradient at ABL top. However in these cases its determination can still serve as an estimate for the upper and lower uncertainty range of the gradient based ABL height.

5.1.3.3 Wavelet method

Another efficient way to identify gradients between ABL and free troposphere in lidar backscatter signals is using a wavelet transform. The method has been applied in a number of studies (e.g. Davis et al. (2000), Cohn and Angevine (2000), (Brooks 2003) and others). The wavelet transform decomposes the signal in a spatial position as well as a spatial scale of structures in the signal. This allows the use of different scales to detect gradients under a variety of conditions, including low signal to noise ratios.

The wavelet transform is based on the convolution of the signal and a so called wavelet function. In this case the Haar wavelet (figure 5.1) is used, a step function that is defined as

$$h\left(\frac{z-b}{a}\right) = \begin{cases} +1, & b - \frac{a}{2} \le z \le b \\ -1, & b \le z \le b + \frac{a}{2} \\ 0, & \text{elsewhere.} \end{cases} \tag{5.7}$$

Here z is the altitude, b is the translation, i.e. the position of the center of the Haar wavelet, and a is the dilation, i.e. the spatial scale of the wavelet function. The wavelet transform

is then calculated as

$$W_B(a,b) = \frac{1}{a}\int_{z_b}^{z_t} B_{sum}(z)h\left(\frac{z-b}{a}\right)dz, \tag{5.8}$$

where $B_{sum}(z)$ is the range corrected backscatter signal summed for both wavelengths, and integration is performed between the lower and the upper limit of the profile, z_b and z_t, respectively. The Haar wavelet is suited for gradient detection due to its good resolution in the spatial domain, rather than in the frequency domain, compared to other wavelets.

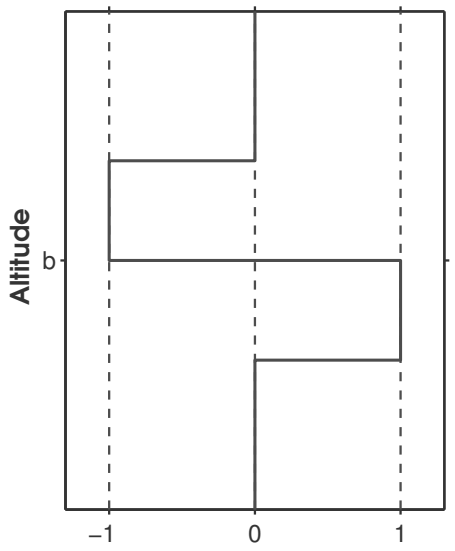

Figure 5.1: Haar wavelet function with altitude on the Y axis as independent variable. The dilation 'a' is the width of the wavelet including both, positive and negative part.

The principle behavior of the wavelet transform of an idealized signal with a step-like decrease at the altitude of the ABL top z_{ABL} is intuitive: Assuming a signal that is constant with altitude below and above the step, $W_B(a,b)$ equals zero for $b + a/2 < z_{ABL}$ and $b - a/2 > z_{ABL}$, and is positive if z_{ABL} is within the range of $b \pm a/2$. The positive peak of the wavelet transform can therefore be used to locate z_{ABL} in a similar way as with the gradient method.

An advantage of the wavelet method over the gradient method is that by varying the dilation a of the Haar wavelet, the detection can be adjusted to the scale of the signal features of interest. This allows more control of the detection for real lidar signals that include noise, a finite gradient at ABL top and gradients within the ABL or the free troposphere that are not zero. Figure 5.2 shows a lidar profile measured on 22 April 2012 over sea ice, where the ABL was influenced by open water causing convective mixing and enhanced backscatter. The ABL top is well defined here and the signal above and below it does not show strong gradients or aerosol structures. On the right, wavelet coefficients for different dilations of the unsmoothed profile are plotted. For the smallest dilation $a =$ 15 m the wavelet coefficient is entirely dominated by noise and small scale structures. Towards larger values of a, a peak at the altitude of the ABL top evolves. Its maximum has the highest value for the largest dilation and remains at a relatively constant altitude independently of the dilation. The ABL height can be easily determined by detecting the maximum of $W_B(a,b)$ at a scale that roughly corresponds to the vertical extent of the

transition zone, which is approximately 80 m in this case. The exact choice of the dilation is not critical as long as it is large enough to sufficiently reduce the influence of noise, and small enough not to reach the ground for $b = z_{ABL}$, i.e. $a < 2 \cdot z_{ABL}$. A variable for the ABL height based on a dilation of $a = 112.5$ m is defined here and named z_{WL1}.

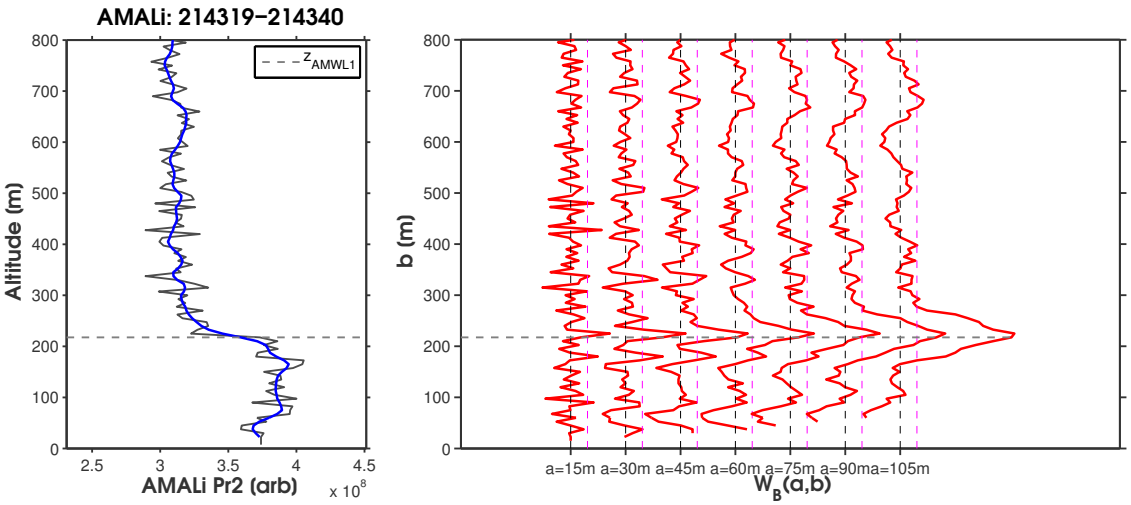

Figure 5.2: (left) Example of a range corrected backscatter profile B_{sum}, showing a well defined mixed ABL, measured on 22 April 2012 over sea ice with open water influence. The black line shows the profile averaged over 21 seconds, that is used for the wavelet transform, the blue line is the profile smoothed with a triple running mean in order to highlight its basic structure. (right) The wavelet transform $W_B(a,b)$ of the profile for different dilations a. The curves are shifted by an offset for better display. The horizontal dashed line indicates the ABL height obtained for $a = 112.5$ m, using the threshold value indicated by the vertical magenta line.

This case is comparable to backscatter profiles of mid-latitude convective boundary layers that are frequently discussed in literature (e.g. de Haij et al. (2007)). Similar situations were encountered during several flights of the campaigns that are examined here. However it is not in general representative for profiles of the lower atmosphere over the Arctic ocean during spring time. The atmosphere over sea ice is frequently characterized by stable conditions along with advected aerosol layers and stratus clouds that complicate the identification of a mixed layer from backscatter profiles, if there is one at all. Figure 5.3 shows a profile that does not correspond to the typical pattern of a convective boundary layer as discussed above. Instead it includes gradients at different scales and at different altitudes. The maximum of the coefficient for the largest dilation, $a = 120$ m, might identify the ABL height to be 165 m, depending on the exact value of the threshold. Only for smaller dilations an additional peak at 75 m becomes clearly visible. If it was a little closer to the ground, it would not be included for the larger dilations at all and could not be identified even if it was more pronounced at smaller scales. The wavelet spectrum plotted in figure 5.4 illustrates how the peaks at the two altitudes, that are clearly discernible for small dilations, merge for larger dilations. In order to obtain a broader scale of gradients that can be detected, wavelet coefficients of different dilations can be averaged and then searched for maxima. This was done in a similar way by de Haij et al. (2007). The lowest dilation included in the average is set to 45 m to exclude noise, and the largest to 105 m, which is approximately the scale of the largest transition zones found from the campaign

data. The ABL height found by this method is called z_{WL2}.

An exemplary comparison of gradient, wavelet as well as inflection point method is shown in figure 5.5 for the case of a well defined ABL. Under these conditions the gradient and the wavelet methods are almost equivalent, however the wavelet method z_{AMWL1} with its large scale was found to be more robust for shorter signal averaging times leading to lower signal to noise ratios.

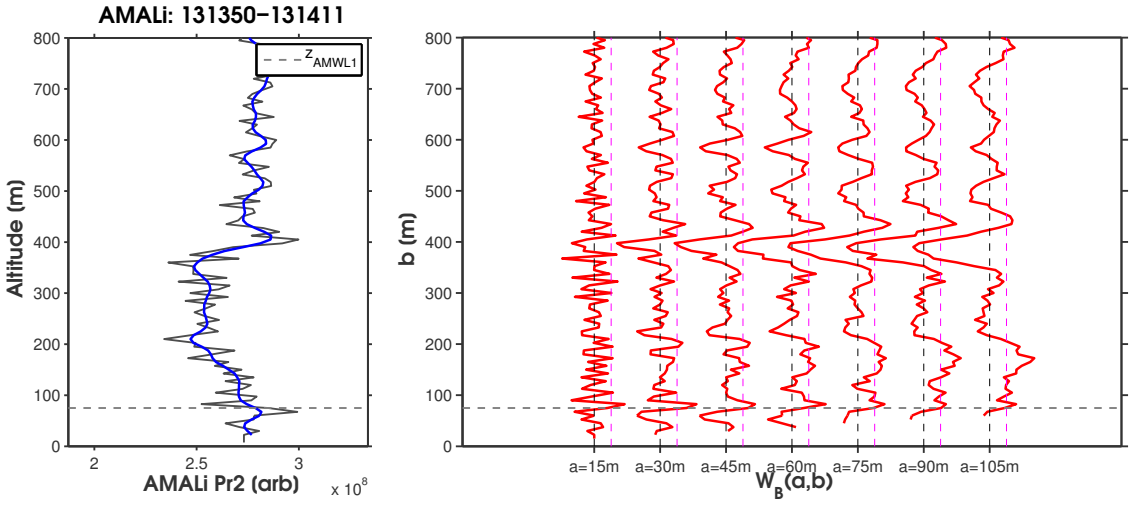

Figure 5.3: Same as figure 5.2, but for a profile measured on 24 March 2012, showing a more ambiguous structure.

5.2 Influence of sea ice concentration on advected air within the ABL

5.2.1 Sea ice concentration

A measure for sea ice cover is obtained from satellite data. The product NISE (*Near real time sea ice and snow extent*) is obtained from the *National Sea Ice Data Center* (NSIDC). It contains sea ice concentration at a spatial resolution of 25x25 km that is derived from brightness temperature and polarization measurements of the SSM/I instrument using the NASA team algorithm (Cavalieri et al. 1992). Data covering the entire Arctic are available on a daily basis and include in each pixel the most recent measurements. The accuracy of the sea ice concentration is estimated to be within 5 % under most conditions. Larger errors arise mostly during summer time when ice is covered by melt ponds. Errors are also introduced by recently refrozen leads that are interpreted as open water due to the thin ice cover. The first error source is not a concern for the spring time measurements of the PAMARCMIP campaigns. The attribution of recently refrozen leads as open water is even desirable here, since it increases the sensitivity to the occurrence of leads in a pixel, that might otherwise not be resolved due to their low open water fraction.

5.2.2 Hysplit trajectories over sea ice

Air parcel trajectories are calculated using the *Hybrid Single Particle Lagrangian Integrated Trajectory Model* version 4 (HYSPLIT, Draxler and Hess (1998)). ERA-Interim reanalysis data at a spatial resolution of 1.5° x 1.5° and a temporal resolution of six hours are used as

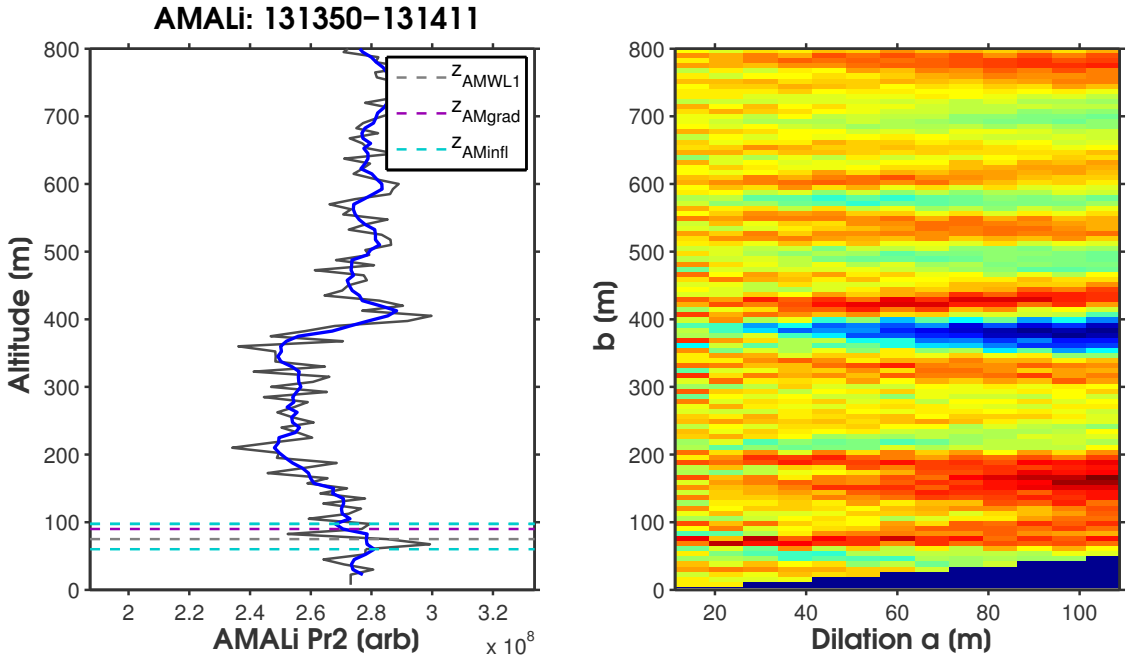

Figure 5.4: (left) Profile of 24 March 2012 as in fig. 5.3. (right) Wavelet spectrum of the profile. Red indicates high values and blue low values of $W_B(a,b)$.

meteorological input fields. The ERA-Interim reanalysis dataset is calculated by the *European Center for Medium-Range Weather Forecasts* (ECMWF), combining measurement data with forecasts to yield a picture of the state of the atmosphere at a given time step (Berrisford et al. 2009). The variables used by HYSPLIT are 3-D geopotential, temperature, humidity and wind fields as well as 2 m temperature, 10 m horizontal wind and the surface geopotential field. The model is run on a local PC under Windows 7.

Calculations of backward trajectories are performed for two different sets of endpoints. For the first run backward trajectories are initialized for each dropsonde profile location at 50 and 500 and 1000 m altitude ending at the time of the dropsonde measurement and reaching back in time over a maximum of 144 h. The second run includes two trajectories for every two minutes of the flight, ending at the location of the aircraft at the aircraft altitude and at 10 m, respectively. They are reaching back in time over 48 h. The time resolution of the trajectories is 1 h.

To obtain a measure for the characteristics of the surface that influenced each air parcel during its advection within the ABL, the trajectories for the lowest endpoints are combined with the sea ice data sets. Due to the mostly stable stratification of the lower troposphere over sea ice and the presence of a capping inversion in almost every dropsonde profile it is generally assumed that air parcels remain preferably within the ABL and therefore are influenced by the underlying surface. NISE sea ice concentration for each trajectory time step is set to the value of the next pixel of the dataset of the respective day. Since sea ice concentrations vary on a relatively slow time scale this is considered a small issue here compared to the error that can be expected from the trajectories.

An additional run was performed with GDAS (*Global Data Analysis System*) input data to obtain an estimate on the influence of the used reanalysis data set on the retrieved air parcel history. The GDAS data have a spatial resolution of 1° x 1° and a temporal resolution of three hours. Figure 5.6 (left) shows the surface properties obtained along trajectories based on GDAS data for the same endpoints as with the ERA-Interim data.

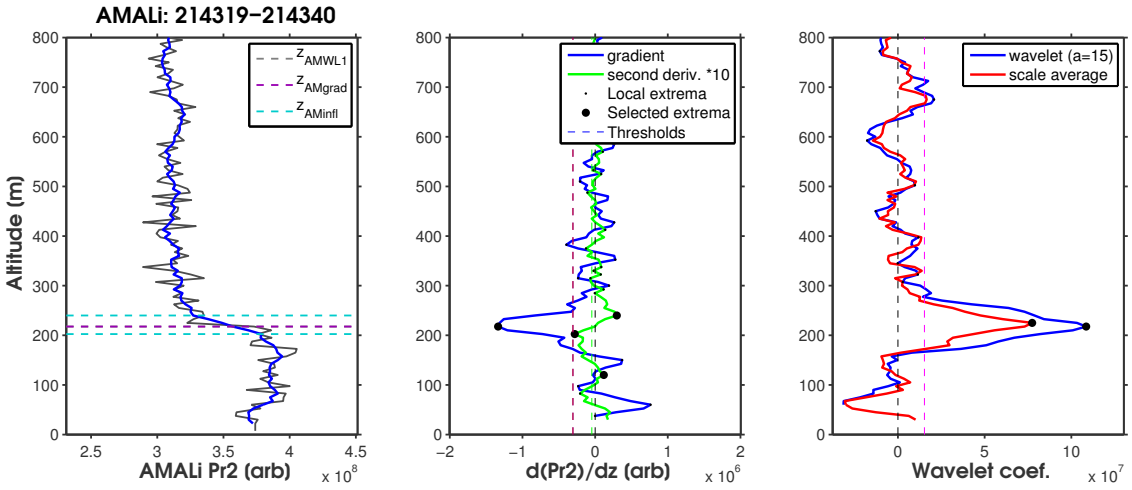

Figure 5.5: Illustration of gradient and wavelet method. (left) Backscatter profile B_{sum} from the flight on 22 April 2012 as in figure 5.2. The smoothed curve (blue) is the one used to calculate the gradient here. Horizontal dashed lines indicate the ABL heights obtained from gradient and wavelet method and the transition zone boundaries from the inflection point method. (middle) First and second derivative of the backscatter profile (blue and green). (right) Wavelet coefficients for fixed dilation and averaged over dilations a from 45 m to 105 m.

Although the spacial differences between the trajectories of the different input fields can be large, the general pattern of ice concentrations seen by the air parcels seem to be robust for most profiles. Deviations increase considerably for trajectory points beyond 48 hours back in time. The trajectories ending at profiles 20 and 21 (flight '120326') differ considerably which is consistent with large gradients in the meteorological fields due to a frontal passage.

5.3 Retrieval of aerosol optical properties from in situ data by Mie forward calculation

In order to further characterize the properties of aerosols that cause backscatter features measured with AMALi and to test assumptions about these aerosols, AMALi measurements are compared to the in situ aerosol measurements.

Scattering coefficients measured by the integrating nephelometer are not directly comparable to backscatter measured by the lidar, since they include light scattered over a broad angular range and the nephelometer does not resolve the scattering phase function.

In order to directly compare aerosol in situ measurements to AMALi lidar backscatter properties, aerosol optical properties are calculated from measured size distributions using the Mie theory (section 3.1). A realization of the algorithm of Bohren and Huffman (1983), implemented as a matlab function by (Schäfer 2011), is used for this purpose. For a given particle diameter and refractive index, the algorithm returns the scattering, extinction and absorption cross sections and the scattering phase function, through which the differential scattering cross section for backscatter, $C_{scat}(180°)$, can be obtained. Integrating over the particle diameters of a number size distribution yields scattering, extinction, absorption and backscatter coefficients, respectively (see section 3.1).

The Mie calculations are performed for the three measurement wavelengths of the nephelometer at 450, 550 and 700 nm and for the two wavelengths of AMALi at 355 and 532 nm.

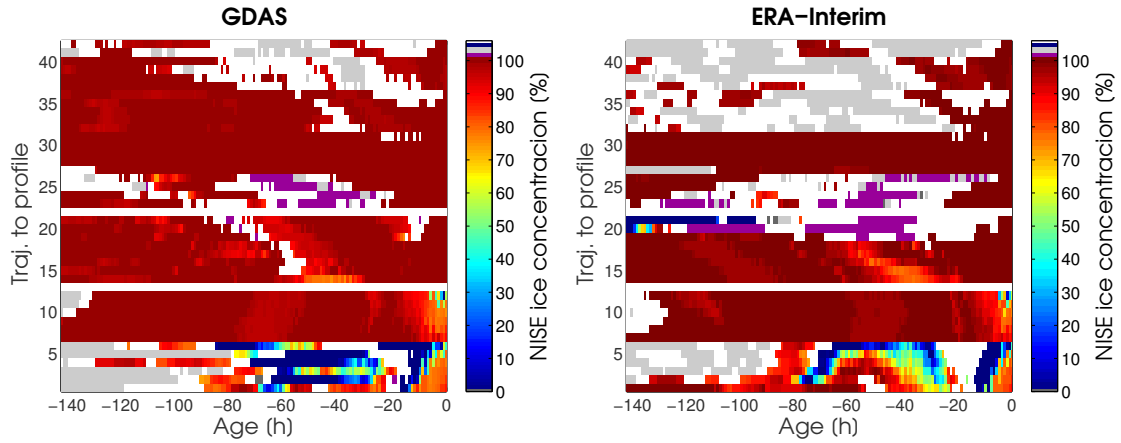

Figure 5.6: Sea ice concentrations along HYSPLIT backward trajectories ending at the locations of the dropsonde profiles of PAMARCMIP 2012 at an altitude of 50 m. The X axis denotes the age of the trajectory with 0 being the time of arrival at the dropsonde location. Magenta indicates the Greenland ice shield, gray snow covered land surface and white ambiguous values in the vicinity of coast lines. (right) Based on ERA-Interim meteorological input fields, (left) based on GDAS input for comparison.

5.3.1 Size distribution

Since the UHSAS measures in a size range between 60 and 1000 nm it covers a large part of the accumulation mode. Particles smaller than 60 nm play a minor role for scattering at the wavelengths of AMALi. However larger particles above 1000 nm, although they occur at low number concentrations, may contribute significantly to light scattering at the wavelengths of AMALi. The size range of the distribution used for the Mie calculations is therefore extended assuming a bimodal distribution that is is approximated by fitting two log-normal modes to the measured data. The bimodal distribution is defined by 6 parameters, namely median diameter $D_{m1,2}$, particle number $N_{1,2}$ and standard deviation $\sigma_{1,2}$. Since the measured size distribution does only include a part of the larger particle mode, the fit would be under-determined with six degrees of freedom. Therefore the number of parameters is reduced by making a priori assumptions about the expected aerosols. The assumptions are then validated by comparing the scattering coefficients retrieved from Mie theory to the nephelometer measurement.

For the larger mode 2, a constant value of the median diameter D_{m2} is assumed as well as a constant standard deviation σ_2. They are set a priori to values for a typical *sea salt accumulation mode* according to the OPAC aerosol data base (Hess et al. 1998), $D_{m2} = 418$ nm and $\sigma_2 = 2.03$ and then adjusted iteratively to yield a good agreement of retrieved scattering coefficients with the nephelometer measurement (section 5.3.2). The integrated particle number N_2 contributing to the mode is varied proportionally to the number concentration measured by the UHSAS for particles larger than $D_{cut} = 726$ nm. This diameter threshold and the factor applied to obtain N_2 were determined empirically to have as small as possible overlap with the accumulation mode, include enough particle counts to obtain a measure for particle number concentration and to yield best agreement with the nephelometer scattering coefficient.

A fit for the smaller mode 1, corresponding to the classical accumulation mode, was tested varying the two parameters D_{m1} and N_1 under the assumption of a constant σ_1

that is adjusted manually to fit the measured distribution. However this fit is not directly used for the accumulation mode in all calculations, since some size distributions differ slightly from the ideal log-normal form. The accumulation mode is well covered by the diameter range of the UHSAS, except for particles smaller than 60 nm that do not contribute significantly to scattering at the wavelengths of AMALi. Hence the measured size distribution could be used directly for the size range of mode 1 by interpolating linearly between the channel diameters. This method is applied up to the threshold diameter D_{cut} = 726 nm. This yields a better correlation for the comparison to the nephelometer where the particle size distribution deviates from the ideal log-normal distribution. Above D_{cut} the sum of the two parametrized modes for the respective size range is always used. Figure 5.7 (left) shows an exemplary size distribution of maritime boundary layer aerosol measured during the flight on 22 March 2012 and averaged over two minutes (black dots). The bimodal fit that was determined according to the method described above is shown as blue line. Figure 5.7 (right) shows the same data plotted as surface size distribution with a linear scale on the Y-axis. The distribution agrees qualitatively with surface size distributions typically found in the Arctic (Seinfeld and Pandis 2006). Note that although the number concentration of mode 2 is two orders of magnitude smaller than the one of mode 1, mode 2 represents a considerable share of the total aerosol surface. This illustrates that mode 2 can not be neglected for the retrieval, since aerosol surface is more closely related to the optical properties than diameter. Larger particles beyond this mode are not sampled by the aerosol inlet and therefore not included in the in-situ measurements. However they are considered to play a minor role in the Arctic atmosphere, since they have short residence times due to gravitational settling and are therefore not advected over long distances (Seinfeld and Pandis 2006).

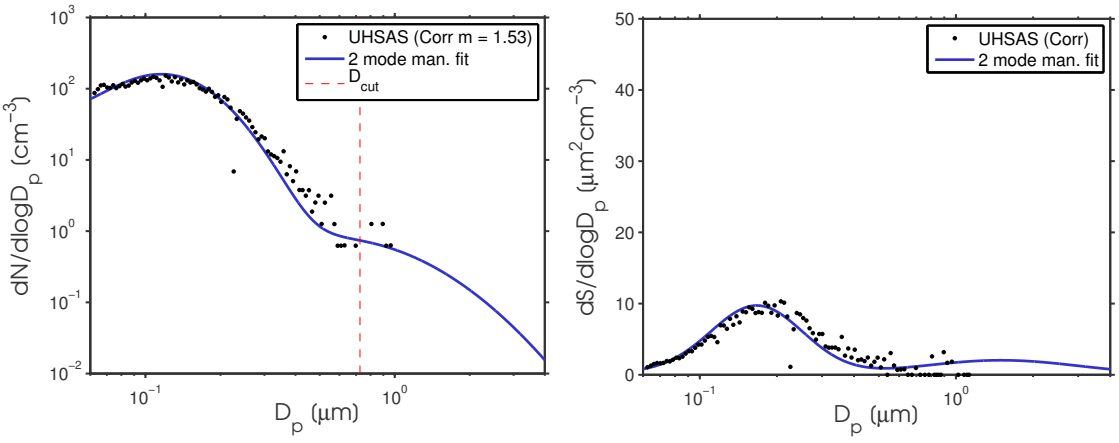

Figure 5.7: (left) Example of a number size distribution for Mie calculation obtained from a UHSAS measurement in the maritime ABL over ocean on 22 March 2012. The standard deviations for the fit are set to $\sigma_1 = 1.51$ for the mode 1 and $\sigma_2 = 2.03$ for the larger mode 2 and the median diameter to $D_{m2} = 550$ nm for the mode 2. The other fit parameters are calculated from the measured size distribution as described in the text. D_{cut} is the cutoff diameter for the parametrization of the larger mode. (right) Surface size distribution of the same data, with a linear scale on the Y axis.

The size Mie calculation is performed for 3500 logarithmically spaced diameter steps D_{Mie}, between 10 nm and 30 μm to cover the size distribution. Further increasing the resolution or size range does not influence the results of the Mie calculation significantly

for the given particle size distributions.

5.3.2 Mie retrieval

The refractive index of the aerosol for the Mie calculations is assumed to be $m = 1.53$, the value for ammonium sulfate ($(NH_4)_2SO_4$) (Toon et al. (1976), Zieger et al. (2010)). The value is considered to be representative for the soluble component of Arctic aerosol by Hess et al. (1998) and not very far from the value for sea salt $m = 1.50$. The aerosol is assumed to be non absorbing. The calculation is not very sensitive to small changes of m, since the value is also used to correct the diameters obtained from the UHSAS measurement, which partly compensates the error.

Figure 5.8 shows a comparison of scattering coefficients retrieved via Mie calculation to nephelometer measurements for the whole flight on 22 March 2012, using the same parameters for the size distribution as for figure 5.7. UHSAS size distributions are averaged over intervals of 10 s before the size distribution fit. The retrieved scattering coefficients show good agreement with the ones measured by the nephelometer for all three wavelengths here. A slope of the regression lines higher or lower than one would indicate a too high or too low absolute particle number concentration for the Mie retrieval. Differences between the regression lines for the different wavelengths are a measure for a wrong assumption of particle diameters. The good correlation for all colors indicates that the parameters used for the size distribution shown in figure 5.7 are valid.

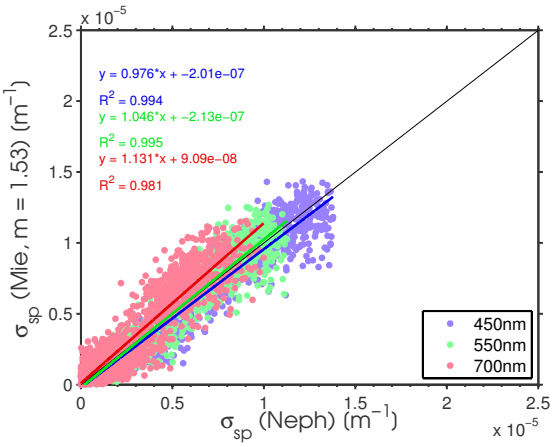

Figure 5.8: Comparison of the scattering coefficients retrieved by Mie calculation to Nephelometer measurements, applying the size distribution parameters from figure 5.7 to the data of the whole flight. Colors indicate the three measurement wavelengths of the nephelometer.

5.3.3 Hygroscopic scattering enhancement

To estimate the potential effect of hygroscopic particle growth on light scattering under the given assumptions, the Mie calculation is performed once for the size distribution that is obtained from measurement under 'dry' conditions as described above, and once for the same size distribution modified by a hygroscopic growth factor $g(RH)$:

$$g(a_w) = \left(1 + \kappa \frac{a_w}{1 - a_w}\right)^{1/3} \tag{5.9}$$

a_w is the water activity that can be replaced by RH for $Dp > 100$ nm where the Kelvin effect plays a minor role. The parameter κ depends on the particle material (Petters and Kreidenweis 2007). The resulting particle size distribution after applying g represents 'wet' conditions. The value of $g(RH)$ is calculated from the actual measured relative humidity, using a value for the parameter $\kappa = 0.57$ that is given as a mean value for ammonium sulfate by Petters and Kreidenweis (2007). The refractive index of the 'wet' particles is calculated by the volume mixing rule

$$m_{mix} = \frac{m_d + m_w \left(g(RH)^3 - 1\right)}{g(RH)^3}, \tag{5.10}$$

where m_d is the refractive index of the 'dry' aerosol and m_w is the refractive index of water, with $m_w(532\text{ nm}) = 1.33$ and $m_w(355\text{ nm}) = 1.43$ for the respective wavelengths of AMALi (interpolated from Seinfeld and Pandis (2006)).

The retrieved scattering enhancement factors are used to discuss the reason for enhanced backscatter values measured by AMALi in the ABL under the influence of sea ice leads (section 7.2).

6 Comparison of ABL heights measured over sea ice

Data of dropsondes and the AMALi lidar from the PAMARCMIP 2012 campaign are used to compare different formulations of ABL height over Arctic sea ice. Since all dropsondes were launched during periods of nadir pointing lidar measurements, profiles of the meteorological variables can be directly compared to coincident backscatter profiles. For the time of each dropsonde launch, AMALi data are averaged over a period of ±10 s to increase the signal to noise ratio and include a representative ensemble of measurements from the area around the descending path of the dropsonde.

ABL heights are calculated applying the criteria introduced in section 5.1 to each vertical profile. Here the same threshold and scale settings are used for each profile, regardless of the characteristics of the respective boundary layer. ABL heights derived from dropsonde profiles are declared invalid if the respective dropsonde did not deliver data below 50 m altitude. AMALi ABL heights are declared invalid if the signal is attenuated by clouds to a value below an empirical threshold that lies considerably below the value for molecular backscatter. An average of attenuated backscatter between 0 and 100 m altitude is therefor compared to the threshold. This criterion does not exclude low clouds, since they lead to high backscatter values and do not trigger the threshold. This is desirable due to the fact that these low cloud tops are likely to represent the ABL height.

Figure 6.1 shows an exemplary comparison of dropsonde variables and AMALi backscatter B_{sum} and the different ABL heights derived from them for the same profile as shown in figure 5.5. The top of this relatively well defined ABL is successfully identified by z_{Tgrad}, z_{Ri1}, z_{Tinfl}, z_{LLJ} and the two AMALi criteria z_{AMgrad} and z_{WL1}. The value of z_{Tgrad} is the lowest and z_{LLJ} the highest one, with a difference of 70 m. The AMALi criteria agree with each other and identify the ABL height in the middle of the capping inversion. The height derived from the layer Richardson number, z_{Ri2} is also shown here. It is obviously not related to any of the other heights. Due to its high sensitivity to local gradients in the wind profile that frequently occur due to gusts, the heights detected from this criterion did not show a clear systematic behavior for the observed cases and are therefore not included in the further analysis.

An overview of different ABL heights for all profiles from PAMARCMIP 2012 is shown in figure 6.2. The heights derived from dropsonde variables are plotted as dots, the height obtained from AMALi via the gradient method as crosses. Note that the plot includes measurements from a latitude range spanning from about 70°N to 86°N as well as a variety of different atmospheric and sea ice conditions. It is evident that there are considerable differences between the various criteria. The disagreement varies between the different flights, representing distinct conditions. However in most cases there seems to be a qualitatively systematic behavior among the different profiles of a single flight. The different criteria shall be compared in more detail here.

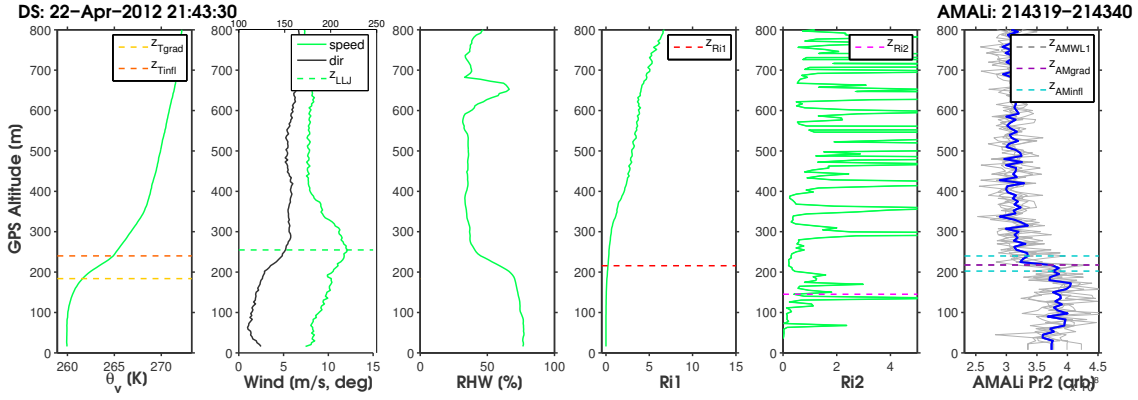

Figure 6.1: Comparison of dropsonde and AMALi measurement for the same profile as in figure 5.5, showing a relatively well defined ABL over sea ice under the influence of a polynya and open leads. The curves in green show virtual potential temperature, wind speed and direction, relative humidity, surface bulk Richardson number and layer Richardson number from the dropsonde. The blue curve to the right is the AMALi range corrected profile B_{sum} that is combined from 532 and 355 nm and averaged over 20 s. Grey lines show averages over 5 s over the same period to illustrate the variability. Different ABL height criteria are indicated as dashed lines.

6.1 Temperature gradient criterion

As figure 6.2 shows (yellow dots), the temperature gradient criterion yields the lowest ABL heights z_{Tgrad} of the four dropsonde criteria evaluated for this study. It is sensitive to an empirical threshold that is based on the assumption that above a certain degree of static stability turbulent mixing is inhibited. Since turbulence is not only generated by buoyancy, but also mechanically, this has to be taken into account implicitly by setting the threshold to a considerably higher value than the dry adiabatic lapse rate. For a convective or neutral ABL the criterion is met slightly above the base of the capping inversion and therefore likely to be a reasonable approximation of ABL height. For a stable ABL however, the height estimate could be arbitrarily influenced by the choice of the threshold, since the influence of wind shear can only be guessed. However, the criterion is still reasonable here, since a gradient in the temperature profile can not only be seen as a measure for stability, but also as an indicator for the presence or absence of turbulent mixing across the respective layer. Any considerable mixing generated by wind shear would in consequence reduce the gradient. Thus a strong temperature gradient indicates the absence of such mixing in a similar way as a gradient in a tracer like particles or water vapor does.

The height z_{Tgrad} is always at the lower end of the different heights obtained here. It shows a strong correlation with z_{Ri} (figure 6.3 a)), but a mean offset of about -29 m. This may be partly explained by the error that is introduced to the temperature profile due to the slow response to the sharp temperature gradient at the inversion that is caused by sensor time lag (see section 5.1.1.1).

6.2 Richardson number criterion

The heights z_{Ri} obtained from the surface bulk Richardson number (red dots in figure 6.2) are mostly higher than z_{Tgrad}, but lower than z_{Tinfl} and z_{LLJ}. Their location relative to

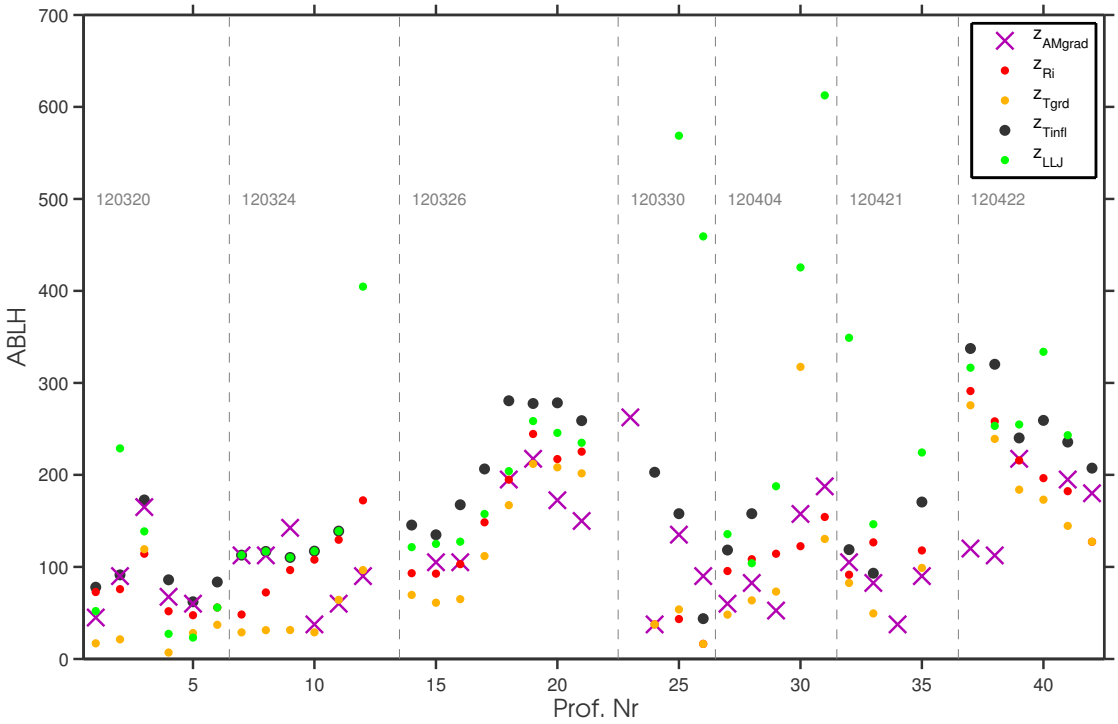

Figure 6.2: Comparison of different ABL heights from dropsonde and AMALi. Different flights are separated by dashed lines with the dates given in the figure.

the other heights seems to vary systematically from profile to profile during some flights, in particular the one on 24 March 2012 (profiles 7-12) where z_{Ri} is close to z_{Tgrad} for the first profile and than rises towards z_{LLJ} over the distance of the flight. This can be explained by the explicit consideration of the wind profile in the Richardson number. As will be discussed in section 7.1, wind speed is more or less constant for the first profiles, while for the later profiles shear up to the altitude of the LLJ increases, leading to higher ABL heights z_{Ri}.

The Richardson number criterion is sensitive to the time lag error in the temperature profile as well, but to a lower degree than z_{Tgrad} due to the additional influence of wind shear that makes the criterion less dependent on the temperature gradient.

6.3 Temperature inflection criterion

The heights obtained from the temperature inflection point criterion (black dots in figure 6.2, note that for profiles 7 to 11 they are identical with z_{LLJ}) are for almost all profiles higher than any of the other heights, except for the low-level jet altitude. Figure 6.3 b) shows a comparison to z_{Ri}. z_{Tinfl} is on average about 40 m higher than z_{Ri}, whereby the difference does not depend systematically on the ABL height. The orange dots show the average of z_{Tinfl} and z_{Tgrad} that is on average equal to z_{Ri}. It may therefore be used as a substitute for z_{Ri} where no wind information is available.

Since z_{Tinfl} marks a locally confined edge in the temperature profile rather than a gradual transition, it is not sensitive to an error in the absolute value of the second derivative. It can be trusted to represent an actual discontinuity in the atmosphere in a more direct way than temperature gradient and Richardson number. The discontinuity at z_{Tinfl} marks the top of the capping inversion of a convective boundary layer or in general of the inversion

associated with an ABL. In general, z_{Tinfl} represents an upper bound for turbulent mixing from the ground and therefore for the ABL. A more detailed comparison to z_{LLJ} follows in the section below.

6.4 Low level Jet altitude

A low level jet is found in many cases somewhere between z_{Tinfl} and z_{Ri}. In general it is expected to occur near the top of a stable ABL. Owing to the commonly used criterion (section 5.1.1.4) a LLJ is not always detected at the top of the ABL, but there can still be a wind maximum meeting the criterion at a higher altitude. There are several cases where the lowest z_{LLJ} (green dots in figure 6.2) is much higher than the other altitudes and obviously not related to the boundary layer. On the other hand there is a possibility of misinterpretation of a wind maximum as LLJ, that is actually a local wind gust related to a large size turbulent eddy. This wind maximum may not be considered a jet due to its very limited horizontal extent. An unambiguous discrimination between a gust and a LLJ is not possible from a single profile, but would require a continuous measurement method like a wind lidar or tethered balloon sounding. Despite the absence of strong orographic influence, gusts that are detected as LLJ occur over Arctic sea ice, but were for example found by Jakobson et al. (2013) in only 10 % of cases they measured between spring and summer.

For the flights '120320', '120324', '120326' and '120422' (figure 6.2), z_{LLJ} seems to follow the overall trends of ABL heights along the respective flight tracks. On '120324' the jet heights match z_{Tinfl} to within the vertical resolution of the dropsondes which is remarkable since the two heights are based two physically independent variables, temperature and wind. This clear relationship between z_{LLJ} and z_{Tinfl} underlines the direct connection of both quantities to physical processes that are reflected in the measured profiles and therefore their validity as upper bounds for ABL height.

For the three flights '120330', '120404' and '120421' there seems to be no correlation between z_{LLJ} and the other heights. This suggests, that ABL heights may not be well defined for these cases.

Figure 6.3 c) shows a comparison between z_{LLJ} and z_{Ri}. Except for the cases of very high z_{LLJ} (excluded from the fit) mostly originating from the three flights mentioned above, there appears to be a high correlation of jet altitude and z_{Ri}. However almost all jet cores are located higher than the top of the turbulent layer as defined by z_{Ri}. Figure 6.3 d) shows a strong correlation to z_{Tinfl}, i.e. to the top of the inversion layer associated with the ABL. Note that some of the points with very high z_{LLJ} are not included in this figure, since there was no detection of z_{Tinfl} for these cases.

The relationship between low level jet altitude and ABL top in terms of both, Richardson number and inversion top, is much stronger here than was found by Jakobson et al. (2013). They concluded from their data that in general there is no significant correlation between low level jet altitude and their definition of z_{Ri}. This may be explained by the different Richardson number criteria used. Their surface temperature was obtained at 10 m, which is lower as the altitude that could be resolved with the dropsondes here, probably leading to a more stable interpretation of the ABL. At the same time their threshold was $Ri_{cr} = 0.4$ in contrast to the $Ri_c = 0.22$ used here. Due to the higher influence of the surface layer in their criterion, the z_{Ri} used here may be more closely related to the inversion height. On the other hand the correlation with inversion top height was also much weaker in their case. They found jets not to be located at some offset below the inversion top as it is the case here compared to z_{Tinfl}. In most cases their jets occurred at much lower altitudes with respect to the inversion top.

This can be seen as a confirmation of the information value of z_{Tinfl} in terms of describing ABL height compared to the classical definition of the inversion top that does not consider the second, but the first derivative of the temperature profile. This definition does not account for the complexity of Arctic inversions that often include several steps in the temperature profile owing to the history of the air mass. Each of these steps can be seen as the footprint of a diabatic cooling process and a lack of vertical turbulent mixing, but only the lowest one is related to the present ABL. This is the step detected by z_{Tinfl} and used here.

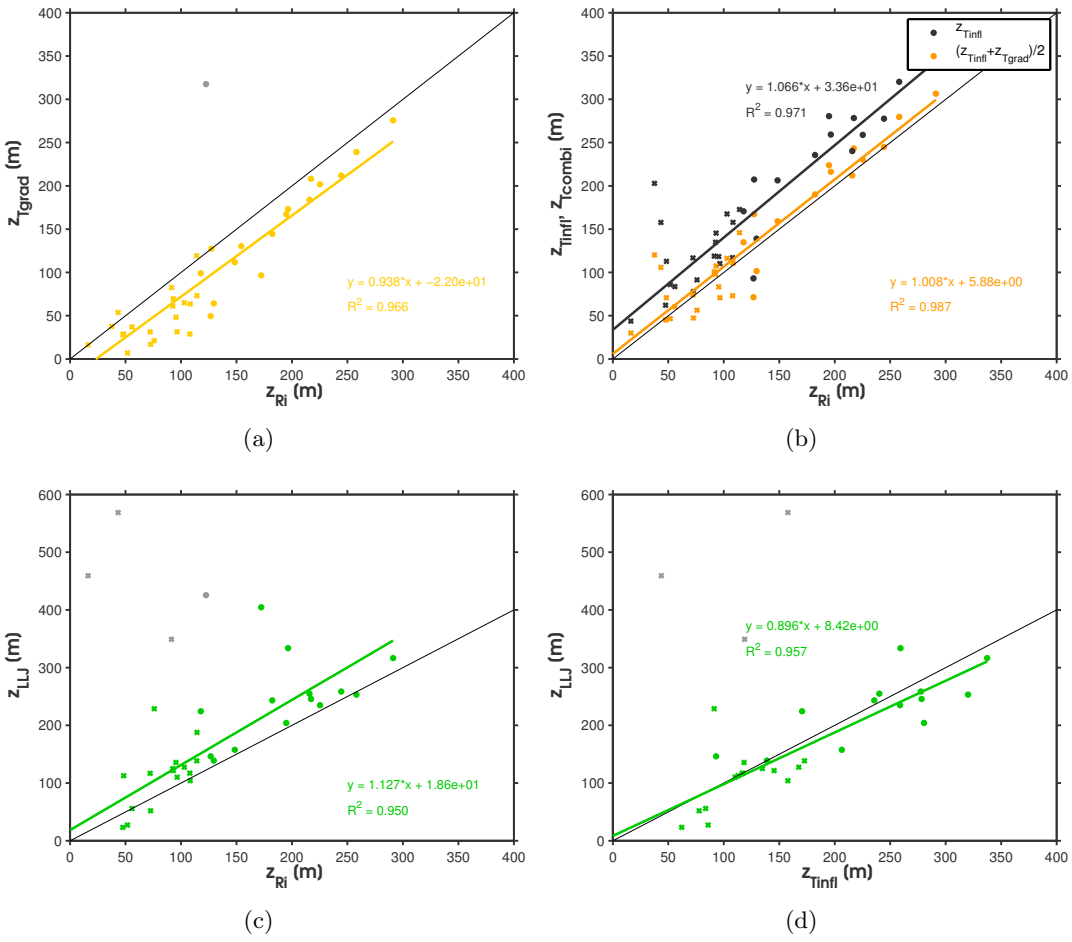

Figure 6.3: Comparing ABL heights derived from dropsonde profiles of PAMARCMIP 2012 using different criteria. a) Temperature gradient vs. Richardson number criterion. Visually identified outliers exceeding the other ABL heights by approximately 100 % are displayed in gray end excluded from the linear fit. b) Temperature inflection and average of temperature inflection and temperature gradient criterion vs. Richardson number criterion. c) Low level jet altitude vs. Richardson number criterion. Outliers excluded as for plot a. d) Same as c vs. temperature inflection altitude.

6.5 Backscatter gradient criterion

ABL heights derived from AMALi backscatter using the gradient method are displayed in figure 6.2 as crosses. Their variation with respect to the heights derived from the different

dropsonde criteria is considerable. Again it deviates between the different flights, owing to different conditions of the ABL. Figure 6.4 a) suggests a correlation to z_{Ri}, but the scatter of the values is relatively large. As will be shown this is caused mostly by the fact that gradients in the backscatter profile can coincide with different meteorological representations of ABL height, depending on the respective conditions.

For flight '120320', z_{AMgrad} is correlated to the general tendency of the dropsonde heights and mostly close to the temperature inflection and Richardson number altitudes. All profiles of this flight included boundary layer clouds that extended to the top of the ABL and caused very strong signal gradients there. The gradient maxima detected by AMALi are in two cases located considerably below the temperature inflection due to the fact that the cloud top altitude can vary over relatively short timescales and the backscatter profiles are averaged over 20 s, i.e. about 1.5 km. Hence the backscatter gradient altitude is an average value that may in fact be more representative for the physical boundary layer conditions than the random sample measured by the dropsonde. The conditions during the flight were characterized by warm air advection over a cold sea ice surface to the north of Svalbard, that lead to a shallow ABL, capped by an inversion under which the clouds developed.

During flight '120324', z_{AMgrad} roughly agrees with the temperature inflection and jet altitudes for the first two profiles, which is caused by a thin stratus layer extending up to this altitude within the capping inversion. Since gradients in the AMALi backscatter profiles can not be determined below the clouds, the actual boundary layer top may be located at a lower level, but z_{AMgrad} represents an upper bound for it. After the end of the cloud layer z_{AMgrad} drops to much lower altitudes that agree with the ones obtained from temperature gradients. The reason is an internal boundary layer developing over open leads as will be further discussed in section 7.1.

AMALi gradient and Richardson number height for flight '120326' agree well except for the last two profiles. As will be discussed in more detail in section 7.1, the high agreement for the first profiles occurs at the top of a thin fog layer extending up to the top of a convectively mixed ABL. This layer is not present at profiles 20 and 21, where AMALi yields considerably lower altitudes than the dropsondes. However visual examination of the AMALi profiles confirms the presence of a persistent discontinuity in the backscatter profiles, suggesting that z_{AMgrad} is more representative for the actual ABL or mixing layer height here than the dropsonde criteria.

A similar behavior of z_{AMgrad} is evidenced for flight '120422' that also probed a convective ABL under the influence of a polynya and open leads. The top of the ABL was characterized by a significant gradient over most of the flight, except for the first two profiles that differ from the dropsonde criteria by more than 50 %. Visual inspection of the backscatter profiles suggests the formation of a weakly stable internal boundary layer here that might be too subtle to trigger the dropsonde criteria. This case will be further discussed in section 7.2.

For flight '120404' there seems to be a correlation between z_{AMgrad} and the dropsonde altitudes as well, although the scatter is relatively large and for profile 29 the height found by AMALi lies considerably below the other criteria. The backscatter profile has an ambiguous structure, although it shows an increase approximately at the altitude of z_{Ri} that is not detected by the gradient criterion.

For flights '120330' and '120421' no correlation can be found to any dropsonde criterion. On '120330' the ABL is very stably stratified with temperatures close to the ground as low as $-37\,°C$. Dry, cold and clean air was advected from Greenland, showing only weak structures in backscatter in the lower troposphere. The actual ABL height is probably located only few meters above the ground and therefore beyond the resolution of the

dropsondes as well as AMALi. On '120421' on the other hand low level fog is present caused by open leads that formed a shallow convective boundary layer. It is easily detected by AMALi, but seems to be embedded in a residual layer that causes the differences to the dropsonde heights.

6.6 Backscatter wavelet criterion

The backscatter wavelet criterion z_{AMWL1} with a constant dilatation set to 112.5 m yields very similar results as z_{AMgrad} criterion, except for six single cases where it detects a much higher altitude than the gradient criterion (figure 6.4 c)). All of these cases occur where the dilation of the wavelet is set too large to detect the ABL height as seen by the gradient criterion, i.e. larger than 61.25 m, half the wavelet dilation. Therefore the next higher layer of decreasing backscatter is detected and erroneously assumed to be the ABL height. For this reason the dilation parameter should not be larger than half of the minimum ABL height that is expected. Where the two criteria agree, they do not show a systematic deviation from each other.

6.7 Backscatter inflection points

Figure 6.4 d) shows the altitudes detected from the next inflection points above (z_{inflU}) and below (z_{inflL}) the respective backscatter gradient altitude z_{AMgrad}. They are a measure for the extent of the transition zone between the higher backscatter of the ABL and the lower backscatter above that can be seen as an entrainment zone caused by the mixing of two air masses. The depth of this transition zone $\Delta z = z_{inflU} - z_{inflL}$ increases with altitude from 30 m at $z_{AMgrad} = 40$ m to 70 m at $z_{AMgrad} = 260$ m according to the linear fits as depicted in the plot. This indicates that the mixing at ABL top occurs over a deeper layer for higher ABL heights. This is consistent with the fact that lower ABL heights are typically associated with more stable conditions, while higher ABL heights preferably occur under the influence of convection or at least a neutral stratification.

The upper inflection point z_{inflU} is relatively close to the temperature inflection altitude z_{Tinfl} for most cases (figure 6.4 b)) This agreement shows the validity of z_{inflU}, since it refers to the top of the entrainment or transition zone, respectively as does z_{Tinfl}.

6.8 Summary

Boundary layer characteristics varied considerably between flights which was to a large extent caused by differences in sea ice cover. Some of the underlying processes will be discussed in detail in chapter 7. Whether the height of an ABL can be unambiguously identified depends to a large extent on these characteristics. The criteria perform differently, depending on the properties of the ABL.

The dropsonde criteria can be divided into two types. Those that rely on quantities directly associated with the causes of stability or instability of the ABL, the Richardson number and the temperature gradient criterion. And those that rely on properties of the wind and temperature profiles that develop in response to the stability of the ABL, the temperature inflection and LLJ criterion.

The latter two can be seen as upper bounds for ABL height. They are not necessarily associated with the present ABL. Discontinuities in the temperature profile may be related to a residual layer and do not allow a statement about the structure of the ABL below, as will be demonstrated on the example of a developing internal boundary layer in section 7.1.

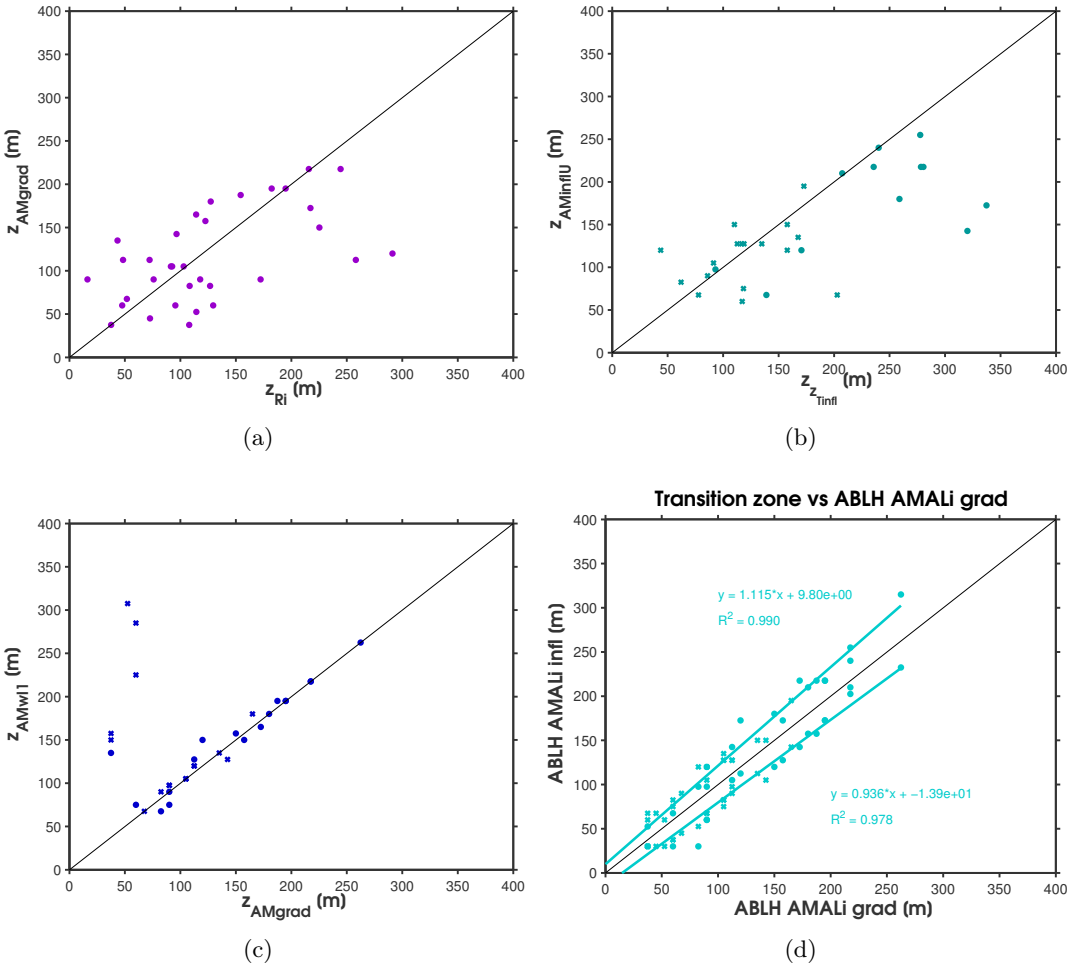

Figure 6.4: Comparing ABL heights derived from dropsonde and backscatter profiles of PAMARCMIP 2012) using different criteria. a) AMALi gradient vs. Richardson number criterion. b) AMALi upper inflection point above gradient altitude vs. temperature inflection altitude. c) AMALi wavelet with dilation 112.5 m vs. AMALi gradient criterion. d) AMALi upper and lower inflection point vs. gradient criterion.

A LLJ is likely to form at the inversion at the top of a stable ABL, but can also occur in stable layers at higher altitudes. Therefore the two criteria can not be considered reliable for detecting the height of shallow boundary layers.

Due to their more direct character, the Richardson number and the temperature gradient criterion are able to detect ABL heights for a broader range of conditions. In particular the Richardson number is applicable under convective as well as stable conditions as it takes into account dynamic instability that is the driving process for turbulence in a stable ABL. The temperature gradient criterion is reliable in case of a convective ABL but generally underestimates the height of stable ABLs here. This is mostly due to the fact that it does not directly account for wind shear.

The detection of ABL height by lidar is more sensitive to atmospheric conditions than the heights determined from dropsonde profiles. The reason is that the backscatter detection methods rely on aerosols and clouds as tracers that mark the ABL. These are affected by a variety of different conditions that are not necessarily connected to the ABL. While

for typical mid-latitude boundary layers a mostly increased aerosol concentration within the ABL due to emissions from the surface can be assumed, this is not in general the case over Arctic sea ice. Where aerosols are emitted at the surface over the Arctic Ocean, this is mostly related to the presence of open water. Since open water is also the main driver for convective ABLs over the Arctic ocean, these can often be detected by lidar. Hygroscopic backscatter enhancement acts in favor of this. However the detection of a layer with increased backscatter does not necessarily imply the detection of a boundary layer, since residual layers can have the same appearance in the lidar signal. Residual layers occur mostly where a water influenced ABL is advected over a cold ice surface and a stable ABL forms beginning from the surface that is not necessarily associated with a change of aerosol backscatter. This means a systematic dependency of the detectability of the convective ABL on the underlying surface.

The detection of a stable ABL by lidar is particularly difficult, because no direct connection exists between the process forming the ABL and the tracer. The detection relies on the accidental presence of an advected aerosol layer that marks an upper bound for the possible ABL height by its gradient or on the formation of fog or haze within the ABL due to cooling from the surface and an associated increase of relative humidity.

Where the criteria of dropsonde and AMALi differ, they do so mostly because AMALi identifies a different layer than the one actually associated with the ABL top. An a priori assumption of ABL height based on a dropsonde profile data is therefore necessary to yield a reliable estimate from the backscatter criteria.

On the other hand in some cases the backscatter detection methods are able to identify very subtle gradients that may indicate the presence of a shallow ABL within a near neutral stratification under low wind shear conditions. The presence of the layers is significant according to thorough visual examination of backscatter profiles, even if they are not detected by the dropsonde criteria. For the detection it is important here to set an approximate threshold for backscatter gradient that is not sensitive to noise.

Table 6.1: Criteria for ABL height and thresholds used.

Instrument	Method	Variable	Threshold
Dropsonde	T gradient	z_{Tgrad}	0.04 K/m
	Richardson number	z_{Ri1}	0.22
	Jet altitude	z_{LLJ}	$\Delta v = 2$ m/s
AIMMS-20	Turbulence (w')	z_{Tur}	visual
AMALi	$\partial/\partial z$	z_{AMgrad}	dynamical
	$\partial^2/\partial z^2$	z_{AMinfl}	dynamical
	Wavelet ($a = 112.5$ m)	z_{WL1}	dynamical

7 Case studies

In this chapter four exemplary cases are presented that highlight different processes which lead to the formation or modification of atmospheric boundary layers over sea ice in interaction with the occurrence of open water regions or leads. All four cases were observed between March 24 and April 22 during the PAMARCMIP 2012 spring campaign at different locations over the western Arctic Ocean. They are chosen to illustrate a broad range of different conditions and the processes caused by them. These processes include the modification of height and stratification of the ABL and influences on aerosol and cloud distribution by turbulent fluxes and mixing. The case studies should be understood as exemplary for typical situations found during the campaign. The focus is set on a comprehensive description and explanation of the underlying processes of the observations.

7.1 Atmospheric influence of the marginal ice zone (24 March 2012)

On a flight on 24 March 2012 a cold air outbreak from closed ice towards the open sea north of Svalbard was observed. The flight track was oriented in northwest - southeast direction and crossing the marginal ice zone (MIZ). The evolution of a pristine Arctic stable ABL via the formation of internal boundary layers caused by decreasing ice concentration towards a fully turbulent ABL with convective roll clouds over open water was evidenced. Aerosol was mixed into the ABL from the free troposphere above as the influence of open water increased. The flight consisted of an outbound low level leg, a vertical ascent up to 3000 m at the northern end of the leg and an inbound leg at 3000 m back on the same track. During the high level leg, lidar measurements were performed with AMALi and six dropsondes were launched.

7.1.1 Meteorological situation and sea ice

The map of 850 hPa geopotential and wind (figure 7.1) shows a synoptic flow coming from the northeast under the influence of two low pressure systems located to the south and east of Svalbard. Air masses originate from the eastern central Arctic and possibly the Kara Sea. Towards the surface the wind direction turns to north for the northern part of the flight and to north-north-east for the southern part, as can be confirmed by the dropsonde wind vectors shown in figure 7.2 (left). Wind speed in the free troposphere was around 7 m/s at the northern end of the leg, increasing to around 12 m/s at the southern end. Within the lower ABL it was increasing from around 4 m/s to around 8 m/s. The wind within the ABL was directed from the ice covered ocean towards open water, a situation known as cold air outbreak (Wacker et al. 2005).

The flight track was crossing the marginal ice zone at around 81°N. To the south, open water extended towards the coast of Svalbard, while to the north the ice concentration increased steadily, from single ice floes to closed pack ice. Figures 7.5 a) and c) show surface temperature and nadir camera ice concentration, respectively, measured during the northbound low level leg. The decrease in surface temperature and ice concentration until

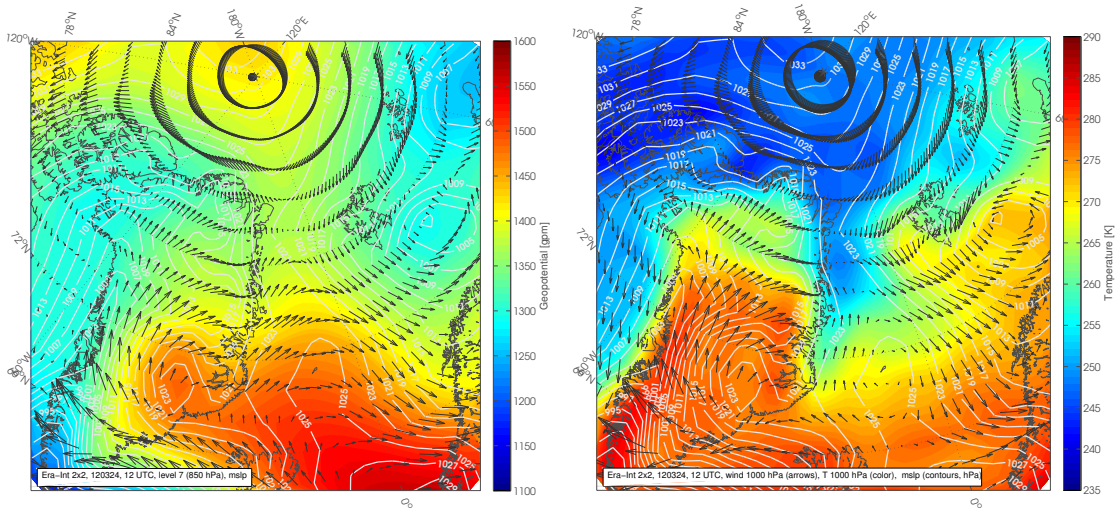

Figure 7.1: (left) ERA-interim geopotential and wind at 850 hPa and mean sea level pressure (white lines), showing the meteorological situation on 24 March 2012 in the vicinity of Svalbard. (right) Temperature and wind at the 1000 hPa level with mean sea level pressure. Note that the 1000 hPa fields are not valid over elevated land surfaces.

11:00 indicates the extent of the MIZ. In the area with closed ice from 11:00 on, i.e. to the north of the MIZ, several single leads occurred sporadically along the flight track.

Since the wind direction is not parallel to the flight direction, the conditions found along the track may not be entirely representative for the ice surface that influenced the ABL that was probed during the flight. HYSPLIT trajectories (figure 7.2, right) show advection relatively parallel to the MIZ and underlying ice concentrations (color coded) over the last 15-20 hours decreasing from DS 1 to DS 6, i.e. from north to south.

7.1.2 Influence of leads on the ABL

The decrease of ice concentration from the northern towards the southern trajectory implies that the ABL in the northern part of the flight path was less influenced by open leads, than in the southern part. This allows to study the influence of open leads on the ABL over sea ice.

7.1.2.1 Northern part, small lead influence

The ABL at the northern end of the flight path was characterized by a shallow inversion at about 100 m altitude. The stratification below this inversion was moderately stable according to dropsonde and collocated in situ profiles of potential temperature (figure 7.4, first DS 1 to 3). Wind speed and direction show a relatively sharp transition at the height of the inversion, indicating a decoupling towards the free troposphere. Winds below the inversion height are relatively constant with altitude, while at the inversion height a low level jet was present. The height of the boundary layer capping inversion z_{Tinfl} increased slightly from about 100 m in the north to about 110 m in the south and was very similar between aircraft and dropsonde profiles. This indicates stationary conditions at the time scale of at least 1.5 hours that passed between the respective aircraft measurement and DS 3.

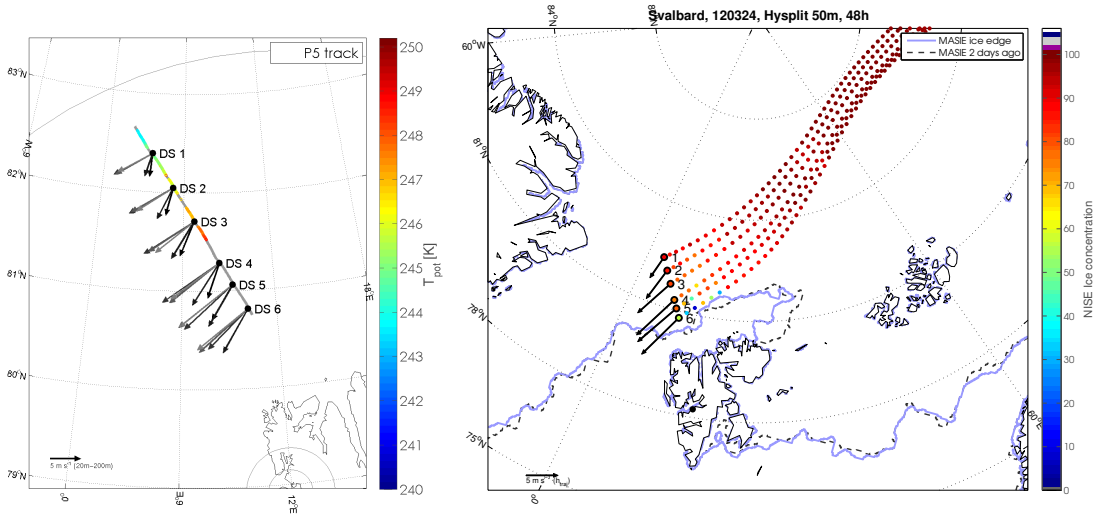

Figure 7.2: Flight track for 24 March 2012. (left) Color coded potential temperature measured during the low level leg for altitudes between 50 and 90 m. Parts of the leg where Polar 5 was flying at different altitudes appear in grey. Arrows are dropsonde wind vectors for different altitudes from 20 m (black) to 200 m (grey). (right) HYSPLIT trajectories ending at the dropsonde locations at an altitude of 50 m. Arrows show dropsonde wind vectors at 50 m altitude. Colors indicate the NISE ice concentration in % (see section 5.2.1). The blue line is the ice edge provided by the MASIE (Multisensor Analyzed Sea Ice Extent) product (Fetterer et al. 2010), with water extending to the south and ice to the north of it. The black dashed line indicates the sea ice extent two days earlier.

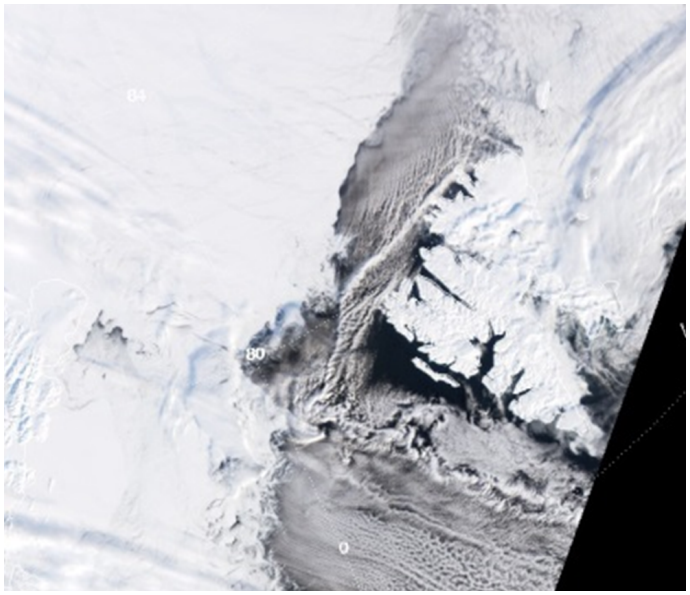

Figure 7.3: MODIS visible swath image from 24 March 2012 showing the area around Svalbard with convective clouds forming during a cold air outbreak over the open water.

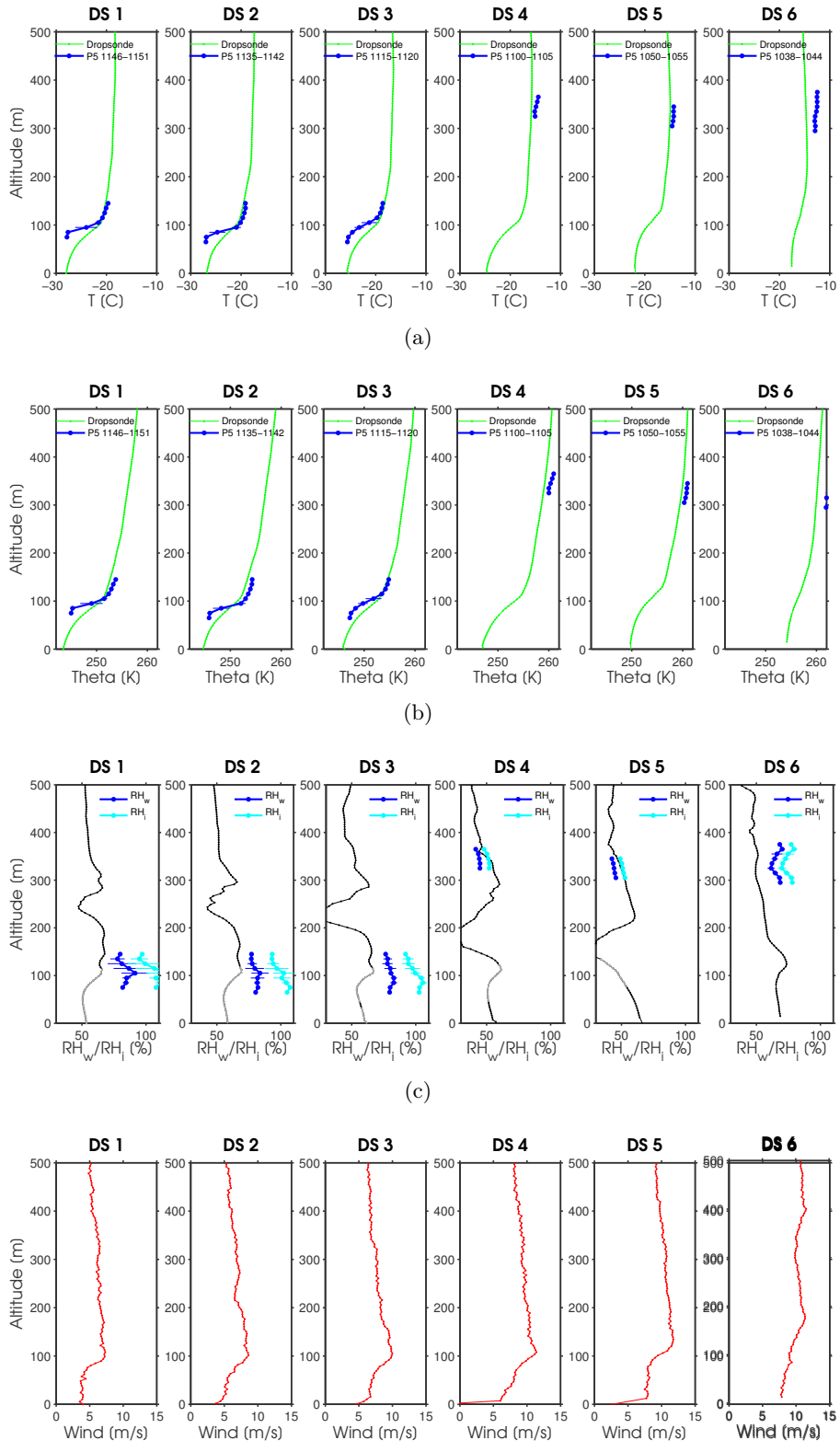

Figure 7.4: Dropsonde profiles from the flight on 24 April 2012 of dropsondes 1 to 6 together with Polar 5 in situ profiles obtained during the low level leg for matching positions, showing a) temperature, b) potential temperature, c) relative humidity and d) wind speed.

Sporadic thin stratus clouds occurred at the height of z_{Tinfl} as can be seen from the backscatter measurement of AMALi (figure 7.9). These clouds trigger the AMALi ABL height detection as was discussed in section 6. They can be expected to act to maintain the sharp gradient at the top of the ABL inversion that can be seen in the Aircraft temperature profiles (figure 7.4) by radiative cooling due to their thermal emission at cloud top.

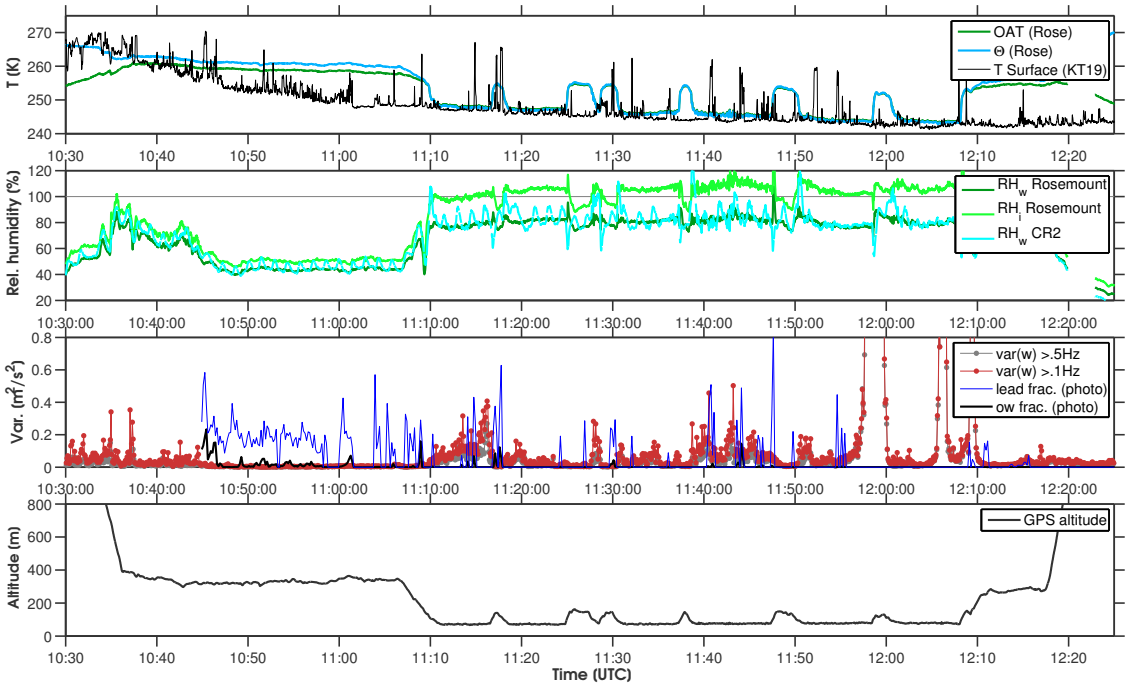

Figure 7.5: In situ measurements during low level leg of the flight on 24 March 2012.

7.1.2.2 Increasing lead influence to the south

In the southern section of the flight, represented by DS 4 to DS 6, the influence of open water on the advected air forming the ABL increases gradually. Air temperature near the surface increases by 7 °C from −24.5 °C at DS 4 to −17.5 °C at DS 6. The strength of the ABL inversion is significantly reduced from about 7 °C to about 3 °C. The height z_{Tinfl} increases slightly, while the discontinuity in the temperature profile is reduced and not well defined anymore for DS 6. This shows the influence of open heat flux from the leads that acts to destabilize the ABL.

To further illustrate the influence of leads on the ABL, the humidity measurement from the low level leg shows a water vapor mixing ratio of about 0.4 g/kg for the southern end of the leg compared to only 0.25 g/kg at the northern end. Temperature at the altitude of the low level leg 70 m also increases from north to south. The ice surface temperature is slightly lower than the air temperature and shows an analogous increase. This increase is probably in response to downward heat flux from the ABL that is heated by the leads and in return warms the ice surface.

The increase of wind speed of the low level jet shown by the dropsondes and its change of direction is consistent with increasing baroclinicity caused by the horizontal temperature gradient. The baroclinicity may also be responsible for the remarkable agreement between z_{Tinfl} and z_{LLJ} for all dropsondes that was already mentioned in section 6 and did not occur during any other flight.

The variance of vertical velocity fluctuations plotted in figure 7.5 (third panel) shows sporadically occurring turbulence at the low level at 70 m that was not always present, but generally disappears during the short low profiles where the aircraft climbed above the top of the ABL. Turbulence appears to be stronger in the vicinity of open leads that are detected from the nadir photographs and can also be evidenced from surface temperature. Figure 7.6 shows two spectra of vertical velocity within the ABL, one from the northern part and one from the southern part of the flight. While the spectrum from the southern part indicates fully developed turbulence for scales smaller than a few hundred meters (larger scales can not be reliably evaluated), the one for the northern part contains a gap with low turbulent intensity ranging down to tens of meters, indicating relatively laminar flow conditions. This illustrates the influence of the leads in mixing the ABL by producing convection.

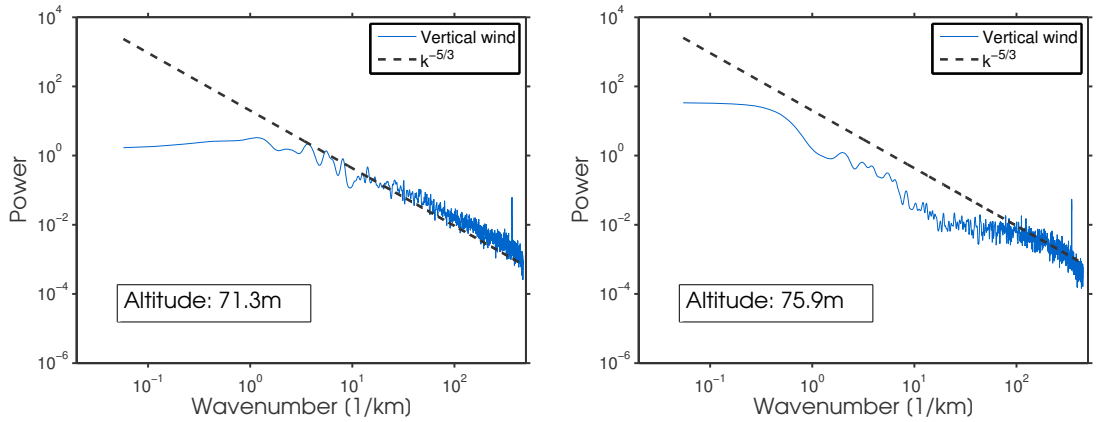

Figure 7.6: Spectra of turbulent fluctuations of vertical velocity measured with the AIMMS-20 probe on 24 April 2012. The dashed line indicates the ideal slope for the inertial turbulent subrange. (left) Southern part of the flight track (11:11:00-11:16:00), (right) northern part of the flight track (12:01:00-12:04:30).

7.1.2.3 Aerosol within the ABL

Figure 7.7 shows low level in situ profiles of aerosol concentrations, temperature and humidity around the altitude of the ABL top inversion for two time intervals of the low level leg (an overview plot of the leg is shown in figure 7.8). The profiles colored in cyan are from the northern part, the ones in dark blue from a more southern, lead influenced part of the flight leg. The consideration of a location closer to the ice edge was not possible using the in situ data, because the flight leg was conducted at 400 m there to avoid turbulence and reduced visibility within the ABL. The profiles are each averaged over an ascent and a descent to reduce the bias introduced from the measurement time lag. Therefore the concentrations at the lowest and highest level are more reliable since they were measured at constant flight levels and more significant since they include more data points. Error bars denote the standard deviation of all data points included in the respective height interval.

For the northern profile, concentrations of both small particles ($D < 100$ nm) and larger particles ($D > 100$ nm) were reduced within the ABL compared to the free troposphere above. This suggests a sink for the particles within the ABL during the advection over the Arctic sea ice.

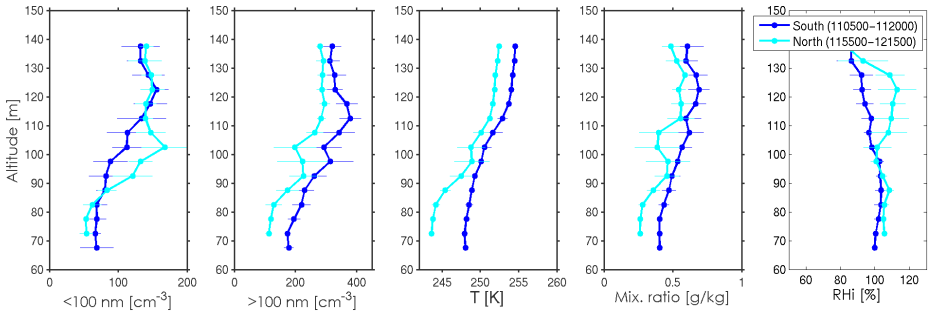

Figure 7.7: Low level profiles of aerosol concentrations for particles smaller than 100 nm and larger than 100 nm, temperature, water vapor mixing ratio and relative humidity with respect to ice at the ABL top inversion on 24 March 2012. Two time periods of the flight leg are compared that are highlighted in figure 7.8.

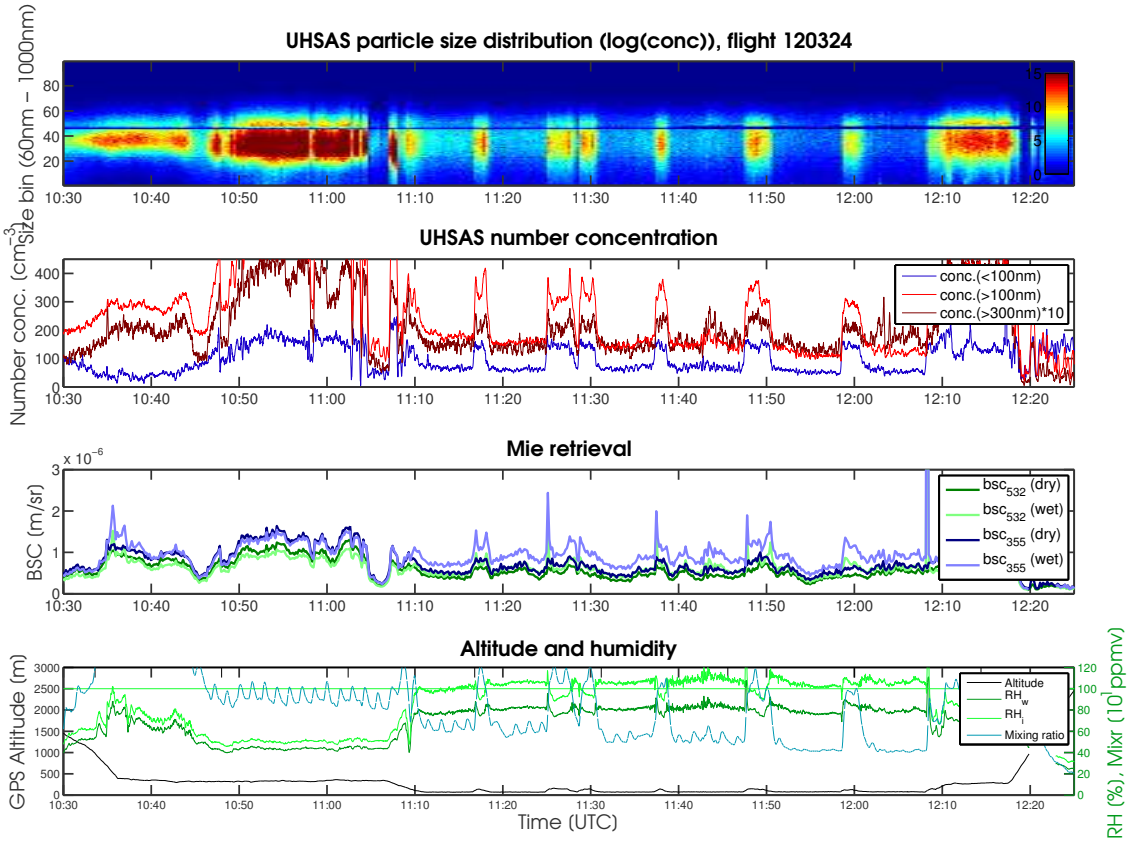

Figure 7.8: In situ aerosol measurements during the flight on 24 March 2012. (Top) Particle number concentration measured by the UHSAS particle spectrometer on a logarithmic color scale for size bins of the instrument with logarithmic spacing between 60 and 1000 nm. (Second) UHSAS and CPC number concentrations integrated over size ranges from 14 to 100 nm, 100 to 1000 nm and 300 to 1000 nm. (Third) Aerosol backscatter coefficients at 532 nm and 355 nm retrieved by Mie calculation for dry and humid aerosol as described in section 5.3. (Bottom) GPS altitude, relative humidities and water vapor mixing ratio. Colored bars at the bottom indicate the time intervals of the vertical profiles shown in figure 7.7.

For the southern profile, the concentration of small particles within the ABL was similar to the northern profile (higher by a factor 1.2), while the concentration of the larger particles was higher within the ABL by a factor of 1.5. In the free troposphere the two profiles did not differ significantly. Assuming that the air masses sampled for the two profiles originally had similar properties, which is supported by the trajectories (figure 7.2) that run closely in parallel above sea ice over a long distance, an influence of the open leads on the aerosol properties can be implied.

There are two possible mechanisms for the increase in large particles: They might be either generated by a source within the ABL or at the surface or transported into the ABL by entrainment from the air above.

A possible source within the ABL would be the emission of particles from open leads. The particles would have to be sea salt, since from a formation of secondary particles from precursor gases an increase of small particles would be expected. Despite the absence of large waves over most leads, Radke et al. (1976) claimed that even a relatively small fraction of open water may be able to produce significant amounts of sea salt aerosol. However this may not apply for the relatively moderate wind speed measured here with values of about 7 m/s close to the surface. At these wind speeds bubble bursting associated with organic particle formation is dominating and sea salt plays a minor role (Nilsson et al. 2001; Leck et al. 2002). The organic processes responsible for this particle formation mechanism are considered more relevant during summer time.

The concentration of large particles could also have increased by cloud processing within ABL clouds, that were possibly generated by humidity increase due to the moisture flux from the surface of open leads. If these clouds had formed and dissolved again without precipitating, the cloud residuals would contain larger particles formed from the mass of small particles and precursor gases (Hoppel et al. 1986). However since the concentration of small particles was not decreased but also slightly increased within the ABL, this process apparently did not play a role here. Also if clouds had formed throughout the ABL within the air mass while traveling over the region with open leads, they should have intensified in terms of liquid water content rather than dissolved, since moisture was added continuously from the leads. The AMALi measurement does only show sporadic occurrence of not very dense cloud layers and a low fog layer that are not related to the location of the increased aerosol concentration.

Besides particle formation within the ABL, mixing of air from the free troposphere into the ABL could have caused the increase of aerosol concentration. Since the aerosol concentration was higher above the ABL than within it, entrainment into the ABL would have caused a net downward particle flux and increased the concentration there. This is in agreement with the reduced vertical stability of the temperature profile and the increased vertical turbulence at the southern profile (figures 7.5 and 7.6). Mixing would be expected to increase the concentration of both, small and large particles. However, the concentration of large particles within the free troposphere was also slightly higher in the southern profile compared to the northern one. Hence the ratio between free tropospheric and ABL concentration was the same for small and for large particles, namely $N_{FT}/N_{ABL} = 2.5$ for the northern and $N_{FT}/N_{ABL} = 1.94$ for the southern profile. The vertical gradient of the concentrations was thus reduced equally by a factor of 0.75 for both size ranges. For water vapor mixing ratio the gradient is reduced by 0.73 which is a very close agreement considering the large error bars for upper data points there. This means that mixing can explain the observed difference of particle concentrations between the two profiles within the ABL, while particle formation is not necessary for the explanation.

7.1.2.4 Formation of a fog plume above open leads

AMALi evidenced the formation of a shallow fog plume within the ABL between 12:52 and 13:10 (figure 7.10). It consisted of several separate parts and extended over approximately 80 km in the horizontal. During the low level leg, open leads had been detected in this region. Since the leads can be expected to extend over some distance perpendicular to the flight track, they were probably also present in the upstream region of the later AMALi measurement. The altitude of the plume top varied considerably between about 40 and 100 m. Backscatter coefficients at 355 nm varied between about 5 and more than $100 \cdot 10^{-6}\mathrm{m}^{-1}\mathrm{sr}^{-1}$. The color ratio is relatively homogeneous within the plume at values slightly below 1. Depolarization (not shown here) is smaller than 5 %, which means that the plume consisted of water droplets. The temperature close to the surface was approximately -25 °C, estimated from dropsonde 4, which is still consistent with the existence of liquid water droplets (e.g. Boronikov et al. (1963)). Unfortunately no valid humidity measurement is available from within the plume, since temperatures were too low for the dropsondes to measure reliable values within the ABL.

The structure of the ABL is interesting here. The dropsonde criteria based on Richardson number, temperature profile inflection and LLJ agree very closely and indicate the ABL inversion top height at around 115 m (DS 3 and 4) and 140 m for DS 5. The temperature gradient criterion detects heights of 30 and 64 m, relatively close to the top of the plume. This is a sign for the formation of a convectively mixed internal boundary layer (IBL) associated with the latent and sensible heat releases from leads that formed the plume. The fact that z_{Tgrad} is sensitive to the formation of this IBL also supports its general reliability in terms of detecting stable stratification close to the surface. The increase of the 'upper' ABL inversion heights to 140 m at DS 5 coincides with the increase of z_{Tgrad} and confirms that the influence of the surface reaches up to this inversion. This illustrates the complicated structure of ABLs over sea ice and the difficulty in defining an unambiguous ABL height.

The variability of the plume top altitude is probably caused by wind driven turbulence as well as horizontally inhomogeneous heat supply from the surface. The backscatter intensity at the lower levels of the plume is to some extent related to the altitude of the plume top with high values where the plume reached to higher altitudes and vice versa. Thus the plume height changes probably in response to the intensity of the surface fluxes that provide water vapor to increase droplet size and concentration on the one hand and latent and sensible heat to intensify convection on the other hand.

At the same time the backscatter coefficient decreased with altitude within the plume. This means that the droplet properties within the plume were not dominated by adiabatic cooling, which would cause an increase of liquid water content and therefore backscatter coefficient with altitude. Instead the mixing with dry air at the top of the plume seems to have caused a partial evaporation of droplets. Here the availability of a reliable and highly resolved humidity measurement would be helpful to further investigate the case.

7.1.3 Formation of convective cloud rolls over open water

Over the open water to the south of the MIZ, the AMALi measurement shows clouds with an inhomogeneous structure. Starting at the surface, the cloud tops increase in altitude with distance from the MIZ. These convective cloud rolls are a typical phenomenon during cold air outbreaks and were for example studied by Wacker et al. (2005). They form as structures of organized convection due to the very large sensible and latent heat flux as the cold air is advected over the warmer ocean surface. The temperature difference between ocean surface and air was approximately 15 °C in this case. The convective rolls are clearly

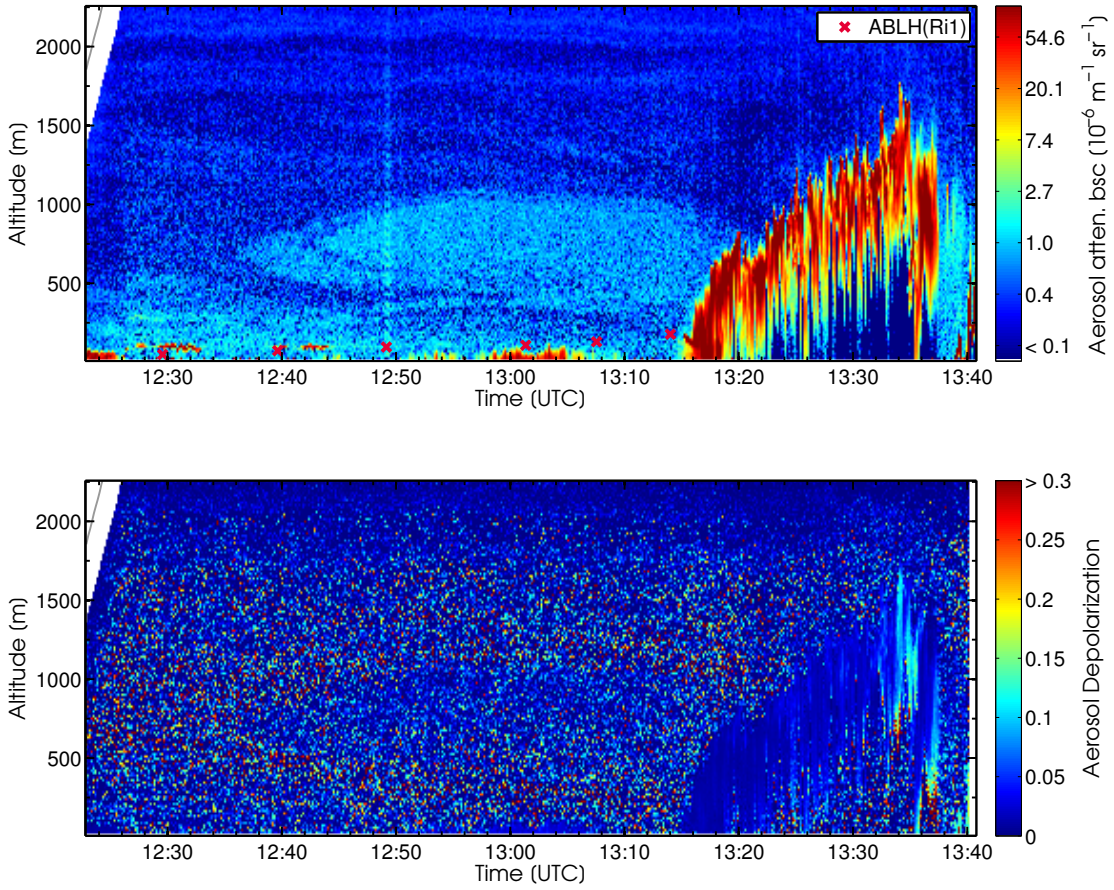

Figure 7.9: AMALi measurement from the flight on 24 March 2012 during the inbound flight leg over sea ice and the marginal ice zone towards open ocean. (top) AMALi attenuated backscatter at 532 nm. Red crosses indicate ABL height z_{Ri} from dropsonde profiles DS 1 (12:30) to DS 6 (13:15). (bottom) Aerosol depolarization at 532 nm.

visible on the MODIS satellite image in figure 7.3. They started at the eastern end of the large polynya to the north of Svalbard and arrived approximately perpendicular to the flight track.

Aerosol depolarization measured by AMALi was lower than 5 % within most of the clouds, indicating liquid water droplets. Only the southern part of the clouds measured around 13:35 shows higher depolarization of more than 15 %, indicating the presence of ice crystals. This is the region where cloud tops reached highest, up to 1500 m which may be the direct explanation for the partial glaciation of the clouds due to adiabatic cooling.

7.1.4 Occurrence of a moist particle layer within the free troposphere

The cross section of the AMALi measurement (figure 7.9) shows an elevated aerosol layer within the free troposphere between about 500 and 1200 m with backscatter coefficients between 1 and $2.5 \cdot 10^{-6}$ $\mathrm{m^{-1}sr^{-1}}$. It is clearly decoupled from the ABL over sea ice by the temperature inversion. To the north it narrows and finally ends in the vicinity of DS 2, while to the south it shows a seamless transition to the high-reaching convective clouds of the ABL over open water. Relative humidity within the layer is enhanced considerably

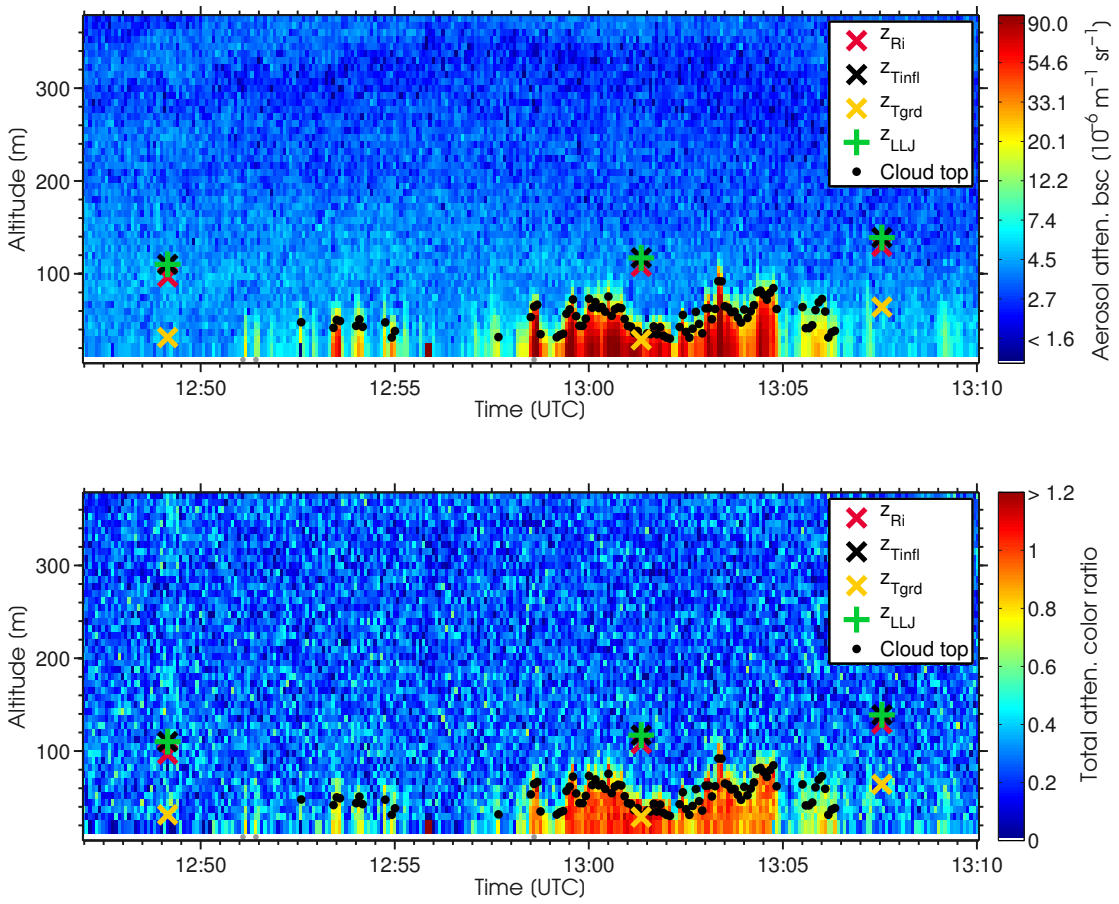

Figure 7.10: Amali measurement on 24 March 2012, zoomed in on the fog plume within in the ABL. Crosses indicate dropsonde ABL heights as described in section 5.1 from DS 3, 4 and 5, black dots the cloud top altitude as described in section 4.2.4. (top) AMALi attenuated backscatter at 355 nm. (bottom) Total color ratio.

up to 60 %, while the atmosphere below and above is relatively dry with values of about 40 % and 25 %, respectively (figure 7.12). The water vapor mixing ratio (not in the figure) shows increased values within the layer as well. This indicates an origin of the layer from a region associated with both particle formation and moisture emission, such as the marine boundary layer.

An interesting explanation of the particle layer would be a formation mechanism associated with the convective roll clouds that were observed during this flight. Aerosol originating from the marine ABL over the large open polynya could have been easily transported up to the free troposphere. This would explain the high humidity as well as the increased backscatter coefficient. A mixing process at the top of the convective cloud rolls, associated with evaporation of the cloud droplets, could have released the aerosol as cloud residuals into the free troposphere. However in order for the aerosol layer to extend to the north, a wind component in this direction would be necessary, for example from a local circulation that was superimposed to the mean wind field. Such a wind component was neither evidenced by the dropsondes nor the HYSPLIT trajectories calculated for endpoints at the dropsonde locations at an altitude of 500 m (figure 7.11) and thus this formation mechanism is ruled out here as a possibility.

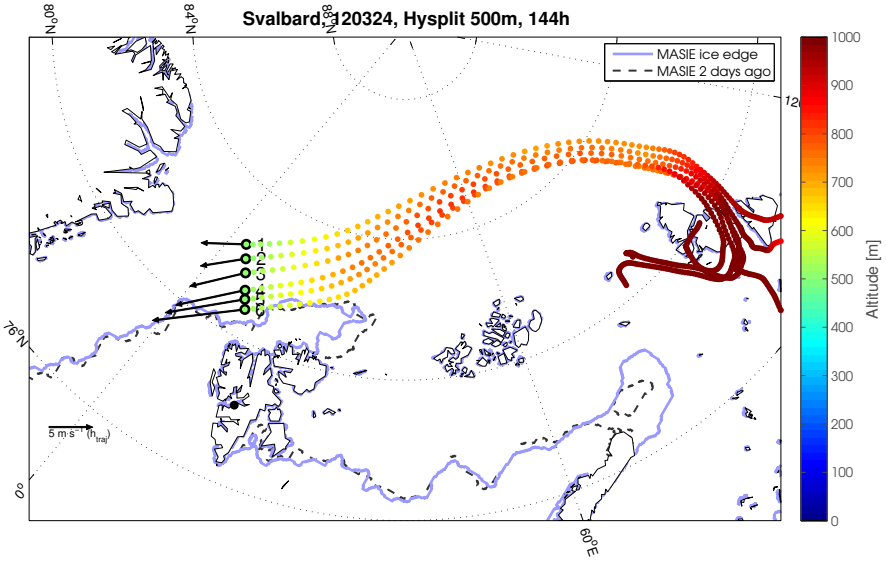

Figure 7.11: Hysplit trajectories for 24 March 2012, ending at the dropsonde locations at 500 m altitude within the elevated aerosol layer. Arrows show dropsonde wind vectors at 500 m altitude. Color coded are the altitudes of the trajectories along their paths. The blue line is the ice edge provided by the MASIE (Multisensor Analyzed Sea Ice Extent) product (Fetterer et al. 2010), with water extending to the south and ice to the north of it. The black dashed line indicates the sea ice extent two days earlier.

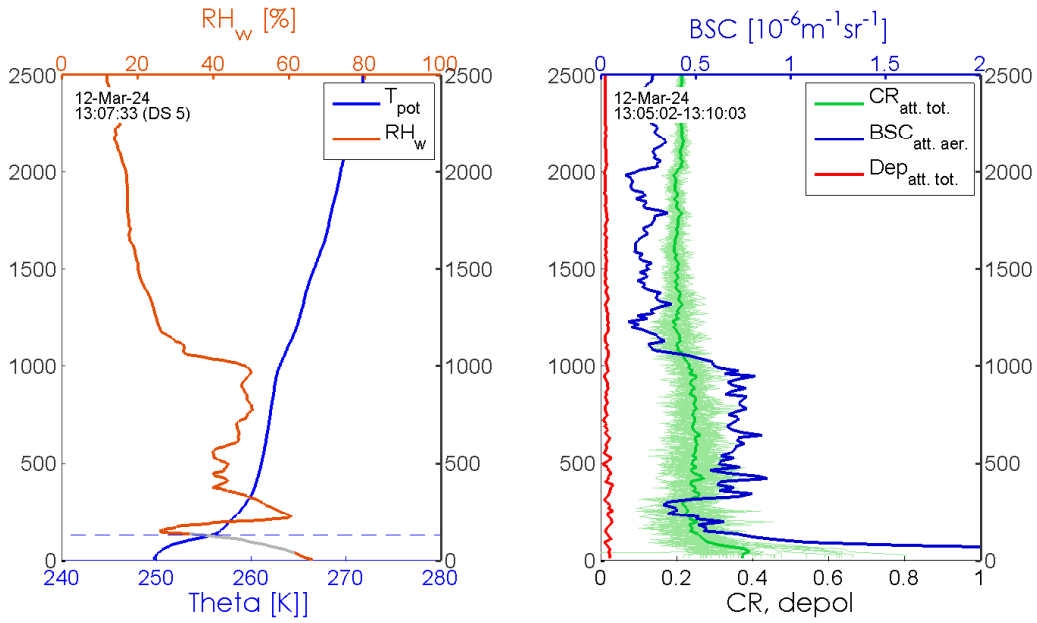

Figure 7.12: (left) Potential temperature and relative humidity measured by dropsonde 5 on 24 April 2012 in the region of the elevated aerosol layer. The dashed line indicates the ABL height z_{Ri}. (right) AMALi attenuated backscatter coefficient, total color ratio and total depolarization ratio averaged over a five minute interval around the launch time of the dropsonde.

Instead the trajectories suggest an advection of the layer from the region of the Kara sea. Due to a stable low pressure system in the region of the northern Barents and Kara seas the trajectories were guided in a relatively well defined path and are therefore assumed to be trustworthy back to the island Severnaya Zemlya where they split up, probably due to a frontal system. The original source of the air can therefore not be assessed further back in time. Possible would be an advection from Siberia or the Laptev Sea. Assuming a lidar ratio $LR = 40$ sr, the optical depth of the layer is estimated as $OD = 0.016 \pm 0.004$. The radiative impact of the layer itself can therefore be assumed to be low, however it may have have had considerable influence on cloud formation in a later process.

Over the ice the layer was separated effectively from the ABL by static stability as can be seen from the persistent layer of low backscatter above the ABL at around 300 m. Over open water the convective cloud rolls most likely caused downward entrainment of the layer into the ABL. In this way they have probably removed a part of the layer from the atmosphere by wet scavenging.

This case shows how the influence of open water can remove aerosols from the free troposphere by destabilizing the ABL and increasing its height. This mechanism may be important as a sink for Arctic haze. It might play a role for the known transition from the springtime, aerosol rich arctic atmosphere towards the summertime, cleaner conditions where small particles of mostly local origin dominate (e.g. Tunved et al. 2013). Wet scavenging was shown to be a part of this process by Garrett et al. (2011), which would be consistent with the frequent occurrence of clouds under the influence of open water.

7.2 Short term influence of open water on advected continental aerosol in ABL (22 April 2012)

During a flight over the Beaufort Sea on 22 April 2012, an enhancement of backscatter within a neutrally stratified ABL was observed that can be directly related to the influence of a developing polynya and a network of open leads in sea ice. Small scale plumes of enhanced backscatter, caused by emissions from nearby open leads, show up within the boundary layer and will be discussed separately. The flight included a low level outbound leg and an inbound leg back on the same track at 3000 m altitude with AMALi and dropsonde measurements.

7.2.1 Meteorological situation and sea ice cover

A high pressure system located over the Beaufort sea on 21 April 2012 advected cold air from the Arctic ocean over the land mass. As the system moved to the south-east towards the coast during the day, wind directions at the coast changed to south-east, redirecting the air that had been transported to the land before back towards the Beaufort sea. This situation continued during 22 April (figure 7.15) and formed the conditions that were present during the flight on this day.

Dropsonde wind profiles show advection within the ABL from south-eastern direction in agreement with the ERA wind field that was used to calculate the trajectories in figure 7.13 (right). The air mass sampled during the analyzed part of the flight arrived from south-east over completely closed ice and then traversed an open polynya that was in the process of formation since several days. The open water fetch of the polynya was up to approximately 50 km in wind direction towards dropsonde 3 and decreasing towards the western and eastern ends of the flight legs. Sea ice was in a state of rapid change driven by shear motions induced by the Beaufort Gyre (Haas 2012), causing a network of open and recently refrozen leads between the polynya and the flight track, as can be seen in the

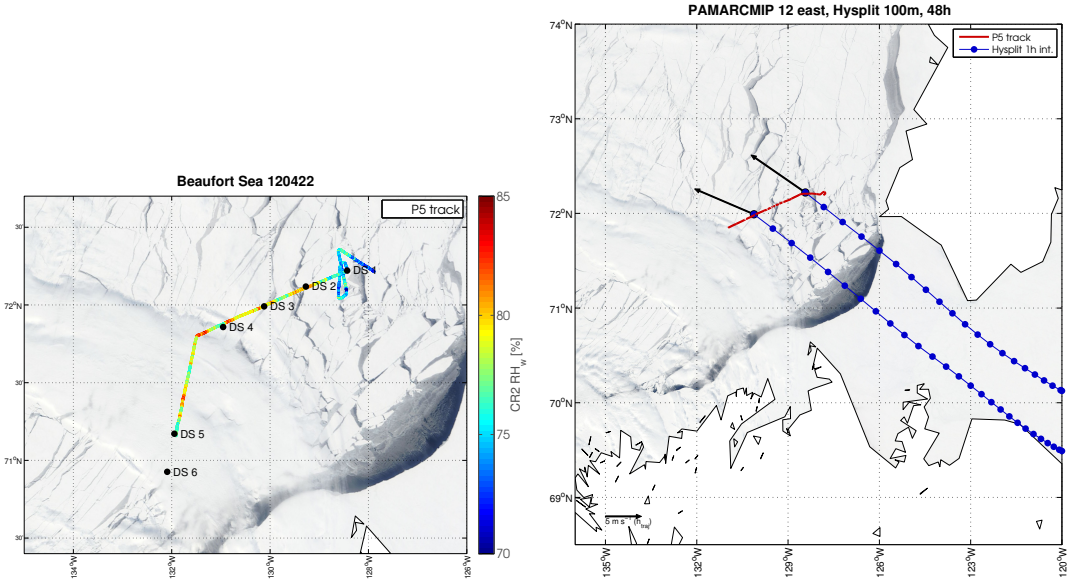

Figure 7.13: Flight track of the flight on April 22 2012 over the Beaufort sea close to Inuvik. The underlying MODIS visible subset image with 250 m resolution clearly shows leads and an approximately 50 km wide polynya. (left) Low-level flight leg with color coded relative humidity measured by the CR2 dewpoint mirror. Dropsondes launched during the returning high level leg are indicated as DS 1 - DS 6. (right) AMALi measurement leg in red, HYSPLIT trajectories ending at two dropsonde locations at 100 m altitude and the corresponding two dropsondes (DS 1 and DS 3) with wind vectors measured at 100 m altitude.

MODIS image in figure 7.14. Open and refrozen leads are not unambiguously discernible from the high resolution visible MODIS image and the KT 19 radiation thermometer was not operating on this flight. However, nadir photographs taken during the low level leg resolve waves on the water surface of open leads and could therefore be used to distinguish between open and recently refrozen leads along the flight path. Leads in the region between DS 2 and DS 4 (figure 7.14) were partly open, while those at the north-eastern end of the track were mostly refrozen.

The height of the ABL varied between about 300 m at the north-eastern and 200 m at the south-western end of the flight track according to dropsonde measurements, applying the threshold $R_c = 0.22$ to the Richardson number. A low level jet existed at the height of the capping inversion for dropsondes 1 to 3, that was decreasing for dropsondes 4 to 5, which may be related to the synoptic situation. Wind speed was relatively constant with altitude within the ABL with values of about 10 m/s at the top and slightly decreasing towards the ground. This and the constant potential temperature with altitude indicate a well mixed ABL.

7.2.2 Lead influence on ABL aerosol backscatter

AMALi observed two regimes of backscatter intensity of the ABL along the flight track (figure 7.17). At the beginning of the leg at the north-eastern end, backscatter at 532 nm in the boundary layer (red crosses show ABL height measured by dropsondes) does not show any significant difference to values in the free troposphere. Towards the south-west, starting from about 21:37, the ABL shows enhanced backscatter with a sharp gradient separating

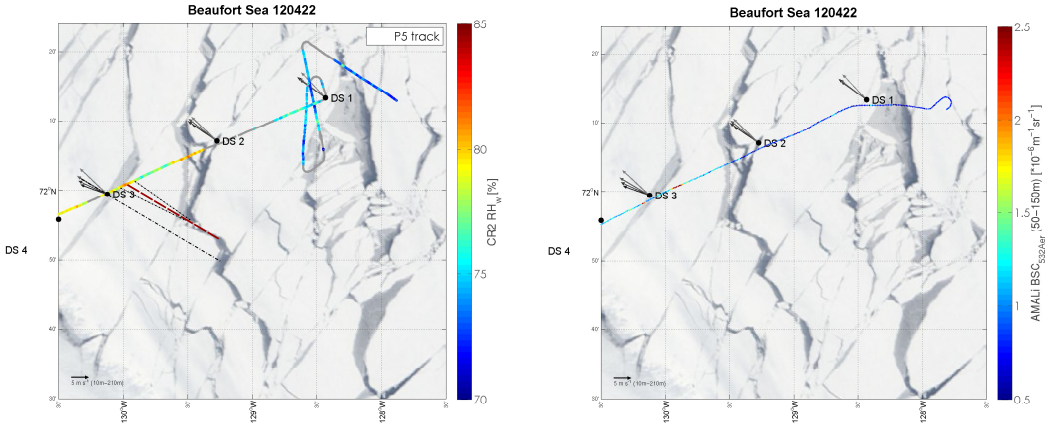

Figure 7.14: Zoom on the north-eastern part of the flight track for 22 April 2012. (left) Relative humidity measured during the low level leg for altitudes between 50 and 90 m. Parts of the leg where Polar 5 was flying at different altitudes appear in grey. (right) Backscatter at 532 nm measured by AMALi during the high level leg, averaged from 50 to 150 m altitude. Dropsonde wind vectors from 10 m or the lowest measured altitude, respectively (black), to 210 m (gray) are shown. MODIS image as in figure 7.13.

it from the free troposphere at the ABL height measured by the dropsondes. Together with the neutral stratification in the ABL this suggests a source of a tracer located at the ground that enhances backscatter. This could be either a source of large aerosol particles, or a source of humidity that causes hygroscopic growth of particles or the formation of ice particles or water droplets. The polynya and the fresh, open leads in the air advection path are a source of water vapor to the ABL as well as a possible aerosol source and therefore a possible cause for the enhanced backscatter values.

Dropsonde 1, located in the low backscatter part of the flight, shows a relative humidity of 69 % close to the surface. Dropsonde 3 in the high backscatter part measured about 77 % close to the surface. Measurements of the CR-2 dewpoint mirror (figure 7.14, north-eastern part of the track) from the earlier low level flight leg also show relatively lower background values of 74 % in the low backscatter region and higher background values of about 79 % in the high backscatter region. Here they also show inhomogeneities with locally increased values for short parts of the track, that will be discussed in the next section. The slight differences between the humidities measured by dropsondes and CR2 may be attributed to not completely stationary conditions. However they both show a qualitatively similar difference between the two backscatter regimes. Considering relative humidity as a tracer for the influence of open water, the enhanced backscatter region can be connected to a higher open water influence on the advected air masses than the low backscatter region.

Humidities measured are below saturation both for ice and water, and hence ice particles or water droplets can be excluded as source for the enhanced backscatter. Unfortunately no aerosol in situ measurements are available for this flight, so a change of aerosol number concentration can not be excluded or confirmed based on the measurements. A possible mechanism causing such a change would be the generation of sea salt particles from sea spray over the polynya caused by the relatively strong wind. The large fetch of the polynya might allow sufficient wave formation to generate sea spray and form a sea salt aerosol mode contributing to the backscatter enhancement.

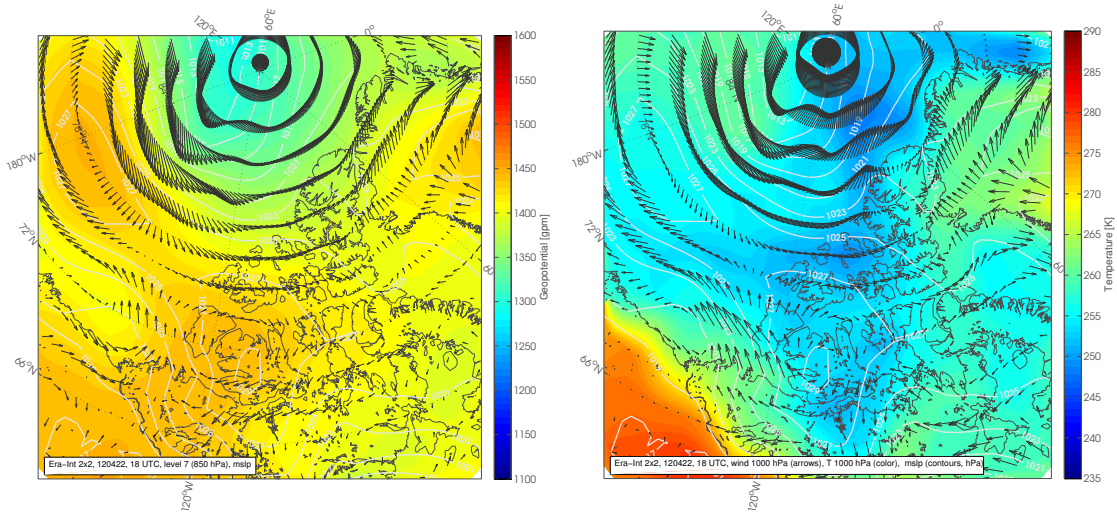

Figure 7.15: (left) ERA-interim geopotential and wind at 850 hPa and mean sea level pressure (white lines), showing the meteorological situation on 22 April 2012 over the Beaufort sea. (right) Temperature and wind at the 1000 hPa level with mean sea level pressure. Note that the 1000 hPa fields are not valid over elevated orography.

The second mechanism that may enhance backscatter is hygroscopic growth of particles by the increased relative humidity. Scattering enhancement factors were calculated using the Mie theory under the assumption of spherical particles. Since no in situ aerosol measurement is available from this flight and the advected air was influenced by open water from the polynya, a bimodal sea salt aerosol was assumed based on a UHSAS measurement of maritime aerosol close to Svalbard on 22 March 2012. The retrieval was performed as described in section 5.3.3 with the parameters of the two modes as found for the maritime ABL. These are $D_{p1} = 120$ nm, $\sigma_1 = 1.51$, $N_1 = 68$ cm^{-3}, $D_{p2} = 550$ nm, $\sigma_2 = 2.03$ and $N_2 = 1.5$ cm^{-3}. The resulting scattering and backscatter enhancement factors as a function of relative humidity are shown in 7.18. The backscatter enhancement factor between the two humidity regimes measured by the CR2 is $f(RH = 79\%)/f(RH = 74\%) \approx 1.16$. Enhancement measured by AMALi between the two regimes is $\beta_2/\beta_1 = 1.4$, averaging over the ABL in figure 7.19. To reach this value, a humidity of about 85 % would be needed according to the retrieved scattering enhancement factors. However, taking into account the uncertainties resulting from the assumptions that had to be made, a considerable part of the scattering enhancement may be explained by hygroscopic particle growth.

7.2.3 Single plume generated by open lead

Within the enhanced backscatter region observed by AMALi, some distinct features of considerably higher backscatter are visible between 21:41 and 21:44 (figure 7.17) that appear to be plumes within the ABL. To investigate the origin of these features, a horizontal profile of backscatter averaged over altitudes from 50 to 150 m is overlaid the MODIS satellite image (figure 7.14, right). The largest plume is visible in red colors east of DS 3, a smaller one west of it. Backscatter is enhanced against the background by approximately a factor 3 to values of $\beta_{aer,532} \approx 5 \cdot 10^{-6}$ m^{-1}sr^{-1}. In the same region the relative humidity measured during the low level leg was considerably increased with peak values of $RH_w = 82$ %. Due to the time difference of 1.5 hours between the two measurements at a wind

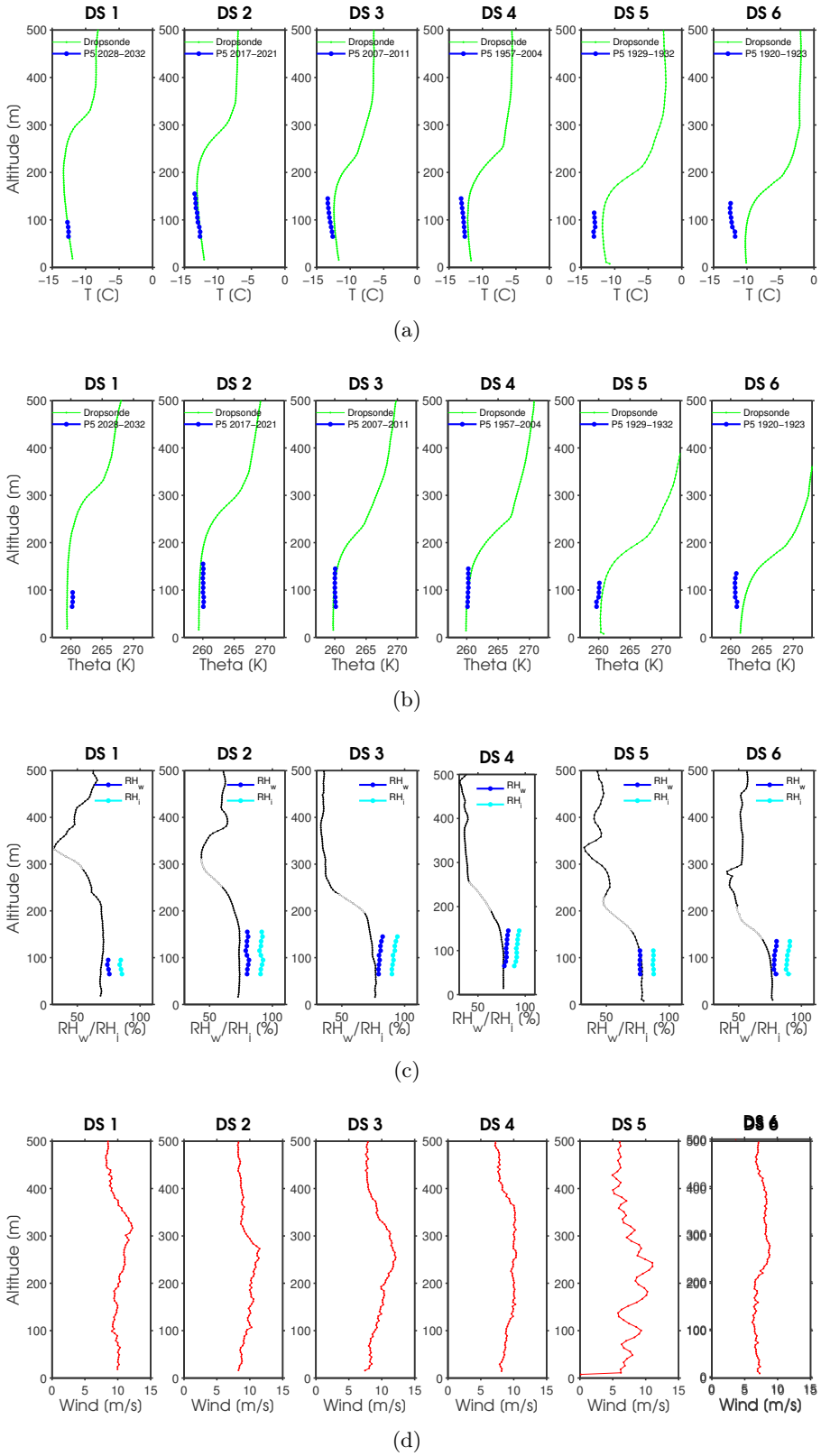

Figure 7.16: Dropsonde profiles of dropsondes 1 to 6 with Polar 5 in situ profiles obtained during the low level leg for matching locations for 22 April 2012, showing a) temperature, b) potential temperature, c) relative humidity and d) wind speed.

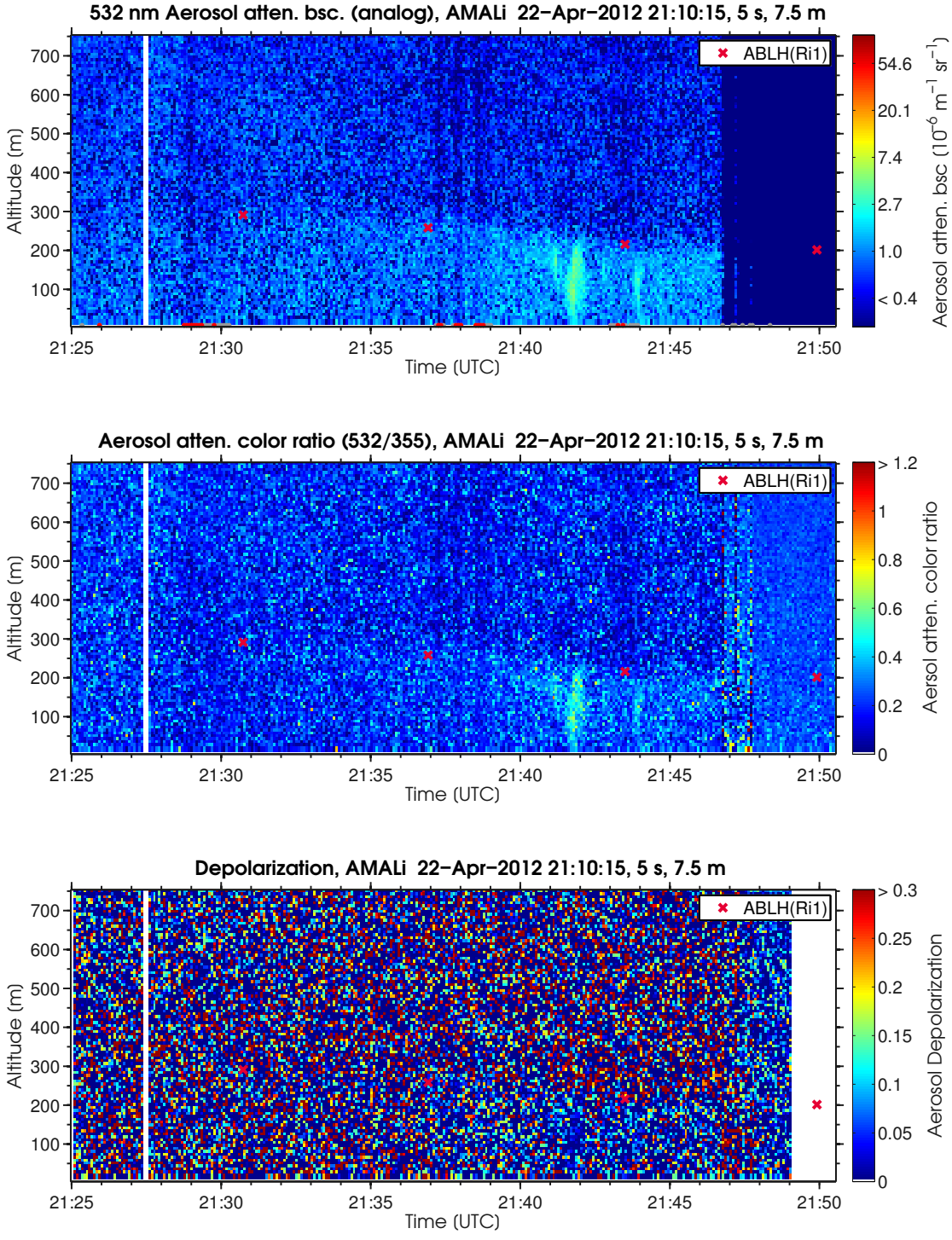

Figure 7.17: AMALi measurement on 22 April 2012 over the Beaufort Sea with a time resolution of 5 s and height resolution of 7.5 m, zoomed in on the enhanced backscatter ABL. (top) Aerosol attenuated backscatter at 532 nm, (middle) color ratio and (bottom) aerosol depolarization. Red crosses denote the ABL height from dropsonde Richardson number with $R_c = 0.22$ for DS 1 to DS 4. Red bars at the bottom of the first plot show the positions of leads identified from the AMALi background signal (section 4.2.5).

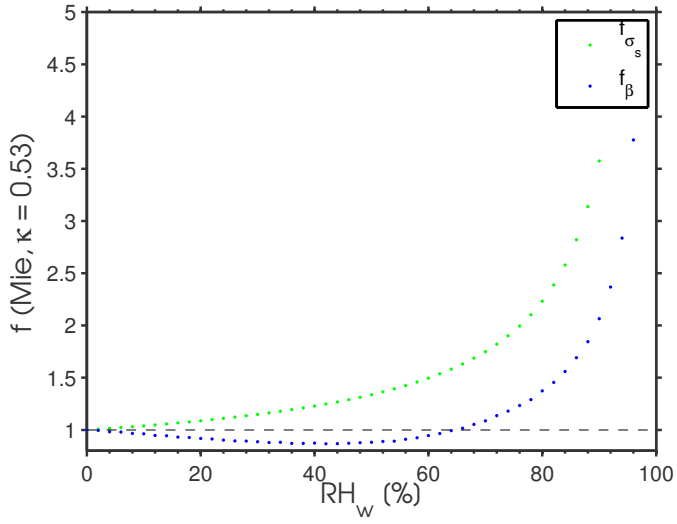

Figure 7.18: Total scatter (green) and backscatter (blue) enhancement factors retrieved via Mie forward calculation. The aerosol size distribution is based on the assumption of a bimodal size distribution as it was retrieved for the maritime ABL on 22 March 2012.

velocity in the ABL of 10 m/s, they definitely do not show the same air parcel. However they might show the same stationary process, i.e. a plume that originates from a lead upwind of the flight track and is advected towards the track. It can be expected that such a plume would undergo fluctuations driven by turbulence of the flow, and therefore show variations of its intensity over time. The two measurements may therefore not be directly comparable, but show different states of the same advected plume.

The most likely source for the humidity increase is the lead located to the south-east of the plume location as can be shown by drawing a line parallel to the 150 m wind vector of DS 3 through the plume center (figure 7.14, left). The direction of the lead yields a long effective fetch parallel to the wind direction here, allowing air masses passing over it a long period of time to accumulate water vapor emitted by the lead. This would explain the contrast to the parts of the lead running perpendicular to the wind direction and apparently not producing plumes visible for AMALi. The spreading angle of the plume can be estimated, assuming a point source at the end of the lead, to be about ± 7 degree. This is at the low end for values that one would expect for turbulent dispersion of atmospheric plumes under neutral conditions (Stull 1988). The moderate vertical wind shear is in agreement with this relatively small angle.

The approximate width of the large plume perpendicular to the wind direction as observed by AMALi is $\Delta x \approx 5$ km, which is similar to the horizontal extent of the region of increased humidity during the low level leg. In the vertical it extends from the ground to the top of the ABL at about 220 m. Backscatter values are highest in the core region of the plume and decrease towards the sides as well as towards its top and bottom, probably caused by entrainment into the plume core. The same is the case for relative humidity and water vapor mixing ratio in the horizontal. High color ratio values indicate the presence of large particles. Liquid water droplets and ice particles did not exist during the humidity measurement, since relative humidities do not reach saturation even with respect to ice. AMALi does not show enhanced depolarization, which would be expected in case of the presence of ice particles. On the other hand the high backscatter values in the plume are unlikely to be caused by an increased aerosol number concentration, since this would re-

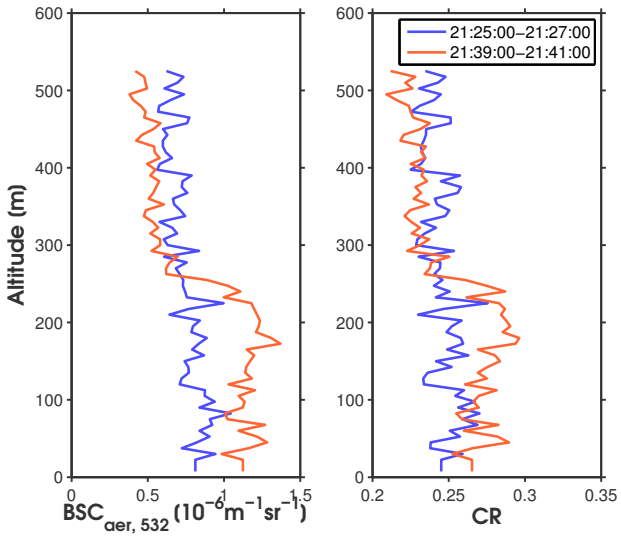

Figure 7.19: AMALi profiles of attenuated backscatter (532 nm) and attenuated color ratio averaged over two minutes within the low and high backscatter region, respectively. Backscatter averaged from 0 to 220 m is increased by a factor 1.4 from the first to the second profile, color ratio by a factor 1.1

quire a strong local source of particle emission that one would not expect from the small open water surface of the lead. Applying the relative humidity measured by the CR-2 hygroscopic particle growth would be too weak to explain the scattering enhancement as well, but taking into account fluctuations of the relative humidity over time, values of the scattering enhancement factor of $f_\beta = 3$ would be reached for humidities approaching 95 %. Hygroscopic growth is therefore a possible explanation for the occurrence of this plume.

The case illustrates how open leads and polynyas can influence backscatter in the ABL on a large scale as well as by introducing smaller scale plumes, that can persist over considerable distances downstream of their source. These plumes might become the origin of clouds forming within the ABL, if more moisture is added by additional leads located downstream of the measurement location.

7.3 Modification of a residual layer under lead and cloud influence (26 March 2012)

During a flight on 26 March to the north of Station Nord, Greenland, the formation of a haze layer containing ice particles, that was caused by humidity emission above open leads was observed. The layer developed as an internal boundary layer within an advected maritime residual layer. The flight consisted of a low level outbound leg during which sea ice thickness was measured with the EM bird, and an inbound leg at 3000 m altitude with lidar and dropsonde measurements. Conditions were clear near Greenland with increasing low stratus cloud cover and light fog formation causing poor visibility of the horizon during the low level leg. The flight course was therefor corrected towards north-west to avoid the fog for EM-bird operation (figure 7.22, left). During the same period an increasing number of partly open leads was visually observed in the vicinity of the flight track and the pilots reported increasingly turbulent conditions at flight altitude ($\approx$ 80 m). From the northernmost point the return flight was continued with an ascent to 3000 m and then at this level first eastwards of the outbound leg and then meeting the original track. During

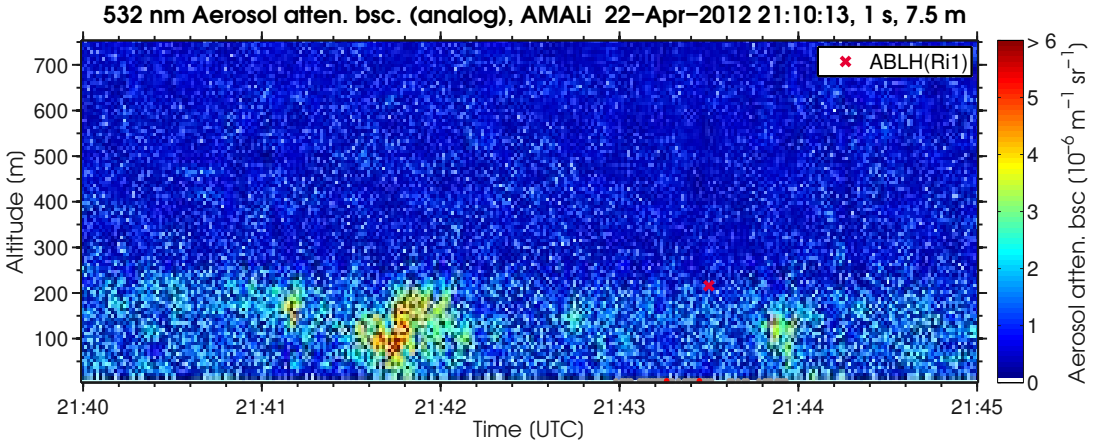

Figure 7.20: Same as figure 7.17 a), but zoomed into the plume region with a time resolution of 1 s and adjusted linear color scale. The red cross denotes the Richardson number ABL height from DS 3.

the leg at 3000 m, AMALi was measuring in nadir mode.

7.3.1 Synoptic situation

Figure 7.21 shows geopotential and wind at 850 hPa and temperature and wind at 1000 hPa from ERA-Interim reanalysis at 12 UTC. White lines are surface pressure contours in both plots. Wind is coming from the south at the 850 hPa level, driven by a low pressure system to the north of Greenland and forming a warm front in the region of the flight. Close to the surface the wind turns to north-west, advecting cold air masses from the central Arctic Ocean below the warm air in the opposite direction. The cloud system that can be seen in the cross section of AMALi backscatter (figure 7.26) is likely to be caused by large scale lifting motion due to the front.

Wind vectors from the dropsonde measurements in figure 7.22 (right) show a very sharp turn of the wind direction with altitude above the boundary layer from WNW to about SSE for dropsondes 1 to 5, which are located at or near the cloud system. The measurements confirm the existence of a shallow front here. The boundary layer with its cold air masses was decoupled from the residual layer and the free troposphere above. For dropsondes 6 to 8 the gradient is getting smoother and extends over the complete residual layer. In the cloud free region a temperature inversion extended from the top of the ABL to about 1700 m (not shown in the plots). Vertical mixing within the clouds caused near neutral stratification in the cloud layers that was confined from below by the inversion above the top of the ABL.

7.3.2 Advection from low towards high level legs

The wind measurements of dropsondes 1 to 4 show advection from directions approximately matching low-level in situ profiles measured during the western low level leg before. Therefore these profiles and the dropsondes can be directly compared (figure 7.23). Dropsonde 5 is compared to a profile that is not directly located in the advection path but further to the north. Due to the low temperatures of less than −30 °C within the ABL the dropsonde temperature and humidity sensors were reacting very slowly to the sharp transition at the ABL top inversion and hence have a large error in their absolute values in the upper part

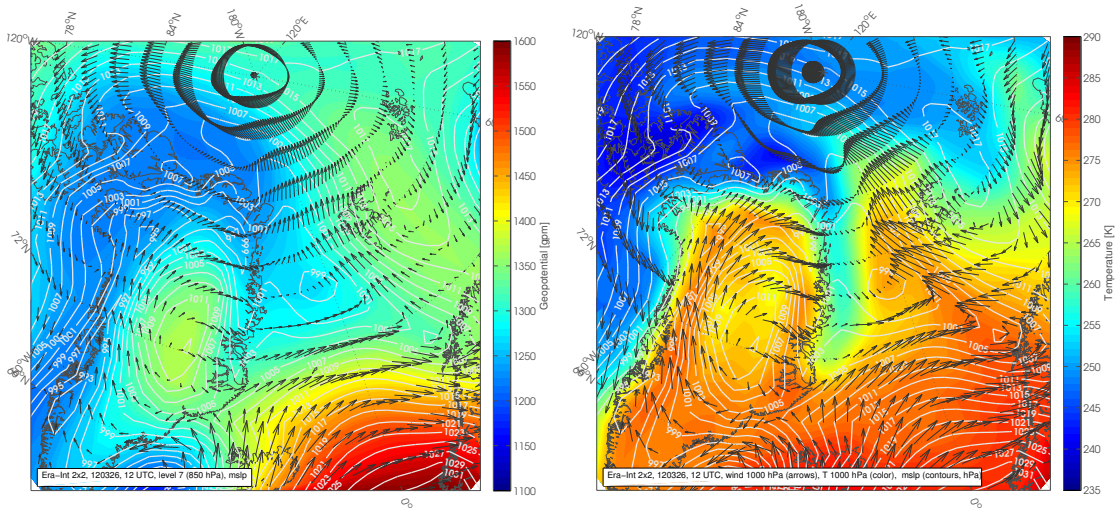

Figure 7.21: (left) ERA-interim geopotential and wind at 850 hPa and mean sea level pressure (white lines), showing the meteorological situation on 26 March 2012 between Greenland and Svalbard. (right) Temperature and wind at the 1000 hPa level with mean sea level pressure. Note that the fields at 1000 hPa are not valid over elevated orography.

of the ABL. However the inversion heights are represented by slight edges in the potential temperature profiles and jet maxima in the wind profiles. The inversion heights seen by dropsonde and respective in situ profile match to within ±20 m for dropsondes 1 to 4. At the locations of DS 5 and 6 the aircraft was not reaching the top of the ABL. Inversion height increases from north to south, but only slightly along the wind advection path.

Potential temperatures for the ABL can be estimated from dropsondes as well as from Polar 5 profiles. Despite the large error after falling through the inversion, dropsonde profiles suggest an approximately constant potential temperature for the lower part of the ABL. The Polar 5 profiles at the same time show only small changes in potential temperature between 70 m altitude and shortly below the inversion. They indicate weakly stable to neutral conditions. Due to the strong winds that are relatively uniform within the ABL in speed and direction, the stratification within the ABL can be considered to be near neutral. The critical Richardson number $R_c = 0.22$ is reached approximately at the height of the inversion for all dropsonde profiles.

For the location of dropsonde 5, the tracks of the low and the high level leg match in position, with a time difference of 153 min. Therefor comparing the measurements of P5 and dropsonde at this point provides a measure for stationarity. The difference in potential temperature is positive with $\Delta\Theta = 0.4\,\mathrm{K}$, yielding only a slow temperature increase of $\frac{\Delta\Theta}{\Delta t} = 0.16\,\mathrm{K/h}$. The situation may thus be assumed to be quasi stationary over the time scale of the flight for this location, despite the rather complicated synoptic situation shown by the ERA-Interim data.

Assuming quasi stationarity to be valid for the entire northern part of the flight track, dropsonde and in situ measurements in the ABL can be compared as a function of distance traveled by the air mass over the ice between the measurement locations. Figure 7.24 shows the change in potential temperature multiplied by the depth of the ABL derived from the Richardson number criterion as a function of the time the advection took in downwind direction. The ABL is warming in downwind direction between the measurement locations,

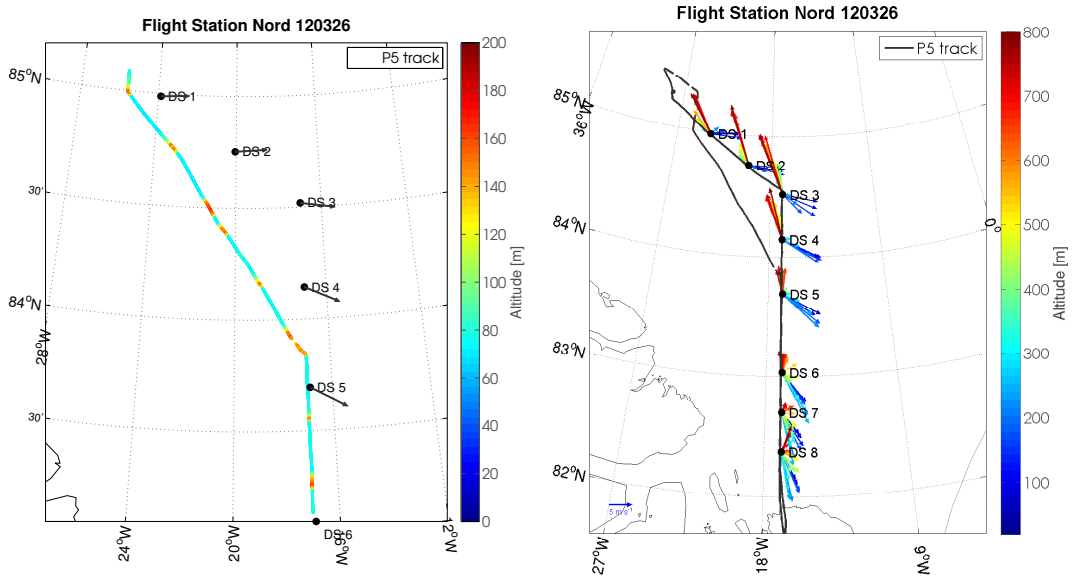

Figure 7.22: Flight track of the flight on 26 March 2012 over the Arctic Ocean to the north of Greenland. (left) Low-level flight leg with color coded flight altitude. The course of the low-level leg was changed to avoid flying through haze. The black arrows indicate the wind vectors at 50 m altitude, measured by the dropsondes on the returning high-level leg. (right) Wind vectors from the dropsondes launched on the high-level inbound leg with altitude color coded in 40 m intervals between the lowest dropsonde measurement and 800 m.

suggesting a net positive heat flux into the air mass. A likely origin for this heat flux are the open and partly refrozen leads occurring in the area between the two flight tracks. However other sources must be considered as well, especially entrainment at the top of the ABL, surface warming by radiative forcing from the clouds above 500 m. Another possible source is latent heat converted during fog formation within the ABL, which was observed by AMALi. Due to these influences an estimate of the heat flux would only partly be representative for the open leads in the region of the advection. However, the warming can be seen as a qualitative sign of the influence of open leads on the ABL.

7.3.3 AMALi and dropsondes flight leg

Figure 7.26 shows AMALi measurements from the inbound high altitude leg. The most prominent feature is a cloud system extending horizontally over more than 150 km and vertically between 500 and up to 1250 m. It consists of a thin stratus deck in the south, connecting to the higher cloud band in the north that was probably caused by lifting due to the front.

Southwards of the clouds a layer of homogeneously enhanced backscatter between the ground and 500 m altitude extends towards the coast. Its top shows a sharp gradient separating it from the background troposphere above. Partly below the cloud layer, between 14:05 and 14:23, an inhomogeneous layer with considerably higher backscatter values of β_{Aer} between 10 and $20 \cdot 10^{-6}$ $\mathrm{m^{-1}sr^{-1}}$ and a color ratio of $CR \approx 0.6$ is embedded in the first layer between shortly above the ground and about 250 m. The high color ratio and backscatter values indicate fog particles. Aerosol depolarization has values around 10 %. This value is relatively low for ice particles, but significantly higher than the depolarization

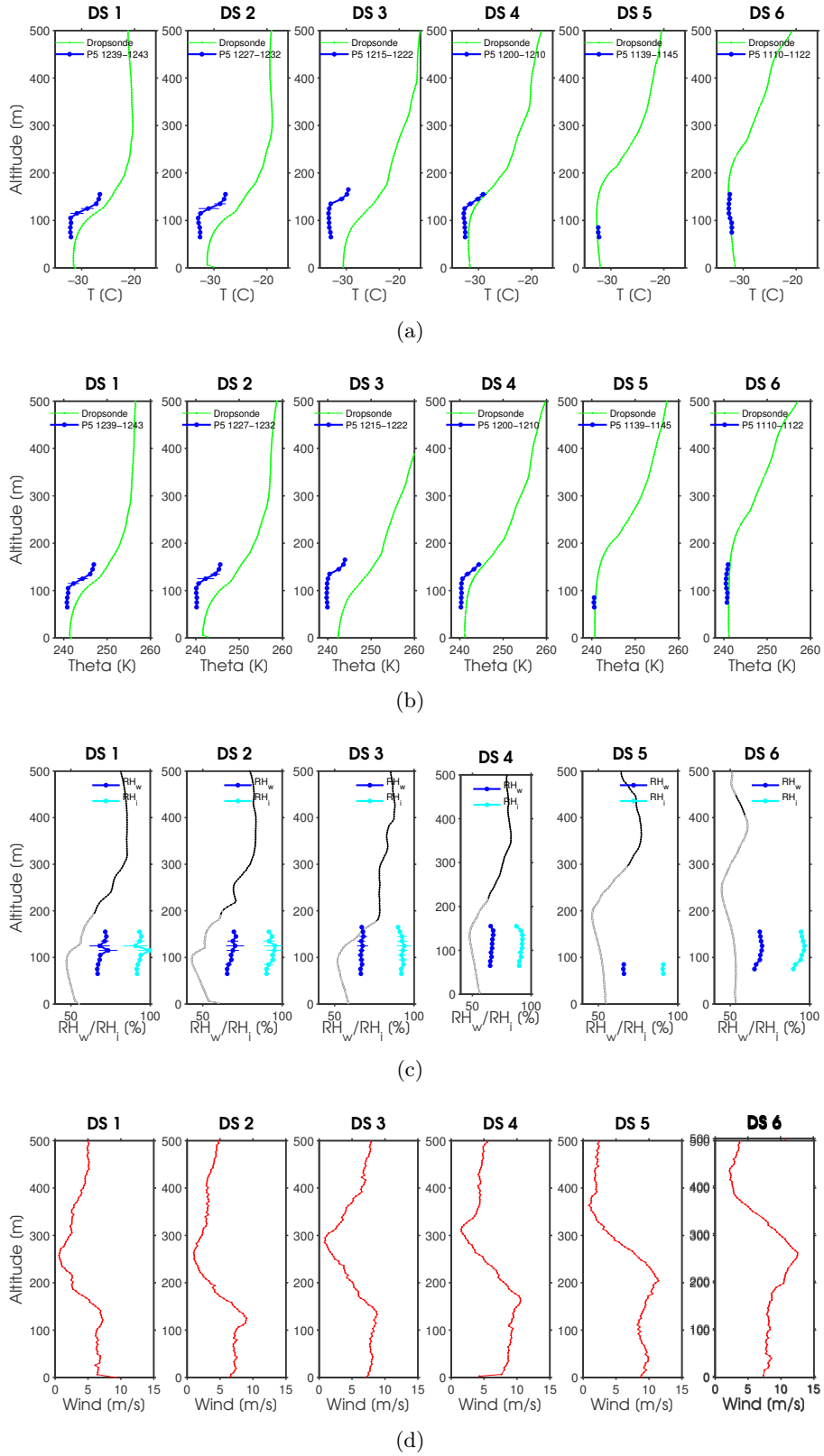

Figure 7.23: Dropsonde profiles from the flight on 26 April 2012 of dropsondes 1 to 5 together with Polar 5 in situ profiles obtained during the low level leg for matching directions of advection, showing a) temperature, b) potential temperature, c) relative humidity and d) wind speed.

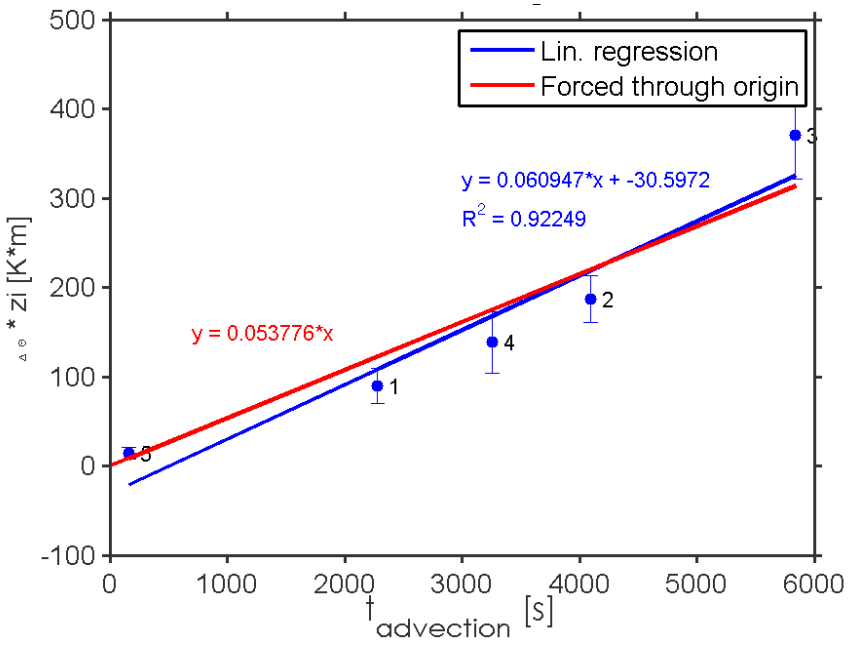

Figure 7.24: Difference in potential temperature between the 5 upwind and downwind profiles multiplied by the respective ABL height from the Richardson number criterion. Error bars denote the estimated error from ABL height.

found in the upper parts of the warmer cloud system above, which seems to consist predominantly of water droplets. The fog layer can thus be assumed to consist of ice particles having a moderately aspherical shape (Liu et al. 2004).

Between 14:10 and 14:20, AMALi shows additional structures of relatively large particles between the fog layer and the cloud layer. They have a significantly higher depolarization than the fog below, indicating a different origin of the particles and identifying them as weak ice precipitation falling from the cloud layer into the fog layer.

The red crosses in the plot mark boundary layer heights determined from six dropsondes using the ground related Richardson number criterion with $Ri_c = 0.22$. They show that the fog layer between 14:10 and 14:25 corresponds to the boundary layer where it occurs. At the same time the layer with weakly enhanced backscatter reaches almost twice as high as the ABL defined by the dropsondes. Although this layer appears to be homogeneous between 0 and 500 m, it is separated by an inversion. This layer seen by AMALi therefore does not represent the actual boundary layer, but can be considered as a residual layer that was advected. As ERA-Interim data from 6 to 12 hours earlier reveal (not shown), it is likely to originate from the marginal ice zone and has traveled over ice for approximately one day.

Due to the advection from west the air mass flowing into the region covered by the AMALi measurement until about 14:10 was probed in situ prior to the fog formation. Unfortunately the view of AMALi on the boundary layer was mostly blocked by the clouds in this region. However since the fog layer is seen by AMALi in all regions not attenuated by the clouds and it may be assumed that it extends horizontally below the cloud system. This is supported by the fact that the dropsonde profiles show a relatively continuous behavior for this region.

At the beginning of the AMALi measurement around 13:25, backscatter and color ratio are only weakly enhanced in the ABL. 10 minutes later, about 50 km further to the southeast, color ratio and backscatter are enhanced as they are from 14:10. The measurement

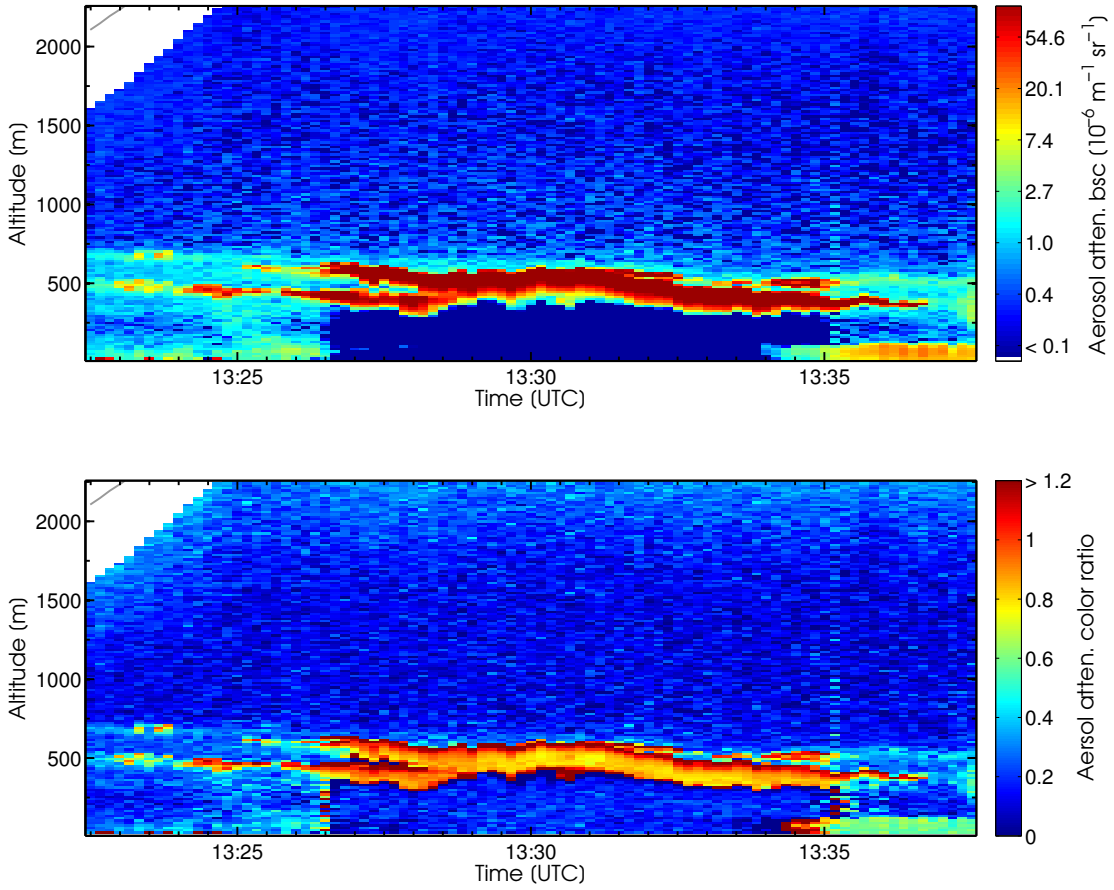

Figure 7.25: Part 1 of the AMALi measurement from 26 March 2012.

covers different stages of formation of a plume here.

7.3.4 In situ measurements

Two vertical profiles of size resolved aerosol number concentrations from 70 to 3000 m were measured at the beginning and at the end of the high altitude leg (Figure 7.28 a) and b)). Profile a) from the northern end shows likely cloud influenced aerosol up to about 700 m altitude. Small particle concentration $N_{<100}$ is reduced by more than a factor 4 compared to values in the troposphere above. $N_{>100}$ and $N_{>300}$ are both increased with two distinct peaks at 400 and 700 nm coincident with the two layers measured by AMALi directly after the ascent (figure 7.25). The AMALi measurement shows how these layers fade into clouds within a few kilometers, suggesting that the diameter increase in the in situ measurement originates from cloud processing of the aerosol. Towards the ground the concentrations show a further distinct peak between about 80 and 200 m and again a decrease below. The second profile b) that was measured during descent at the end of the high leg shows increased concentrations for large particles within the residual layer as well, but with less sharp gradients. Small particles show a strong peak between 100 and 400 m that may as well originate from a local source during the landing approach to Station Nord.

Figure 7.29 shows the time series of the in situ measurements over the duration of the flight. During the low level leg at the first part of the flight, the in situ aerosol measurements show relatively constant number concentrations for large particles $N_{>100}$ and $N_{>300}$. Small

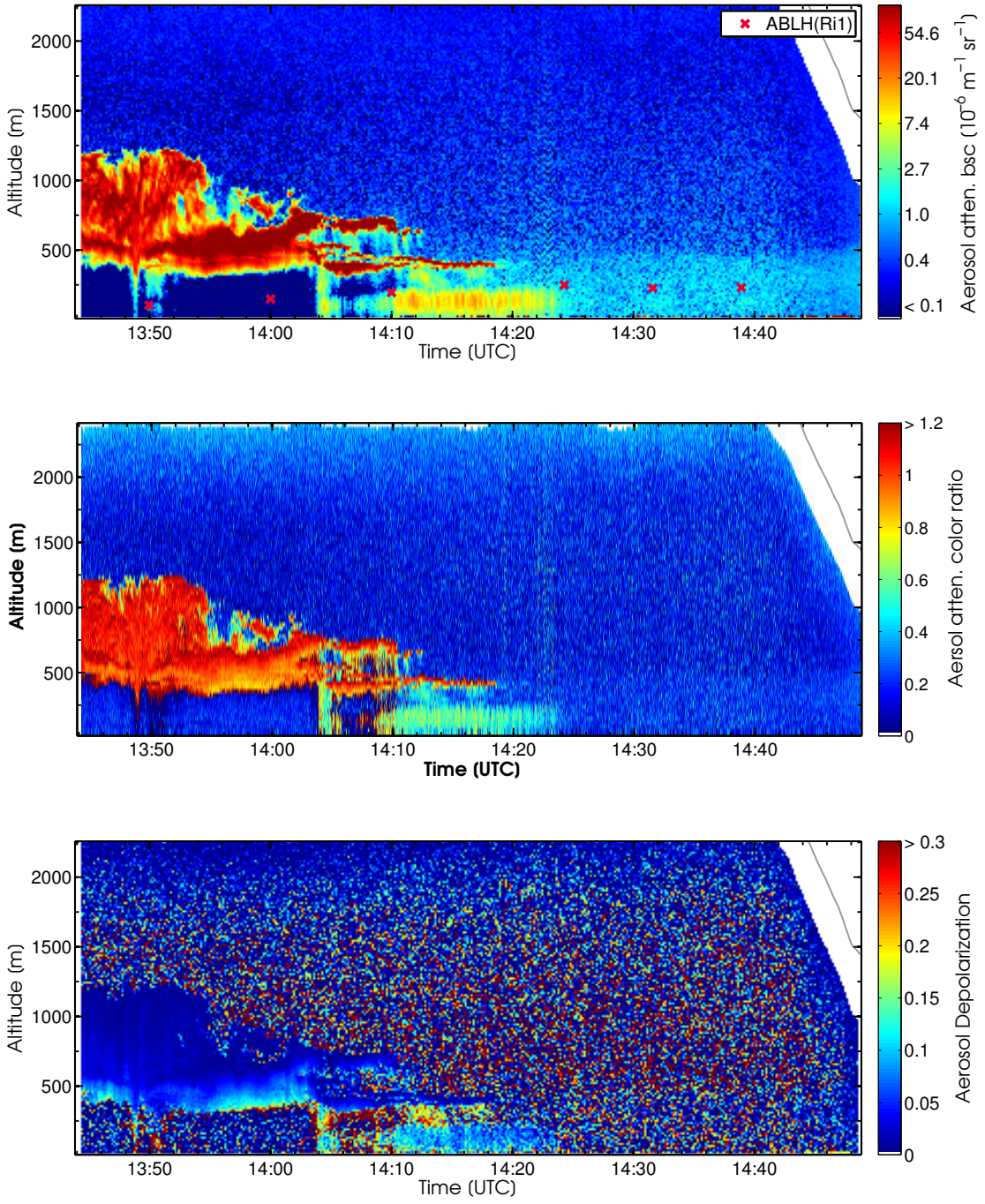

Figure 7.26: AMALi attenuated backscatter, color ratio and depolarization on the inbound flight leg over sea ice towards Station Nord. Red crosses indicate Richardson number ABL heights from dropsondes DS 3 to DS 8.

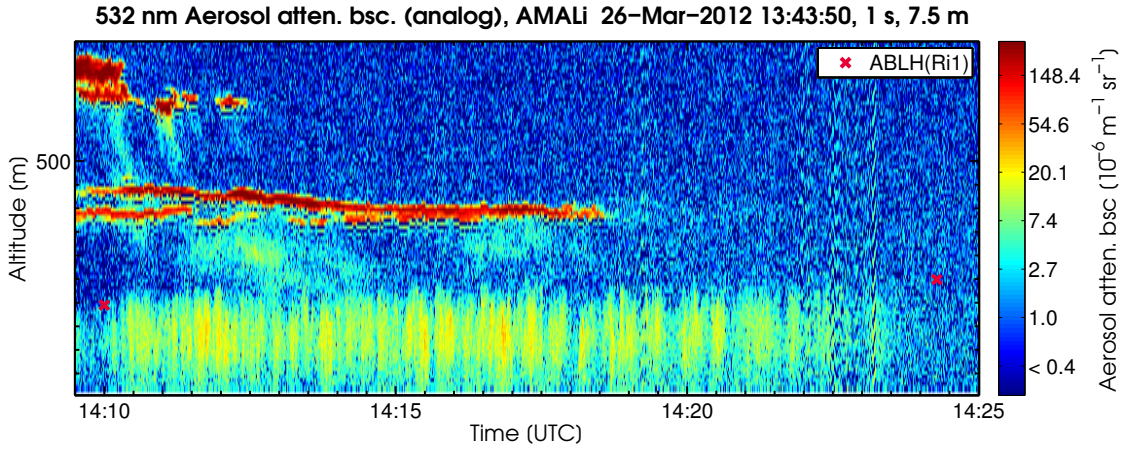

Figure 7.27: AMALi aerosol attenuated backscatter on March 26 2012 at 532 nm, zoomed in on the fog layer. The color scale was adjusted here. Red crosses indicate Richardson number ABL heights from dropsondes DS 5 and 6.

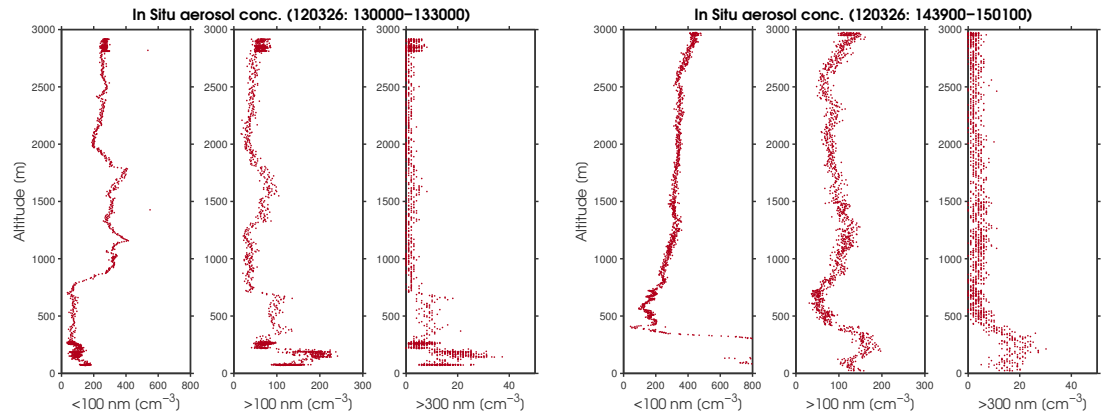

Figure 7.28: Vertical profiles of aerosol number concentrations measured in situ by UHSAS and CPC, separated into three different particle diameter ranges. a) Ascent profile before lidar measurement, b) descent profile after lidar measurement

particles exhibit more variations with a particularly strong decrease of almost 50 % around 12:10. At all size ranges, concentrations show strong variations with altitude during the short bird calibration ascents (altitude is shown in the bottom plot). While small particles decrease with altitude, particle numbers for $D_p > 100$ nm increase at the same time. This was not observed during the first part of the flight, where the ABL height was not reached by the short ascents, but starts from 11:45 on, where ABL heights were lower. The profiles therefore show the difference of aerosol properties within and above the ABL. Figure 7.30 compares profiles from the first and the second part of the leg between 70 and 170 m altitude. The decrease of small particles and increase of large particles, respectively, are very clear above about 130 m.

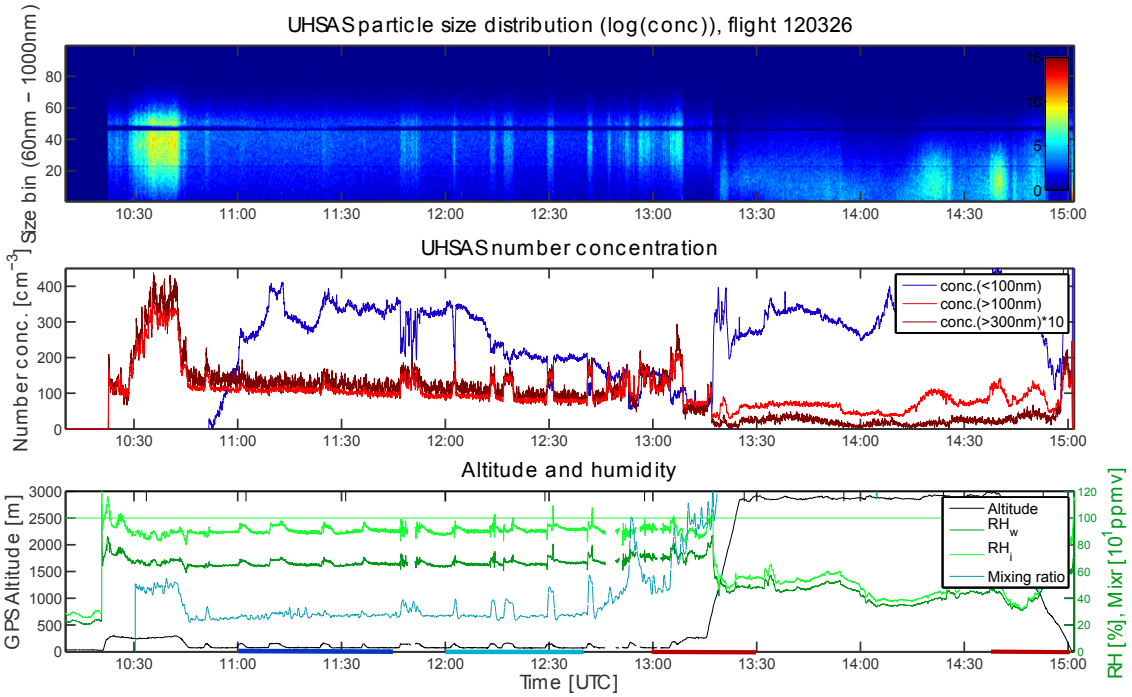

Figure 7.29: In situ aerosol measurements during the flight on 26 March 2012. (Top) Particle number concentration measured by the UHSAS particle spectrometer on a logarithmic color scale. The X axis shows size bins of the instrument with logarithmic spacing between 60 and 1000 nm. (Middle) UHSAS number concentrations divided in size ranges. (Bottom) GPS altitude of Polar 5, relative humidities from the humicap sensor and water vapor mixing ratio from the CR2 dewpoint mirror. Colored bars at the bottom indicate the time intervals of the vertical profiles

7.3.5 Interpretation

The most likely origin for the fog layer measured by AMALi in the ABL is humidity emitted from the leads in the advection path. Figure 7.31 shows a schematic of the proposed formation mechanism. (Burk et al. 1997) investigated the formation of plume layers downwind of open leads under different atmospheric conditions using a 2 dimensional steady state boundary layer model. They ran simulations for which they varied different parameters, such as the temperature difference between surface and air, the lead width and the atmospheric lapse rate. They found a particularly strong influence of stratification on the

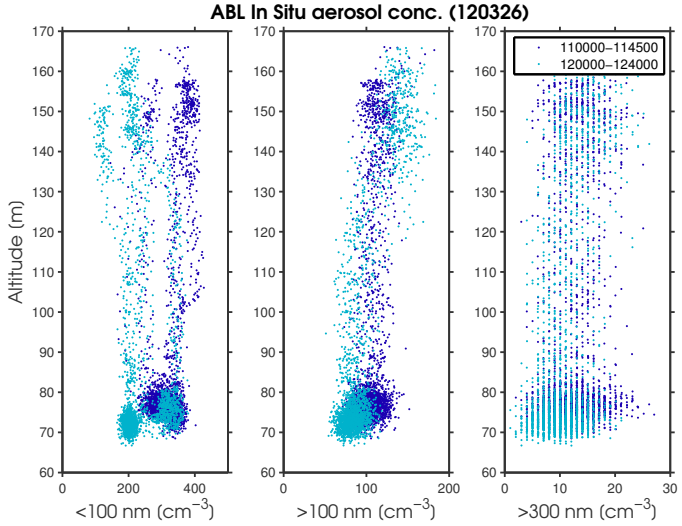

Figure 7.30: Vertical in situ aerosol profiles as in 7.28 for low-level vertical profiles during the low level flight leg. The colors denote two different time intervals, showing the evolution of the aerosol concentrations in the boundary layer over the flight leg.

atmospheric response to open leads. While so called steam fog directly above the leads forms almost regardless of the relative humidity of the incoming air if the air-surface temperature difference is high enough, the formation of an extended plume downwind of the leads required the stability within the ABL to be low in their simulations. They show that only if the air is able to rise sufficiently, water and ice particles form downstream of the lead above a certain altitude, creating an elevated plume below the capping inversion, which was at about 200 m in one of their cases.

At air temperatures below −30 °C together with a near-neutral stratification the conditions for the formation of an extended plume containing ice particles are given here (Burk et al. 1997).

Where the plume is visible after 14:05, it shows a noticeable pattern with intermittent areas of high and low backscatter in the horizontal. This indicates a cell-like structure of the plume. A possible explanation for this may be the formation of convective roll vortices downstream of the leads (figure 7.27). The horizontal scale of the cells seen by AMAli varies between about 1 and 2 km. Assuming vortices that are approximately parallel to the wind direction yields a mean $d = x \cdot \cos(\alpha) \approx 1.2$ km and therefore an aspect ratio of $z_i : d = 1 : 5.5$. This is a relatively high horizontal dimension compared to typical values of $1 : 3$ given by (Stull 1988), which may be a result of horizontal divergence and at the same time vertical confinement of the rolls by the capping inversion.

7.4 Gravity waves at ABL top (7 April 2012)

On 7 April 2012, gravity waves occurring at an inversion above sea ice between islands near Resolute Bay, Canada were observed. An additional plume of thin ice fog, probably originating from small polynyas in the upwind region had formed within the ABL. Dynamic behavior of the waves, cloud properties changing under their influence and the thin ice fog are three partly independent features that can be characterized from this flight. The flight consisted of a northward high level leg over ice between the islands and a low level leg partly

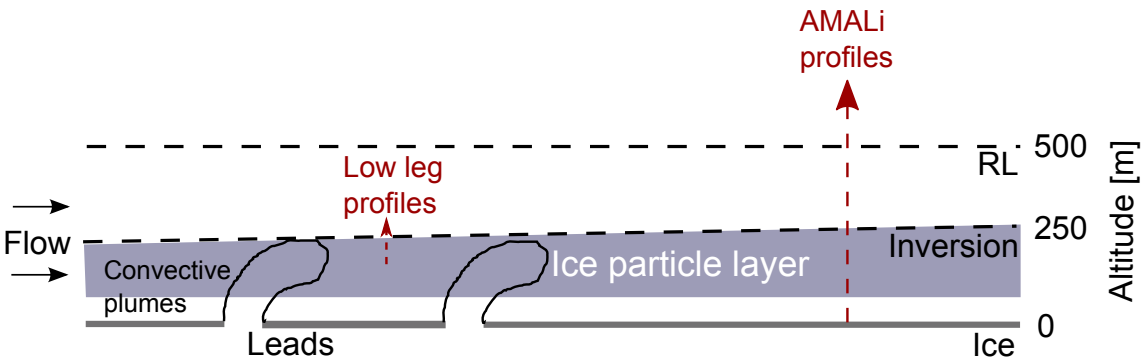

Figure 7.31: Proposed mechanism for the formation of the ice haze layer on 26 March 2012 that is embedded within the residual layer. The orientation is with the air flow from nort-west. RL marks the top of the residual layer.

back on the same track. The low level leg then left the original track to sample several specific spots with the EM-bird. Dropsondes were not deployed on the flight, since it was originally intended to focus on sea ice observations. However temperature and relative humidity along the track are available from aircraft in-situ sensors. Due to the limited information available for the interpretation of the flight, this case will be discussed relatively briefly. Nevertheless it is interesting due to the variety of features that can be derived from the AMALi measurement.

7.4.1 Meteorological and sea ice situation

Figure 7.32 (left) shows geopotential and wind at 850 hPa and pressure at mean sea level from ERA-Interim data at 12 UTC, 3 hours before the flight. Wind was blowing steadily from north, north-west, driven by a high pressure system over the Beaufort sea and a low over the western part of Greenland. The observed air masses close to the surface were advected from the central Arctic Ocean before they reached the first islands (1000 hPa map, figure 7.32 (right)). Sea ice between the islands had a mostly closed surface with few small polynyas occurring in the vicinity of nearby islands. Several single small leads were observed visually close to the northern end of the flight track. Since no dropsonde measurements are available from the flight, the only information about wind speed and direction is from ERA data and a radiosonde started at 12 UTC from Resolute Bay, located at the southern end of the flight track (not shown). It confirms the wind direction indicated by the ERA data and shows wind speeds between 7 and 8 m/s up to the top of the ABL. This wind speed may differ from the one that was present at the location and time of the flight leg due to orographic influence near Resolute Bay. However it provides an estimate of the conditions.

7.4.2 Formation of gravity waves

The backscatter measurement of AMALi at 355 nm (figure 7.35) shows two main features. The first one is a thin cloud layer at about 300 m altitude that exhibits a wave structure (top and bottom). The second one is a thin fog layer in the right, i.e. the northern part of the top image. It extends from the surface to about 150 m altitude. Aerosol depolarization with values up to 15 % (middle) indicates that it contains ice particles.

The cloud layer is located at the top of a stably stratified layer as can be seen from the potential temperature profile shown in figure 7.33 (blue), that was measured during the descent at the northern end of the high level AMALi flight leg. The potential temperature

shows the stratification of the stable layer as it was advected by the mean flow from the Arctic ocean. The actual ABL only extended up to an altitude of about 120 m and was stably stratified as well. It agrees with the ice particle layer measured by AMALi, that may have originated from the open leads to the north. The second profile shown in the plot (cyan) was measured during a short ascent during the low level leg further to the south, where the ice particle layer was not present. It covers only a lower altitude range. The potential temperature shows a warming of the ABL by about 4.5 °C and a change of stratification from stable to near neutral.

A small island was located on the flight track. It can be seen in the AMALi image at 15:43 as an elevation shown in red, where the lidar signal was reflected from the ground. The island had a height of approximately 80 m. It marks the transition of the ABL from the stable conditions of the northern profile to the near neutral conditions of the southern profile. This transition was apparently at least partly caused by turbulence created in the flow around the island. Additional warming of the ABL may have occurred by heating of the surface due to downward long wave radiation from the cloud layer at 300 m. It may be assumed that the warming reduced the stability of the ABL and the turbulent disturbance caused a mixing with the air layer above. This is supported by the irregular structures that occur in the backscatter plot between 15:35 and 15:40 up to the cloud layer.

The wave motions of the cloud layer, as well as the cloud layer itself, start downstream of the island and match the location of the island with their period. Apparently the island caused the excitation of the gravity waves here. The waves have an amplitude of $\Delta z \approx$ 60 to 100 m and a wavelength $\lambda \approx 2$ to 3.5 km. As can be seen from some small deflected cloud and aerosol features near 15:25, they extend vertically up to an altitude of at least 800 m. The gradient of potential temperature associated with the bottom and the top of the inversion layer at 200 and 320 m, respectively, can be estimated to 7.5 K/100m. From this, the Brunt-Väisälä frequency at the layer is calculated as

$$N = \sqrt{\frac{g}{\Theta}\frac{\partial\theta}{\partial z}} = 0.0029s^{-1}, \tag{7.1}$$

with g the gravity acceleration. Assuming the waves to be stationary, $1/N$ multiplied by the wind speed of 7 to 8 m/s yields a wavelength in the range from 2.4 to 2.7 km which is in good agreement with the observations.

The cloud layer that is deflected by the gravity waves shows a variation in optical thickness between regions of wave crests and troughs. It can be clearly seen from the attenuation of the lidar signal below the clouds (figure 7.35 (bottom). This variation can be explained by increasing and decreasing liquid water content due to the adiabatic motions of air parcels within the waves. At around 15:40 in plot 7.35 (middle), structures in the aerosol depolarization are visible that extend from the cloud layer to the surface and indicate ice precipitation. The precipitation occurs in spatially confined streaks of the approximate scale of the wavelength. Thus it may be hypothesized that they are related to the adiabatic lifting process at the wave crests. Micro-physical studies of such clouds under the influence of gravity waves may be interesting as they would allow to study changes of clouds and aerosol particles therein under the influence of repeated condensation and evaporation cycles.

This case is interesting in the context of Arctic ABLs, because it illustrates a process that is capable of extending the influence of the surface beyond the top of the ABL. Zilitinkevich (2002) found the interaction of gravity waves and turbulence to be an important mechanism in the stable ABL, allowing originally local turbulence to affect the flow at higher altitudes by transporting its momentum. Unfortunately no wind or turbulence measurements are

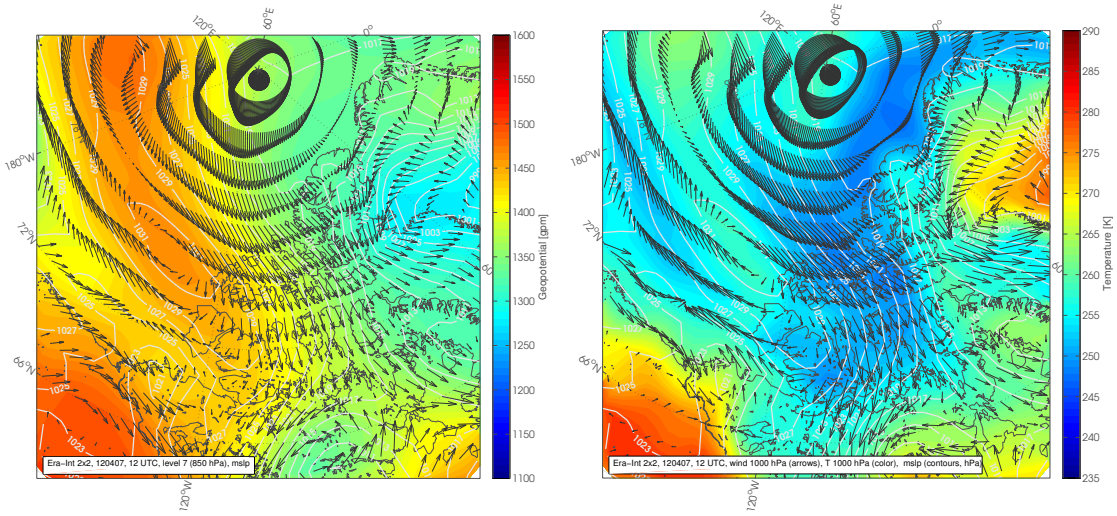

Figure 7.32: (left) ERA-interim geopotential and wind at 850 hPa and mean sea level pressure (white lines), showing the meteorological situation on 07 April 2012 over the Canadian Arctic. (right) Temperature and wind at the 1000 hPa level with mean sea level pressure. Note that 1000 hPa data in over land masses may not be valid due to surface elevation.

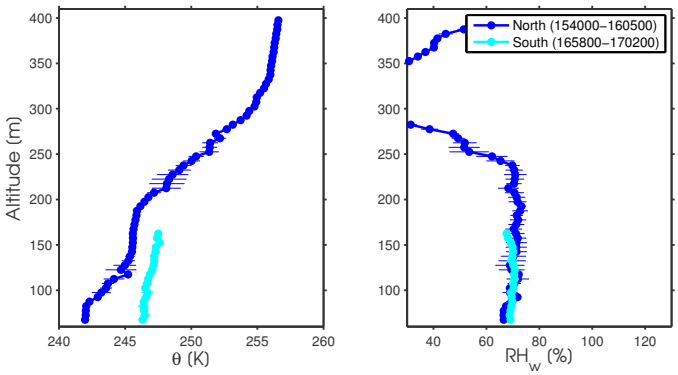

Figure 7.33: Vertical profiles situ measurements within and above the ABL for two time intervals during the low level leg of the flight on 07 April 2012.

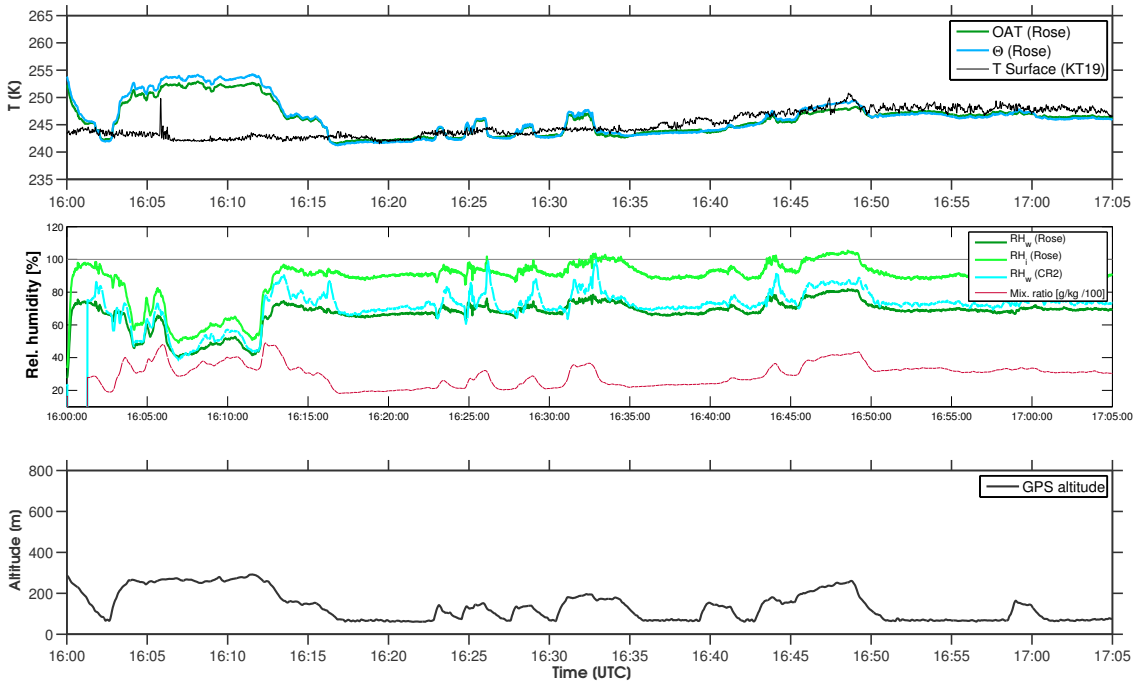

Figure 7.34: In situ measurements of air temperatures, humidities and surface temperature during the low level leg of the flight on 07 April 2012.

available from this flight. Nevertheless the AMALi measurement allows an insight into the vertical distribution of the waves. As the gravity waves break at different altitudes, they cause a vertical exchange of momentum and therefore increase the dynamic coupling between ABL and free troposphere.

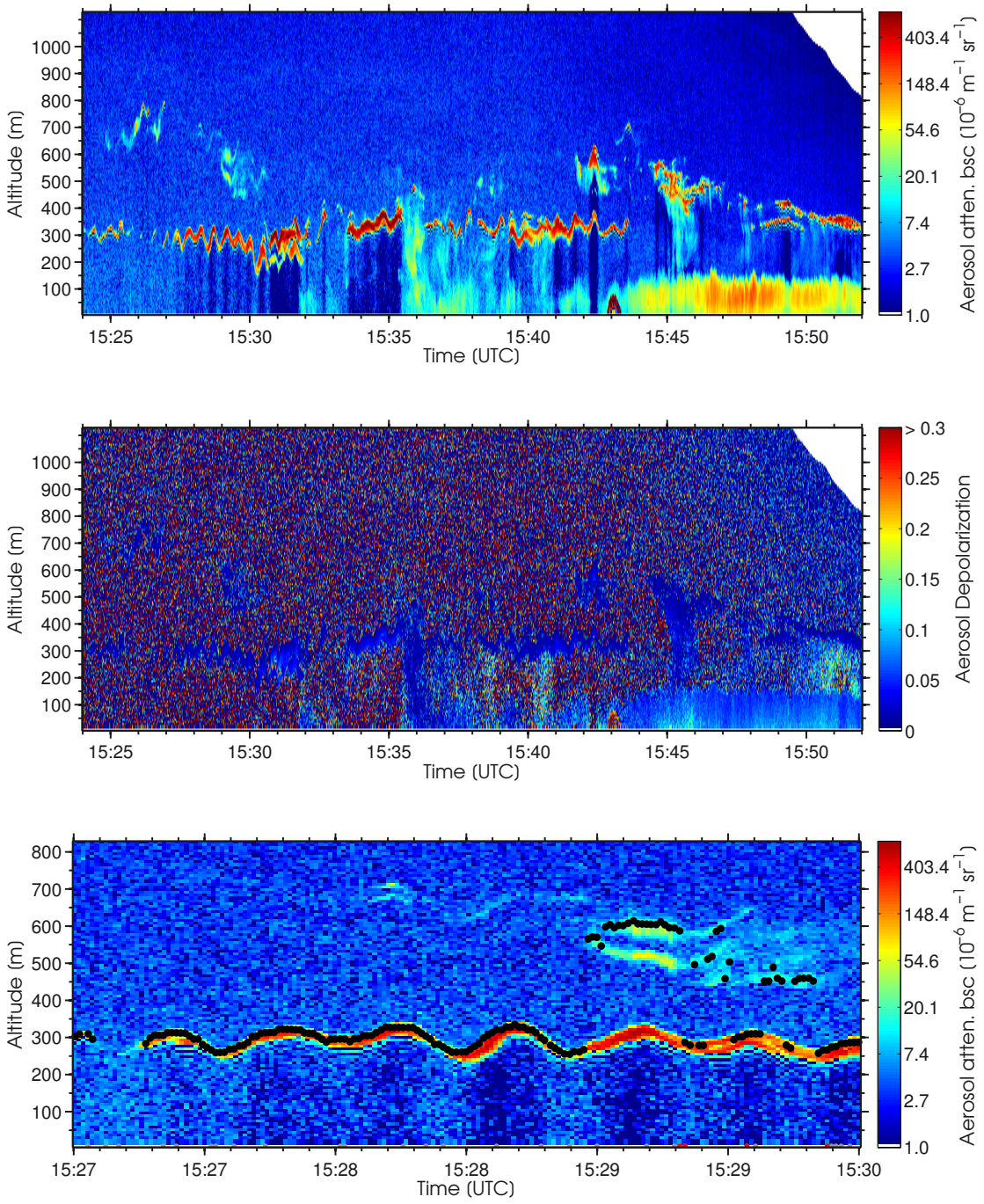

Figure 7.35: AMALi measurement from the flight on 7 April 2012, showing gravity waves at the top of a stably stratified ABL close to Resolute Bay. (top) Aerosol attenuated backscatter at 355 nm, (middle) aerosol depolarization at 532 nm. (bottom) Zoom into the top figure between 15:27 and 15:30, with black dots marking the cloud tops. Note the attenuation of the backscatter signal below the cloud that varies with the cloud top altitude.

7.5 Summarizing discussion of the case studies

Four exemplary snapshots of processes in the lower troposphere and atmospheric boundary layer over the Arctic ocean during spring time were evaluated and discussed. They represent typical conditions as they occur under the influence of varying sea ice concentrations and larger scale atmospheric conditions.

The case studies can be categorized in a short form in terms of the basic characteristics of the original ABL, the process modifying the ABL and the resulting ABL:

24 March
: Off-ice flow from a stable Arctic ABL was modified by leads and open water, resulting in a strongly convective ABL.

22 April
: An air mass advected from a land mass was modified by a polynya and open leads, resulting in a moderately convective and humidified ABL.

26 March
: A residual layer of a former on-ice air flow was modified by a front, clouds and open leads, resulting in a convective ABL with fog formation, embedded in the former residual layer.

07 April
: Air that was advected from the central Arctic ocean experienced gravity wave formation at a strong ABL top inversion resulting in upward propagation of waves and the modification of clouds at ABL top.

The case of **24 March** shows the transition from an ABL that is stably stratified and has low aerosol concentration and humidity towards a regime with strong, organized convection and cloud formation. The transition occurs entirely due to the influence of the horizontally changing sea ice surface over which the air is advected. A gradually increasing open water fraction first leads to a reduction of stability, an increase of turbulence and entrainment of aerosol from the free troposphere. During the process a shallow internal ABL forms in which fog occurs over leads. This fog layer is confined to a region determined by the supply of moisture from open leads on the one hand and the dissolving due to mixing and dilution with dry air on the other hand. Where air from the ABL is finally advected over open water, the strong supply with sensible and latent heat due to the large temperature difference causes a rapid development of convective clouds. They increase the height of the ABL top from about 100 m to more than 1500 m. In the process of the height increase an advected aerosol layer is partly entrained into the ABL and can be expected to be mixed down to the surface and to be partly removed from the atmosphere by wet deposition.

The case of **22 April** shows a partly convective ABL that has formed within an advected air mass under the influence of an open polynya. Due to a relatively high concentration of partly open leads the ABL is maintained in a state of near neutral stratification and moderate convection. Moisture that is emitted into the ABL from the water surface of the polynya and the leads, causes hygroscopic particle growth and therefore an increase of aerosol backscatter. A spatially confined plume of increased aerosol backscatter is advected downstream of a lead that has presumably caused it and thereby extends almost up to the top of the ABL.

The setting for the case of **26 March** is a residual layer resulting from an earlier on-ice air flow from the open ocean, probably mixed with an air mass originating from the

Greenland ice shield. The layer is characterized by enhanced aerosol backscatter relative to the free troposphere. Within the residual layer a cooler, originally stable ABL has formed due to cooling from the ice surface while the warm air was advected over the ice. It extends up to about half the height of the residual layer. This ABL becomes part of a shallow front between warm air masses that flow northwards from the ocean and cold air within the ABL flowing in the almost opposite direction. Sporadic leads cause convection within the very cold ABL, presumably acting together with clouds above, that cause longwave radiative warming of the surface. Within the ABL a fog layer occurs that shows structures of organized convection and contains ice particles. Further complexity is added to the scenario by ice crystals precipitating into the fog ABL from the higher cloud layer.

The case of **07 April** is slightly different from the other cases. It shows the formation of gravity waves at the strong capping inversion of a moderately stable ABL. They appear to be excited by the less than 100 m high orography of a small island. A layer of optically thin ice fog that is originally embedded within the ABL is mixed with the air above where turbulence is generated within the moderately stable ABL at low levels by the island. The gravity waves at the inversion layer displace a thin cloud layer vertically. Thereby they cause periodic adiabatic cooling and warming of this layer that leads to increasing and decreasing liquid water content of the clouds. This process may cause sporadic ice precipitation of the cloud layer. The waves propagate vertically into the troposphere as internal gravity waves and thereby exchange momentum up to at least 800 m. This is far higher than the height to which turbulence usually reaches that originates from the ground and is trapped within the ABL by the capping inversion.

The presented case studies illustrate the complexity and diversity of Arctic boundary layer processes. They show in which ways the presence of open water can have a large effect that often dominates the character of the ABL. Even low concentrations of open leads modify the ABL in terms of stability, height, entrainment, aerosol properties and concentrations as well as the formation of fog plumes and clouds. The underlying processes depend to a large extent on the initial properties of the advected ABL. Near neutral stratification as it occurs in a residual layer facilitates convective mixing up to altitudes of several hundred meters. In contrast, an initially stable ABL limits the height up to which mixing occurs. The stability is gradually reduced in the process as the upward turbulent heat flux heats the ABL, leading to entrainment at its top. Fog layers were observed preferably when the temperature of the advected ABL was relatively cold, with temperatures below $-25°$ in the cases analyzed here.

The case studies illustrate the difficulties of ABL height determination over Arctic sea ice, especially from backscatter lidar measurements. For the first case, an estimate of ABL height from backscatter is only possible due to the presence of clouds and fog within the ABL. However the thin cloud layers that are detected during the first part of the flight apparently only provide an upper bound for the ABL height when compared to the dropsonde criteria. Due to aerosol concentrations decreasing towards the ground, an ABL height can hardly be determined unambiguously from aerosol alone here. The second case is one of the few of the campaign that seem to allow an unambiguous ABL or mixing layer height detection. This is due to a significant aerosol and moisture source at the surface from open water. The source of the backscatter enhancement is at the same time the mechanism that underlies the ABL formation here. For the third case, classical lidar ABL height criteria would have detected the residual layer as ABL, yielding an error of about +100 %. Only due to the adjustment of gradient and wavelet transform detection thresholds to high sensitivity, the much more subtle gradient separating the ABL from the residual layer could be detected. This comes at the cost of a high sensitivity to noise or

insignificant fluctuations of backscatter.

This shows that determining the height of the ABL often requires a combination of different methods, as applied in this study. Especially stable boundary layers over sea ice are challenging to detect. However where open water surfaces influence the ABL, it reaches higher heights and is at the same time more easily detected and characterized.

8 Conclusion and outlook

In this study, aircraft measurements of the lower troposphere influenced by the underlying sea ice surface were analyzed, covering a large part of the western Arctic Ocean from Svalbard to Canada. The measurements were performed in 2012 as part of the aircraft campaign PAMARCMIP of the Alfred Wegener Institute for Polar and Marine Research. Data from a variety of different instruments on board the aircraft Polar 5 were combined to understand and interpret processes related to the influence of open water on the atmospheric boundary layer (ABL). These direct influences range from the exchange of sensible and latent heat over the emission of aerosol particles to the modification of the dynamic properties of the ABL. Indirect influences can reach much further. The strongest one is certainly the formation and modification of clouds by adding moisture and aerosol serving as condensation and ice nuclei, since any change in cloud cover has a considerable effect on radiative transfer within the atmosphere. It could be shown how even small concentrations of open and partly refrozen leads can create fog layers within the ABL, consisting of either water or ice particles.

The combination of the nadir pointing lidar AMALi and dropsondes allows a comprehensive examination of the lower troposphere and the ABL down to the surface. Besides the measurement of optical properties of aerosols and clouds, the lidar measurements provide useful information about the structure of the atmosphere. This aspect of the measurements was applied in this study to assess the height of the ABL from vertical gradients of aerosol backscatter. The heights derived from gradients in the backscatter profiles were compared using different criteria based on dropsonde measurements of temperature and wind and were found to provide a valid estimate of the ABL height in many cases.

The agreement between the methods depends on the characteristics of the respective ABL. Under stable conditions over sea ice the criteria can deviate considerably from each other. This is partly due to the fact that the height of the ABL is not always well defined. The lidar backscatter criteria rely on aerosol as a tracer which is not always associated to the ABL over sea ice, as opposed to mid-latitude conditions. Nevertheless the overall agreement between the methods is surprisingly high. Especially under convective conditions, both dropsonde and backscatter criteria prove to be reliable. The closest agreement between backscatter and dropsonde criteria taking into account all examined profiles is found between a backscatter gradient and a surface bulk Richardson number criterion. A discontinuity in the temperature profile provides a reliable upper bound for the height of the ABL.

Four case studies were chosen and analyzed in detail to illustrate processes in the ABL that depend on the underlying sea ice concentration and represent typical conditions over the Arctic Ocean during springtime. They show the large influence that open water and leads have on the characteristics of the ABL by modifying its structure and height while forming cloud and fog layers. In general the occurrence of open water tends to destabilize the ABL and to increase its height, acting in favor of entrainment of air and aerosol from the free troposphere.

By entrainment and subsequent wet scavenging, the ABL can act as a sink for aerosol from the free troposphere. This could play a role in the removal of Arctic haze from the atmosphere and the transition from high aerosol concentrations during springtime to low

concentrations during summertime that is a known phenomenon in the Arctic (e.g. Tunved et al. 2013). An increase of lead concentration, starting earlier in the year in response to a warming climate, might reduce the lifetime of Arctic haze in the atmosphere. In the case of absorbing aerosol particles, their deposition on snow reduces the surface albedo and therefore has the potential to increase sea ice melt (e.g. Hansen and Nazarenko 2004). This might represent a positive feedback mechanism, acting in favor of further lead formation in the vicinity of already existing leads.

The chosen measurement patterns have proven to be very useful to examine the lower troposphere and the ABL by means of lidar and in situ measurements. Some recommendations for future campaigns addressing the subject to yield best possible results can be given.

The turbulence measurements conducted during the campaign provided valuable qualitative information about the actual state of the ABL. They allow to identify turbulence and are therefore very useful to validate other criteria for estimating ABL height. Performing additional flux measurements would bring the advantage of more comprehensively quantifying the state of the ABL. But obtaining reliable quantitative measurements of wind vectors with the existing AIMMS-20 instrument would already be of great value for the characterization and interpretation of the conditions found during flights. Investing efforts into an improved calibration of the instrument would therefore be worthwhile.

The interpretation of most measurements relies on additional quantities measured by other instruments. This is particularly important during airborne campaigns, where results are not derived from long time series, but are based on a snapshot of a condition or a process that has therefore to be characterized as comprehensively as possible. The most essential variables are the meteorological ones, temperature, humidity, pressure and wind vector. They are available for Polar 5 campaigns in a powerful and comfortable to use database system, however at present only in a raw version as recorded by the instruments. This ensures that the original data are preserved in a transparent way. Nevertheless it would be beneficial to add an evaluated version of these essential data on a routine base, including the most recent calibration.

In-situ measurements from the short ascending profiles during low level legs that are originally conducted for calibrating the EM-bird contain valuable information about the ABL in many cases. Aerosol as well as meteorological measurements from these profiles were used for analyses in this study, but did not always reach the ABL, depending on its respective height. For future campaigns, flight planning could include repeated short profiles covering the ABL down to the lowest possible flight level to allow the in situ probing of shallow stable ABLs. This is not possible during the operation of the EM-bird, but could be considered at the beginning and end of each low-level leg, causing almost no additional effort.

A method for the AMALi lidar to measure absolute values of backscatter would increase the information content of the measurements and facilitate the evaluation. This could be achieved by including a reference measurement to circumvent the challenge of defining a boundary condition for the backscatter ratio in the free troposphere. Therefor a defined fraction of the emitted laser beam could be fed into the receiving unit for a short time interval every few minutes. This would allow the determination of the instrumental constants C_0 for the different channels to yield an absolute calibration of the lidar signals.

List of acronyms

ABL Atmospheric Boundary Layer

AIMMS-20 Aircraft-Integrated Meteorological Measurement System

AMALi Airborne Mobile Aerosol Lidar

AVAPS Airborne Vertical Atmospheric Profiling System

AWI Alfred Wegener Institute for Polar and Marine Research

BSR Backscatter ratio

CCN Cloud condensation nucleus

CPC Condensation Particle Counter

CR Color ratio

DMS Dimethyl sulfide

DS Dropsonde

ECMWF European Centre for Medium-Range Weather Forecasts

ERA-Interim ECMWF Interim Reanalysis

FFT Fast Fourier transform

GDAS Global Data Assimilation System

GPS Global Positioning System

HYSPLIT Hybrid Single Particle Lagrangian Integrated Trajectory Model

IBL Internal boundary layer

IPCC Intergovernmental Panel on Climate Change

KARL Koldewey Aerosol Raman Lidar

LCL Lifting condensation level

LIDAR Light detection and ranging

LLJ Low-level jet

LR Lidar ratio

MIZ Marginal ice zone

MODIS Moderate-resolution Imaging Spectroradiometer

Nd:YAG Neodymium-doped yttrium aluminium garnet

NISE Near Real-Time Global Ice and Snow Extent

OAT Outside air temperature

OPAC Optical Properties of Aerosols and Clouds

PAMARCMIP Polar Arctic Measurements and Arctic Regional Climate Model Simulation Project

PMT Photo multiplier tube

RADAR Radio Detection and Ranging

RH Relative humidity

SNR Signal-to-noise ratio

SSM/I Special Sensor Microwave Imager

TAS True airspeed

TAT Total air temperature

UHSAS Ultra High Sensitivity Aerosol Spectrometer

VERDI Vertical Distribution of Ice in Arctic Clouds

Bibliography

G. Ancellet, J. Pelon, Y. Blanchard, B. Quennehen, A. Bazureau, K. S. Law, and A. Schwarzenboeck. Transport of aerosol to the arctic: analysis of caliop and french aircraft data during the spring 2008 polarcat campaign. *Atmospheric Chemistry and Physics*, 14(16):8235–8254, 2014.

T. L. Anderson and J. A. Ogren. Determining aerosol radiative properties using the tsi 3563 integrating nephelometer. *Aerosol Science and Technology*, 29(1):57–69, 1998.

P. Berrisford, D. Dee, K. Fielding, M. Fuentes, P. Kallberg, S. Kobayashi, and S. Uppala. The era-interim archive. Technical report, ECMWF, Shinfield Park, Reading, August 2009.

K. M. Beswick, M. W. Gallagher, A. R. Webb, E. G. Norton, and F. Perry. Application of the aventech AIMMS20AQ airborne probe for turbulence measurements during the convective storm initiation project. *Atmospheric Chemistry and Physics*, 8(17):5449–5463, 2008.

L. Bi, P. Yang, G. W. Kattawar, B. A. Baum, Y. X. Hu, D. M. Winker, R. S. Brock, and J. Q. Lu. Simulation of the color ratio associated with the backscattering of radiation by ice particles at the wavelengths of 0.532 and 1.064 μm. *Journal of Geophysical Research: Atmospheres*, 114(D4), 2009. ISSN 2156-2202.

A. K. Blackadar. Boundary layer wind maxima and their significance for the growth of nocturnal inversions. *Bull. Amer. Meteor. Soc.*, 38:282 – 290, 1957.

R. Boers, J. D. Spinhirne, and W. D. Hart. Lidar observations of the fine-scale variability of marine stratocumulus clouds. *J. Appl. Meteor.*, 27:797 – 810, 1988.

C. F. Bohren and D. Huffman. *Absorption and scattering of light by small particles*. Wiley science paperback series. Wiley, 1983. ISBN 9780471293408.

A. Boronikov, L. Gaivoronskii, E. Zak, V. Kostarev, I. Mazin, M. Minervin, A. Khrgian, and S. S.M. *Cloud Physics, Israel Program for Scientific Translations, Jerusalem: Reference from Seinfeld and Pandis, 2006*, 1963.

I. M. Brooks. Finding boundary layer top: Application of a wavelet covariance transform to lidar backscatter profiles. *Journal of Atmospheric and Oceanic Technology*, 2003.

Buck Research Instruments, L.L.C. Model cr-2 hygrometer. *Operating Manual*, 2009.

S. D. Burk, R. W. Fett, and R. E. Englebretson. Numerical simulation of cloud plumes emanating from Arctic leads. *Journal of Geophysical Research - Atmospheres*, 102 (D14):16529–16544, JUL 27 1997. ISSN 2169-897X.

Y. Cai, D. C. Montague, W. Mooiweer-Bryan, and T. Deshler. Performance characteristics of the ultra high sensitivity aerosol spectrometer for particles between 55 and 800nm: Laboratory and field studies. *Journal of Aerosol Science*, 39(9):759–769, 2008.

D. J. Cavalieri, J. Crawford, M. Drinkwater, W. J. Emery, D. T. Eppler, L. D. Farmer, M. Goodberlet, R. Jentz, A. Milman, C. Morris, R. Onstott, A. Schweiger, R. Shuchman, K. Steffen, C. T. Swift, C. Wackerman, and R. L. Weaver. NASA Sea Ice Validation Program for the DMSP SSM/I: Final Report. NASA Technical Memorandum 104559. *National Aeronautics and Space Administration, Washington, D. C.*, 1992.

S. A. Cohn and W. M. Angevine. Boundary layer height and entrainment zone thickness measured by lidars and wind-profiling radars. *J. Appl. Meteor.*, 39:1233 – 1247, 2000.

T. D. Crum, R. B. Stull, and E. W. Eloranta. Coincident lidar and aircraft observations of entrainment into thermals and mixed layers. *Journal of climate and applied meteorology*, 26(7):774–788, 1987.

C. Dai, Z. Gao, Q. Wang, and G. Cheng. Analysis of atmospheric boundary layer height characteristics over the arctic ocean using the aircraft and gps soundings. *Atmospheric and Oceanic Science Letters*, 4(2):124, 2011.

K. Davis, N. Gamage, C. Hagelberg, D. Lenschow, P. Sullivan, and C. Kiemle. An objective method for deriving atmospheric structure from airborne lidar observations. *Journal of Atmospheric and Oceanic Technology*, 17:1455 – 1468, 2000.

M. de Haij, W. Wauben, and H. K. Baltink. Continuous mixing layer height determination using the LD-40 ceilometer: a feasibility study. KNMI Scientific Report WR 2007-01. *Royal Netherlands Meteorological Institute (KNMI), De Bilt, the Netherlands*, 2007.

R. Draxler and G. Hess. An overview of the hysplit4 modeling system of trajectories, dispersion, and deposition. *Australian Meteorological Magazine*, 1998.

S. Emeis, K. Schäfer, and C. Münkel. Surface-based remote sensing of the mixing-layer height - a review. *Meteorologische Zeitschrift*, 17(5), 2008.

F. Fetterer, M. Savoie, S. Helfrich, and P. Clemente-Colón. Multisensor analyzed sea ice extent - northern hemisphere (masie-nh). Technical report, National Snow and Ice Data Center. Boulder, Colorado USA, 2010.

T. J. Garrett, S. Brattström, S. Sharma, D. E. J. Worthy, and P. Novelli. The role of scavenging in the seasonal transport of black carbon and sulfate to the arctic. *Geophysical Research Letters*, 38(16):n/a–n/a, 2011. ISSN 1944-8007.

C. Haas. Airborne observations of the distribution, thickness, and drift of different sea ice types and extreme ice features in the canadian beaufort sea. *Offshore Technology Conference*, 2012.

C. Haas, S. Hendricks, H. Eicken, and A. Herber. Synoptic airborne thickness surveys reveal state of arctic sea ice cover. *Geophysical Research Letters*, 37(9), 2010. ISSN 1944-8007.

J. Hansen and L. Nazarenko. Soot climate forcing via snow and ice albedos. *Proceedings of the National Academy of Sciences of the United States of America*, 101(2):423–428, 2004.

M. Helten, H. G. J. Smit, W. Sträter, D. Kley, P. Nedelec, M. Zöger, and R. Busen. Calibration and performance of automatic compact instrumentation for the measurement of relative humidity from passenger aircraft. *Journal of Geophysical Research: Atmospheres*, 103(D19):25643–25652, 1998. ISSN 2156-2202.

A. B. Herber, C. Haas, R. S. Stone, J. W. Bottenheim, P. Liu, S.-M. Li, R. M. Staebler, J. W. Strapp, and K. Dethloff. Regular airborne surveys of arctic sea ice and atmosphere. *Eos, Transactions American Geophysical Union*, 93(4):41–42, 2012. ISSN 2324-9250.

M. Hess, P. Koepke, and I. Schult. Optical properties of aerosols and clouds: The software package opac. *Bull. Am. Met. Soc.*, 79:831 – 844, 1998.

T. Hock and J. Franklin. The NCAR GPS dropwindsonde. *Bulletin of the American Meteorological Society*, 80(3):407–420, MAR 1999. ISSN 0003-0007.

K. P. Hoinka. Temperature, humidity, and wind at the global tropopause. *Monthly Weather Review*, 1999.

W. A. Hoppel, G. M. Frick, and R. E. Larson. Effect of nonprecipitating clouds on the aerosol size distribution in the marine boundary layer. *Geophysical Research Letters*, 13(2):125–128, 1986. ISSN 1944-8007.

IPCC. Climate Change 2013: The Physical Science Basis. Contribution of Working Group I to the Fifth Assessment Report of the Intergovernmental Panel on Climate Change [Stocker, T.F., D. Qin, G.-K. Plattner, M. Tignor, S.K. Allen, J. Boschung, A. Nauels, Y. Xia, V. Bex and P.M. Midgley(eds.)]. *Cambridge University Press, Cambridge, United Kingdom and New York, NY, USA*, page 1535 pp, 2013.

L. Jakobson, T. Vihma, E. Jakobson, T. Palo, A. Männik, and J. Jaagus. Low-level jet characteristics over the arctic ocean in spring and summer. *Atmospheric Chemistry and Physics*, 13(21):11089–11099, 2013.

V. U. Khattatov, A. E. Tyabotov, A. P. Alekseyev, A. A. Postnov, and E. A. Stulov. Aircraft lidar studies of the arctic haze and their meteorological interpretation. *Atmospheric Research*, 44:99–111, 1997.

J. D. Klett. Stable analytical inversion solution for processing lidar returns. *Applied Optics*, 20(2):211–220, Jan 1981.

A. N. Kolmogorov. The local structure of turbulence in incompressible viscous fluid for very large reynolds numbers. *Proceedings: Mathematical and Physical Sciences*, 1991.

V. A. Kovalev and W. E. Eichinger. *Elastic Lidar.* John Wiley and Sons, 2004.

P. Kupiszewski, C. Leck, M. Tjernström, S. Sjogren, J. Sedlar, M. Graus, M. Müller, B. Brooks, E. Swietlicki, S. Norris, and A. Hansel. Vertical profiling of aerosol particles and trace gases over the central arctic ocean during summer. *Atmospheric Chemistry and Physics*, 13(24):12405–12431, 2013.

A. Lampert, A. Ehrlich, A. Dörnbrack, O. Jourdan, J.-F. Gayet, G. Mioche, V. Shcherbakov, C. Ritter, and M. Wendisch. Microphysical and radiative characterization of a subvisible midlevel arctic ice cloud by airborne observations – a case study. *Atmospheric Chemistry and Physics*, 9(8):2647–2661, 2009.

C. Leck, M. Norman, E. K. Bigg, and R. Hillamo. Chemical composition and sources of the high arctic aerosol relevant for cloud formation. *Journal of Geophysical Research: Atmospheres*, 107(D12):AAC 1–1–AAC 1–17, 2002. ISSN 2156-2202.

U. Leiterer, H. Dier, D. Nagel, T. Naebert, D. Althausen, K. Franke, A. Kats, and F. Wagner. Correction method for RS80-A humicap humidity profiles and their validation by lidar backscattering profiles in tropical cirrus clouds. *Journal of Atmospheric and Oceanic Technology*, 22(1):18–29, JAN 2005. ISSN 0739-0572.

Z. Liu, M. A. Vaughan, D. M. Winker, C. A. Hostetler, L. R. Poole, D. Hlavka, W. Hart, and M. McGill. Use of probability distribution functions for discriminating between cloud and aerosol in lidar backscatter data. *Journal of Geophysical Research: Atmospheres*, 109(D15), 2004. ISSN 2156-2202.

L. Mahrt. Stratified atmospheric boundary layers. *Boundary-Layer Meteorology*, 90(3): 375–396, 1999. ISSN 0006-8314.

S. H. Melfi, J. D. Spinhirne, S.-H. Chou, and S. P. Palm. Lidar observations of vertically organized convection in the planetary boundary layer over the ocean. *J. Climate Appl. Meteor.*, 24:806 – 821, 1985.

G. Mie. Beiträge zur Optik trüber Medien, speziell kolloidalen Metalllösungen. *Annalen der Physik*, 25(3):377–445, 1908.

M. Mielke, N. S. Zinoviev, K. Dethloff, A. Rinke, V. J. Kustov, A. P. Makshtas, V. T. Sokolov, R. Neuber, M. Maturilli, D. Klaus, D. Handorf, and J. Graeser. Atmospheric winter conditions 2007/08 over the arctic ocean based on np-35 data and regional model simulations. *Atmospheric Chemistry and Physics Discussions*, 14(8):11855–11893, 2014.

E. D. Nilsson, Ü. Rannik, E. Swietlicki, C. Leck, P. P. Aalto, J. Zhou, and M. Norman. Turbulent aerosol fluxes over the arctic ocean: 2. wind-driven sources from the sea. *Journal of Geophysical Research: Atmospheres*, 106(D23):32139–32154, 2001. ISSN 2156-2202.

S. R. Pal and A. I. Carswell. Polarization properties of lidar backscattering from clouds. *Applied Optics*, 12(7):1530–1535, Jul 1973.

P. O. G. Persson, C. W. Fairall, E. L. Andreas, P. S. Guest, and D. K. Perovich. Measurements near the Atmospheric Surface Flux Group tower at SHEBA: Near-surface conditions and surface energy budget. *J. Geophys. Res.*, 107(C10):8045, 2002.

M. D. Petters and S. M. Kreidenweis. A single parameter representation of hygroscopic growth and cloud condensation nucleus activity. *Atmospheric Chemistry and Physics*, 7(8):1961–1971, 2007.

L. F. Radke, P. V. Hobbs, and J. L. Stith. Airborne measurements of gases and aerosols from volcanic vents on mt. baker. *Geophysical Research Letters*, 3(2):93–96, 1976. ISSN 1944-8007.

J. Räisänen. Co2-induced climate change in the arctic area in the cmip2 experiments. *SWECLIM Newsletter*, 11:23 – 28, 2001.

A. Roth. *Untersuchungen von Aerosolpartikeln und Wolkenresidualpartikeln mittels Einzelpartikel-Massenspektrometrie und optischen Methoden.* PhD thesis, Johannes Gutenberg-Universität Mainz, 2014.

J.-P. Schäfer. *Implementierung und Anwendung analytischer und numerischer Verfahren zur Lösung der Maxwellgleichungen für die Untersuchung der Lichtausbreitung in biologischem Gewebe.* PhD thesis, Univerität Ulm, 2011.

J. H. Seinfeld and S. N. Pandis. *Atmospheric Chemistry and Physics*. Wiley, 2006.

M. D. Shupe and J. M. Intrieri. Cloud Radiative Forcing of the Arctic Surface: The Influence of Cloud Properties, Surface Albedo, and Solar Zenith Angle. *J. Climate*, 17:616 – 628, 2004.

H. Sodemann and T. Foken. Special characteristics of the temperature structure near the surface. *Theoretical and Applied Climatology*, 80(2-4):81–89, 2005. ISSN 0177-798X.

I. S. Stachlewska and C. Ritter. On retrieval of lidar extinction profiles using two-stream and raman techniques. *Atmospheric Chemistry and Physics*, 10(6):2813–2824, 2010.

I. S. Stachlewska, R. Neuber, A. Lampert, C. Ritter, and G. Wehrle. Amali - the airborne mobile aerosol lidar for arctic research. *Atmospheric Chemistry and Physics*, 10(6): 2947–2963, 2010.

D. Stensrud. Importance of low-level jets to climate: A review. *Journal of Climate*, 1996.

T. M. Stickney, M. W. Shedlov, and D. I. Thompson. Goodrich total temperature sensors; technical report 5755, revision c. *Goodrich Corporation/Rosemount Aerospace Inc., Burnsville, MN*, 1994.

J. Stroeve, M. Serreze, M. Holland, J. Kay, J. Malanik, and A. Barrett. The arctic's rapidly shrinking sea ice cover: a research synthesis. *Climatic Change*, 110(3-4):1005–1027, 2012. ISSN 0165-0009.

R. Stull. *An Introduction to Boundary Layer Meteorology*. Atmospheric Sciences Library. Kluwer Academic Pub, 1988. ISBN 9789027727695.

M. Tjernstroem, M. Zagar, G. Svensson, J. Cassano, S. Pfeifer, A. Rinke, K. Wyser, K. Dethloff, C. Jones, T. Semmler, and M. Shaw. Modelling the arctic boundary layer: An evaluation of six arcmip regional-scale models using data from the sheba project. *Boundary-layer meteorology*, 117:337 – 381, 2005.

O. B. Toon, J. B. Pollack, and B. N. Khare. The optical constants of several atmospheric aerosol species: Ammonium sulfate, aluminum oxide, and sodium chloride. *Journal of Geophysical Research*, 81(33):5733–5748, 1976. ISSN 2156-2202.

P. Tunved, J. Ström, and R. Krejci. Arctic aerosol life cycle: linking aerosol size distributions observed between 2000 and 2010 with air mass transport and precipitation at zeppelin station, ny-ålesund, svalbard. *Atmospheric Chemistry and Physics*, 13(7): 3643–3660, 2013.

S. Twomey. The influence of pollution on the short wave albedo of clouds. *J. Atmos. Sci.*, 34:1149 – 1152, 1977.

D. Vickers and L. Mahrt. Evaluating formulations of stable boundary layer height. *Journal of Applied Meteorology*, 2004.

U. Wacker, K. Potty, C. Luepkes, J. Hartmann, and M. Raschendorfer. A case study on a polar cold air outbreak over fram strait using a mesoscale weather prediction model. *Boundary-Layer Meteorology*, 117(2):301–336, 2005. ISSN 0006-8314.

J. Wang. Evaluation of the dropsonde humidity sensor using data from DYCOMS-II and IHOP_2002. *Journal of Atmospheric and Oceanic Technology*, 22(3):247–257, MAR 2005. ISSN 0739-0572.

P. J. Wetzel. Toward parameterization of the stable boundary layer. *Journal of Applied Meteorology*, 21:7–13, jan 1982.

M. Winton. Sea ice-albedo feedback and nonlinear arctic climate change, in arctic sea ice decline: Observations, projections, mechanisms, and implications (eds e. t. deweaver, c. m. bitz and l.-b. tremblay). *American Geophysical Union, Washington, D.C.*, pages 111–131, 2008.

C. Xie, N. Sugimoto, I. Matsui, A. Shimizu, B. Tatarov, and T. Nishizawa. Measurement of aerosols and clouds with combined raman elastic-backscatter lidar. *National Institute for Environmental Studies*, 2008.

P. Zieger, R. Fierz-Schmidhauser, M. Gysel, J. Ström, S. Henne, K. E. Yttri, U. Baltensperger, and E. Weingartner. Effects of relative humidity on aerosol light scattering in the arctic. *Atmospheric Chemistry and Physics*, 10(8):3875–3890, 2010.

S. Zilitinkevich and A. Baklanov. Calculation of the height of the stable boundary layer in practical applications. *Boundary-Layer Meteorology*, 105(3):389–409, 2002. ISSN 0006-8314.

S. S. Zilitinkevich. Third-order transport due to internal waves and non-local turbulence in the stably stratified surface layer. *Quarterly Journal of the Royal Meteorological Society*, 128(581):913–925, 2002. ISSN 1477-870X.

Acknowledgements

First I would like to thank Klaus Dethloff for the unique opportunity to work and write my thesis in his research group under excellent conditions. I want to thank in particular my supervisor Roland Neuber for his great commitment in guiding my work and for his patience and continuous support.

I would like to thank all collegues of my working group at AWI for the warm and friendly atmosphere. Christoph Ritter who always found time for a discussion and shared his knowledge on lidar. Marion Maturilli for helpful discussions on dropsonde measurements and meteorological topics. And Alexander Schulz for constructive debates about atmospheric boundary layers and various Matlab issues.

The organizers and participants of the PAMARCMIP and VERDI campaigns 2012, in particular Andreas Herber, Manfred Wendisch, Eike Bierwirth, Christian Haas, Richard Leaitch, André Ehrlich, Jessica Meyer, and Marcus Klingebiel for the opportunities and good cooperation in a nice and friendly working environment. And the engineers of the AWI flight crew, in particular Martin Gehrmann, Franzi Nehring, Jo Kaessbohrer, Julia Binder and Christian Konrad, who manage the immense workload of the technical realization of the aircraft campaigns.

And of course I would like to thank my family for always supporting me and especially Steffi for motivating me, supporting me in realizing my thesis and for just being there.

Erklärung

Hiermit versichere ich, dass ich die vorliegende Arbeit selbstständig verfasst und keine anderen als die angegebenen Quellen und Hilfsmittel verwendet habe. Die Arbeit wurde an keiner anderen Hochschule eingereicht.

Lukas Schmidt